

doi:10.14379/iodp.proc.356.102.2017

Expedition 356 methods¹



S.J. Gallagher, C.S. Fulthorpe, K. Bogus, G. Auer, S. Baranwal, I.S. Castañeda, B.A. Christensen, D. De Vleeschouwer, D.R. Franco, J. Groeneveld, M. Gurnis, C. Haller, Y. He, J. Henderiks, T. Himmler, T. Ishiwa, H. Iwatani, R.S. Jatiningrum, M.A. Kominz, C.A. Korpanty, E.Y. Lee, E. Levin, B.L. Mamo, H.V. McGregor, C.M. McHugh, B.F. Petrick, D.C. Potts, A. Rastegar Lari, W. Renema, L. Reuning, H. Takayanagi, and W. Zhang²

Keywords: International Ocean Discovery Program, IODP, Expedition 356, *JOIDES Resolution*, Site U1458, Site U1459, Site U1460, Site U1461, Site U1462, Site U1463, Site U1464, northwest shelf of Australia, Indonesian Throughflow, paleomagnetism, benthic foraminifers, planktonic foraminifers, nannofossils, downhole logs, physical properties, stratigraphic correlation

Contents

- 1 Introduction
- 4 Lithostratigraphy and sedimentology
- 12 Biostratigraphy and micropaleontology
- 19 Geochemistry
- 21 Paleomagnetism
- 23 Physical properties
- 28 Downhole measurements
- 31 Stratigraphic correlation
- 34 References

Introduction

This chapter documents the procedures and methods used in the shipboard laboratories during International Ocean Discovery Program (IODP) Expedition 356. This introductory section provides a rationale for the site locations and an overview of IODP depth conventions, curatorial procedures, and general core handling/analyses during Expedition 356. Subsequent sections describe specific laboratory procedures and instruments in more detail. This information only applies to shipboard work described in this *Proceedings* volume; methods used in shore-based analyses of Expedition 356 samples and/or data will be described in various scientific contributions in the open peer-reviewed literature and the Expedition research results section of this volume.

Site locations

The seven Expedition 356 sites (U1458–U1464) are situated along the northwest shelf (NWS) of Australia and comprise a 10° latitudinal transect that targeted tropical reef and carbonate diachroneity related to Leeuwin Current intensity and Indonesian Throughflow/Indo-Pacific Warm Pool influence, the history of the Australian monsoon, and a detailed temporal record of northern Australian plate dynamic subsidence. Previous work by both academia and industry on the NWS provided site data, including well completion reports, seismic data, wireline logs, cuttings, sidewall cores, and limited engineering cores that were used to guide the initial operations plan for each site.

GPS coordinates from precruise site surveys and adjacent industry wells were used to position the vessel at all Expedition 356 sites. A SyQuest Bathymetry 2010 CHIRP subbottom profiler was used to monitor seafloor depth on the approach to each site to confirm the

depth profiles from precruise surveys. Once the vessel was positioned at the site coordinates, the thrusters were lowered and a positioning beacon was dropped to the seafloor. Dynamic positioning control of the vessel used navigational input from the GPS and triangulation to the seafloor beacon, weighted by the estimated positional accuracy. The final hole position was the mean position calculated from the GPS data collected over a significant portion of the time the hole was occupied.

Coring and drilling operations

All four standard coring systems, the advanced piston corer (APC), half-length APC (HLAPC), extended core barrel (XCB), and rotary core barrel (RCB), were used during Expedition 356 (see the Operations sections in each site chapter). The APC system was used in the upper portion of a hole to obtain high-quality core. The APC cuts soft-sediment cores with minimal visual coring disturbance relative to other IODP coring systems. After the APC core barrel is lowered through the drill pipe and lands near the bit, the drill pipe is pressured up until the two shear pins that hold the inner barrel attached to the outer barrel fail. The inner barrel then advances into the formation and cuts the core. The driller can detect a successful cut, or “full stroke,” from the pressure gauge on the rig floor.

APC refusal is conventionally defined in two ways: (1) the piston fails to achieve a complete stroke (as determined from the pump pressure reading) because the formation is too hard, or (2) excessive force (>60,000 lb; ~267 kN) is required to pull the core barrel out of the formation. When a full stroke could not be achieved, additional attempts were typically made, and after each attempt the bit was advanced by the core recovery (m). The number of additional attempts was generally dictated by the recovery length of the partial stroke core and the time available to advance the hole by piston coring.

¹ Gallagher, S.J., Fulthorpe, C.S., Bogus, K., Auer, G., Baranwal, S., Castañeda, I.S., Christensen, B.A., De Vleeschouwer, D., Franco, D.R., Groeneveld, J., Gurnis, M., Haller, C., He, Y., Henderiks, J., Himmler, T., Ishiwa, T., Iwatani, H., Jatiningrum, R.S., Kominz, M.A., Korpanty, C.A., Lee, E.Y., Levin, E., Mamo, B.L., McGregor, H.V., McHugh, C.M., Petrick, B.F., Potts, D.C., Rastegar Lari, A., Renema, W., Reuning, L., Takayanagi, H., and Zhang, W., 2017. Expedition 356 methods. In Gallagher, S.J., Fulthorpe, C.S., Bogus, K., and the Expedition 356 Scientists, *Indonesian Throughflow*. Proceedings of the International Ocean Discovery Program, 356: College Station, TX (International Ocean Discovery Program).
<http://dx.doi.org/10.14379/iodp.proc.356.102.2017>

² Expedition 356 Scientists' addresses.
MS 356-102: Published 26 February 2017

Note that this advance-by-recovery method results in a recovery of ~100% based on the assumption that the barrel penetrated the formation by the equivalent of the length of core recovered. When a full or partial stroke was achieved but excessive force could not retrieve the barrel, the core barrel was sometimes “drilled over,” meaning after the inner core barrel was successfully shot into the formation, the drill bit was advanced to total depth to free the APC barrel.

Nonmagnetic core barrels were used during all APC coring to a pull force of ~40,000 lb. In general, only the second APC hole from any Expedition 356 site was oriented using the Icefield MI-5 orientation tool (see [Paleomagnetism](#)) because of the variable nature of the upper sediments. Formation temperature measurements were taken in many of the second APC holes to obtain temperature gradients and heat flow estimates (see [Downhole measurements](#)).

Once APC refusal was reached, or in many cases when the APC system was unable to be used because the formation was too indurated at the surface (e.g., Site U1460), the HLAPC system was used. The standard APC system contains a 9.5 m long core barrel, and the HLAPC system uses a 4.7 m long core barrel. In most instances, the HLAPC system was deployed after the APC system reached refusal to extend the total piston coring depth (e.g., Site U1461). The HLAPC system was also employed at a site when the upper sediments or sedimentary layers were too hard to allow a full APC stroke and too soft for XCB recovery (e.g., Site U1459). During use of the HLAPC system, the same criteria were applied in terms of refusal as for the full-length APC system. Use of the HLAPC system allowed significantly greater piston coring sampling depths to be attained than would have otherwise been possible and recovery of more indurated material in the upper sections than possible with the APC or XCB systems.

The XCB was used to advance the hole when APC or HLAPC refusal occurred before the target depth was reached (Site U1461), when the formation became too stiff for HLAPC coring (Site U1463), or when hard substrate was encountered in the upper sections of a hole (Sites U1458, U1459, and U1462). The XCB is a rotary system with a small cutting shoe (bit) that extends below the large APC/XCB bit. The smaller bit can cut a semi-indurated core with less torque and fluid circulation than the main bit, optimizing recovery. The XCB cutting shoe extends ~30.5 cm ahead of the main bit in soft sediment but retracts into the main bit when hard formations are encountered. This system resulted in the greatest loss of core quality (the majority of XCB cores collected during Expedition 356 were biscuited). Because the APC and XCB systems use the same bit, it is possible to switch back and forth between the two coring systems. As a result, it was occasionally possible to resume HLAPC coring after an interval of XCB coring if the formation became softer beneath a layer of hard material. This was successfully used numerous times during Expedition 356 (e.g., Site U1459) when alternating hard and soft layers were encountered in the upper ~200 m of sediment.

The bottom-hole assembly (BHA) is the lowermost part of the drill string. A typical APC/XCB BHA consists of a drill bit (outer diameter = 11¹/₁₆ inches), a bit sub, a seal bore drill collar, a landing saver sub, a modified top sub, a modified head sub, a nonmagnetic drill collar (for APC/XCB), a number of 8 inch (~20.32 cm) drill collars, a tapered drill collar, six joints (two stands) of 5¹/₂ inch (~13.97 cm) drill pipe, and one crossover sub. A lockable float valve was used when downhole logging was planned so that downhole logs could be collected through the bit (e.g., Site U1463).

The RCB is generally deployed when XCB coring reaches refusal (generally when the time to cut a core is >90 min), but it was also used during Expedition 356 as an alternative to the XCB and to duplicate XCB-cored intervals in order to recover cores with reduced disturbance (biscuiting). The RCB is the most conventional rotary drilling system. The RCB requires a dedicated RCB BHA and a dedicated RCB drilling bit. The BHA used for RCB coring included a 9¹/₂ inch RCB drill bit, a mechanical bit release (if logging was considered), a modified head sub, an outer core barrel, a modified top sub, a modified head sub, and 7–10 control length drill collars followed by a tapered drill collar to the two stands of 5¹/₂ inch drill pipe. Most cored intervals were ~9.7 m long, which is the length of a standard rotary core and approximately the length of a joint of drill pipe. In some cases, the drill string was drilled or “washed” ahead without recovering sediment to advance the drill bit to a target depth to resume core recovery. Such intervals were typically drilled using a center bit installed within the RCB bit. When coring at many sites, half-cores were sometimes collected with both the XCB (e.g., Site U1461) and RCB (e.g., Site U1459) to improve recovery and when rates of penetration decreased significantly.

Coring disturbance

Core material has the potential to be disturbed and/or contain extraneous material as a result of the drilling process, core handling, and analysis. In formations with loose granular layers (e.g., sand, shell hash, coral rubble, etc.), material from intervals higher in the hole may be washed down by drilling circulation, accumulate at the bottom of the hole, and then be sampled with the next core. This is referred to as “fall-in.” In most Expedition 356 cores from the southern sites (U1458, U1459, and U1460), there was evidence of fall-in; when present it affected the upper ~10–50 cm of the cores. Fall-in was less common in the northern sites (U1461, U1462, U1463, and U1464). Common coring deformation includes the concave appearance of originally horizontal bedding. Another disturbance type is “flow-in,” where the piston coring action results in fluidization at the bottom of the cores. Retrieval from depth to the surface may result in elastic rebound. Gas that is in solution at depth may become free and drive core segments within the liner apart. Both elastic rebound and gas pressure can result in a total length for each core that is longer than the interval that was cored and thus a calculated recovery >100%. If gas expansion or other coring disturbance results in a void in any particular core section, the void can be closed by moving material if very large, stabilized by a foam insert if moderately large, or left as is in the core liner. When gas content is high, pressure must be relieved for safety reasons before the cores are cut into segments. This is accomplished by drilling holes into the liner, which forces some sediment as well as gas out of the liner. In more consolidated material, common core disturbances include biscuiting, where fractured material (“biscuits”) spins within the core barrel. In many cases, drilling slurry can be interjected between biscuits. Finally, fracturing, fragmentation, and brecciation as a result of the drilling process are also common drilling-induced disturbances.

Occurrences of these disturbance types are noted and described in the Lithostratigraphy sections in each site chapter and are graphically represented on the visual core descriptions (VCDs).

Site, hole, core, and sample numbering

Numbering of the sites, holes, cores, and samples followed standard IODP protocol. Drilling sites have been numbered consecu-

tively from the first site drilled by the *Glomar Challenger* in 1968, and since Expedition 301 the prefix “U” has been used to designate sites cored by the R/V *JOIDES Resolution*. At each site, multiple holes are often drilled, and a letter suffix distinguishes the holes drilled at a single site. For example, the first hole would be given the suffix “A,” the second “B,” and so on.

Following the hole designation, each recovered core was numbered sequentially. A cored interval is generally ~9.5 m, the length of a standard core barrel, with the exception of the 4.7 m core barrel of the HLAPC system. The specific coring system used to recover a core is designated by a letter representing the core type and is a suffix to the core number: H = APC, F = HLAPC, X = XCB, and R = RCB.

Each recovered core was cut into ~1.5 m sections. The number of sections is determined by the core recovery, and sections were numbered sequentially starting with “1” at the top of the core. Each core is eventually split lengthwise into working and archive halves (described in [Core handling and analysis](#)) designated by either the letter “W” or “A” succeeding the core number. For depth calculation purposes (see [Sample depth calculation](#)), the top depth of the core is equated with the top depth of the cored interval (in drilling depth below seafloor [DSF]) to achieve consistency in handling analytical data derived from the cores. Sample intervals are described in centimeters within a core section (typically between 0 and 150 cm) beginning from the top of the core section.

Thus, the full curatorial identifier of a sample consists of the following: expedition, site, hole, core number, core type, section number, section half, and interval in centimeters measured from the top of the core section. For example, a sample identified as “356-U1461D-11R-3W, 50–55 cm” represents a 5 cm interval from the third section (working half) of Core 11R (cored with the RCB system) from Hole D of Site U1461 during Expedition 356 (Figure F1).

Sample depth calculation

During Expedition 356, the cored interval was measured in meters as determined by core depth below seafloor, Method A (CSF-A). The calculation of this depth scale is defined by protocol (see IODP Depth Scales Terminology at <http://www.iodp.org/policies-and-guidelines>). In general, the depth below seafloor is determined by subtracting the initial drill pipe measurement to the seafloor

from the total drill pipe measurement (DSF) (Figure F1). For each core, the core depth interval begins with the depth below seafloor where coring began and extends to the depth that coring advanced. However, if a core has incomplete recovery (<100%), all material is assumed to originate from the top of the cored interval as a continuous section for curation purposes; thus, the true depth interval within the cored interval is unknown and represents a sampling uncertainty in age-depth analysis or correlation with downhole logging data. In addition, cores from the holes at each of two sites (U1461 and U1463) were correlated to produce a splice based on a composite depth scale (core composite depth below seafloor [CCSF-A]). The calculation of this depth scale is discussed in [Stratigraphic correlation](#).

Additionally, wireline log depths were calculated from the wireline log depth below seafloor (WSF). When multiple logging passes were made (see [Downhole measurements](#)), the wireline log depths were matched to one reference pass, creating the wireline log matched depth below seafloor (WMSF). These distinctions in nomenclature between core (curated) and wireline log depth should be noted because the same depth value from different scales does not necessarily refer to the same stratigraphic interval.

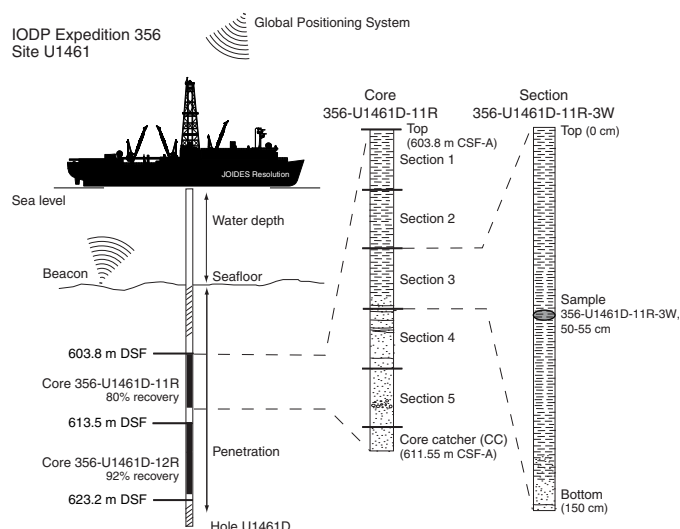
Core handling and analysis

Immediately upon arriving on deck, core catcher samples were taken for biostratigraphic analyses. The cores were then cut into 1.5 m sections, after which whole-round samples were taken for shipboard interstitial water (IW) and noted by the use of a yellow end cap on the core liner. Additional samples taken on the catwalk include syringe samples for routine hydrocarbon gas safety monitoring (see [Geochemistry](#)). Once the core sections were brought inside, they were immediately run through the Special Task Multisensor Logger (STMSL) by the stratigraphic correlators to aid in drilling guidance (see [Stratigraphic correlation](#)). After the cores equilibrated to laboratory temperature (~4 h), they were run through the Whole-Round Multisensor Logger (WRMSL) for *P*-wave velocity, magnetic susceptibility (MS), and bulk density measurements and also through the Natural Gamma Radiation Logger (NGRL). Thermal conductivity measurements were also taken (see [Physical properties](#)).

The core sections were then split lengthwise into archive and working halves. Oriented pieces of more indurated sediments were marked on the bottom with a red wax pencil. The working-half sections were used for taking discrete shipboard samples for paleomagnetic, physical properties, geochemical, and thin section analyses (for details see the individual laboratory group methods in this chapter), and, in some cases (i.e., Sites U1458, U1459, and U1460), science party personal samples for postcruise research. Sampling for postcruise research was based on the sampling plan agreed upon by the science party and the Sample Allocation Committee. Samples for personal postcruise research from all other sites (U1461, U1462, U1463, and U1464) were taken during a sampling party at the Gulf Coast Repository (College Station, Texas, USA) from 19 to 26 February 2016.

The archive half-core sections were run through the Section Half Imaging Logger (SHIL) and the Section Half Multisensor Logger (SHMSL) for color reflectance and point magnetic susceptibility (MSP) measurements. The archive halves were described by expedition scientists visually and by smear slide analyses. Finally, most of the sections were measured with the cryogenic magnetometer (see [Paleomagnetism](#)).

Figure F1. IODP conventions for naming sites, holes, cores, and samples.



All instrument data from Expedition 356 were uploaded into the IODP Laboratory Information Management System (LIMS), and core descriptions were entered into the database using the DESClogik application. DESClogik is a program used to input visual (macro- and/or microscopic) core descriptions.

When all shipboard measurements were completed, data uploaded, and samples taken, the cores were wrapped in clear plastic film, sealed in plastic “D-tubes,” and transferred to cold storage on the ship. At the end of the expedition, the cores were transported to the Gulf Coast Repository until the sampling party, after which they were transported for storage at the IODP Kochi Core Center in Kochi, Japan.

Authorship of methods and site chapters

The separate discipline-specific sections of the methods and site chapters were written by the following scientists (in alphabetical order):

Background and objectives: Fulthorpe, Gallagher
 Operations: Bogus
 Lithostratigraphy: Auer, Himmler, Iwatani, Korpany, Lee, McGregor, McHugh, Petrick, Potts, Rastegar Lari, Reuning
 Biostratigraphy and micropaleontology: Baranwal, Groeneveld, Haller, Henderiks, Jatiningrum, Mamo
 Geochemistry: Castañeda, He, Takayanagi, Zhang
 Paleomagnetism: Franco, Levin
 Physical properties: De Vleeschouwer, Gurnis, Ishiwa, Kominz
 Downhole measurements: De Vleeschouwer, Gurnis
 Stratigraphic correlation: Christensen, Renema

Lithostratigraphy and sedimentology

The lithology of sediments recovered during Expedition 356 was determined primarily from the archive half of each core using visual (macroscopic) core descriptions, smear slides, and thin sections along with additional information from digital core imaging, color reflectance spectrophotometry, X-ray diffraction (XRD), X-ray fluorescence (XRF), and MS analyses. The procedures and criteria for the visual core descriptions were based on those used during Ocean Drilling Program (ODP) Leg 194 (Shipboard Scientific Party, 2002).

We used the DESClogik application to record and upload descriptive data into the LIMS database (see the DESClogik user guide at <http://iodp.tamu.edu/labs/documentation>). DESClogik contains spreadsheet templates with drop-down menus that were customized for the material likely to be recovered during Expedition 356 and were modified as needs arose. The completed spreadsheets record both the visual core descriptions and estimates of the texture and relative abundances of biogenic and nonbiogenic components derived from microscopic examination of smear slides and petrographic slides (thin sections). The core depths at which smear slides and thin sections were taken were recorded in the Sample Master application (where the depths are synced with the DESClogik slide data and descriptions). Descriptive data in the LIMS database were used as output to produce VCD sheets, which are standardized graphic reports (see [Core descriptions](#)).

The standard method of splitting cores into working and archive halves (using either a thin wire or a circular saw) can alter the appearance of the split surface and obscure fine details of lithology and sedimentary structure. When necessary, the cut surface of the archive half was prepared for unobscured sedimentological exam-

ination and digital imaging by gently scraping a freshly cleaned stainless steel or glass plate across the core section and parallel to bedding planes to prevent cross-stratigraphic contamination. Cleaned sections were then described in conjunction with measurements made using the SHIL and SHMSL.

Sediment and rock description and classification

Analyses of rocks and sediments start with recognition, identification, and physical description of individual sedimentary grains, and the resulting suite of grain types and textures is used to classify the sediments and rocks. Description and classification of sediments and rocks for Expedition 356 followed the decision tree and classification schema outlined in Figure F2, with detailed definitions and rationale outlined below.

Lithification

Mixtures of sediments and rocks were recovered during Expedition 356, and the degree of lithification was the first feature noted for each lithology. Lithification categories were adapted from the definitions from Gealy et al. (1971):

- Lithified = rock cannot be scratched or broken without the help of a saw (based on “extreme” and “strong” in Gealy et al. [1971]).
- Partially lithified = hard but friable sediments can be broken easily or scratched with a spatula or fingernail (based on “moderate” and “poor” in Gealy et al. [1971]).
- Unlithified = soft sediments have little strength and are deformed under the pressure of a fingernail or the broad blade of a spatula.

Principal lithology

Sediment and rock units were given principal lithologies based on their composition and texture. Principal lithologies were divided into two main categories: (1) >50% carbonate and (2) >50% siliciclastics. Mixtures between these principal categories and other components were described using major and minor modifiers.

Principal carbonate names

Carbonates were named using the original Dunham (1962) textural classification in conjunction with the depositional textures of Embry and Klovan (1971) for allochthonous limestone (rock) or sediments. Autochthonous carbonates were grouped as boundstones, following the original Dunham (1962) classification. We defined seven principal names (Figure F3):

- Mudstone = mud-supported fabric with <10% grains.
- Wackestone = mud-supported fabric with >10% grains.
- Packstone = grain-supported fabric with intergranular mud.
- Grainstone = grain-supported fabric with no mud.
- Floatstone = matrix-supported fabric (with at least 10% of grains >2 mm).
- Rudstone = grain-supported fabric (with at least 10% of grains >2 mm).
- Boundstone = components organically bound during deposition.

The “grain” component in these definitions is >20 μm mean diameter (i.e., visible by eye or with a hand lens) (Dunham, 1962), the “mud” component is <20 μm (Dunham, 1962), and carbonate mud was termed micrite.

To guide macroscopic descriptions, the presence or absence of micrite was checked on a regular basis by examining the sample un-

Figure F2. Expedition 356 classification schema and decision tree used for entering macroscopic core descriptions into DESClogik and for naming lithologies. Descriptions were classified by primary features (blue shading; in DESClogik menu order) then secondary features (white). Within Principal lithology categories of >50% carbonate or >50% siliciclastic, each lithology name used the format major modifier (optional) + principal name (required) + minor modifier (optional). Major and minor modifiers were linked to the principal name with the prefix "rich" and the suffix "with," respectively (e.g., coral-rich grainstone with foraminifers). Carbonate (pink) and siliciclastic (orange) nodes give hierarchy and rules for determining principal name and major and minor modifiers. Principal name is based on texture (Figure F3) or dolomite percent. Major and minor modifiers reflect estimated percentages of major components or presence of minor components of interest. Fossil components (red dashed lines) were listed in the Fossils category under Other features and were available for use as major and/or minor modifiers. See text for the Lithification, Other features, and Drilling disturbance description options.

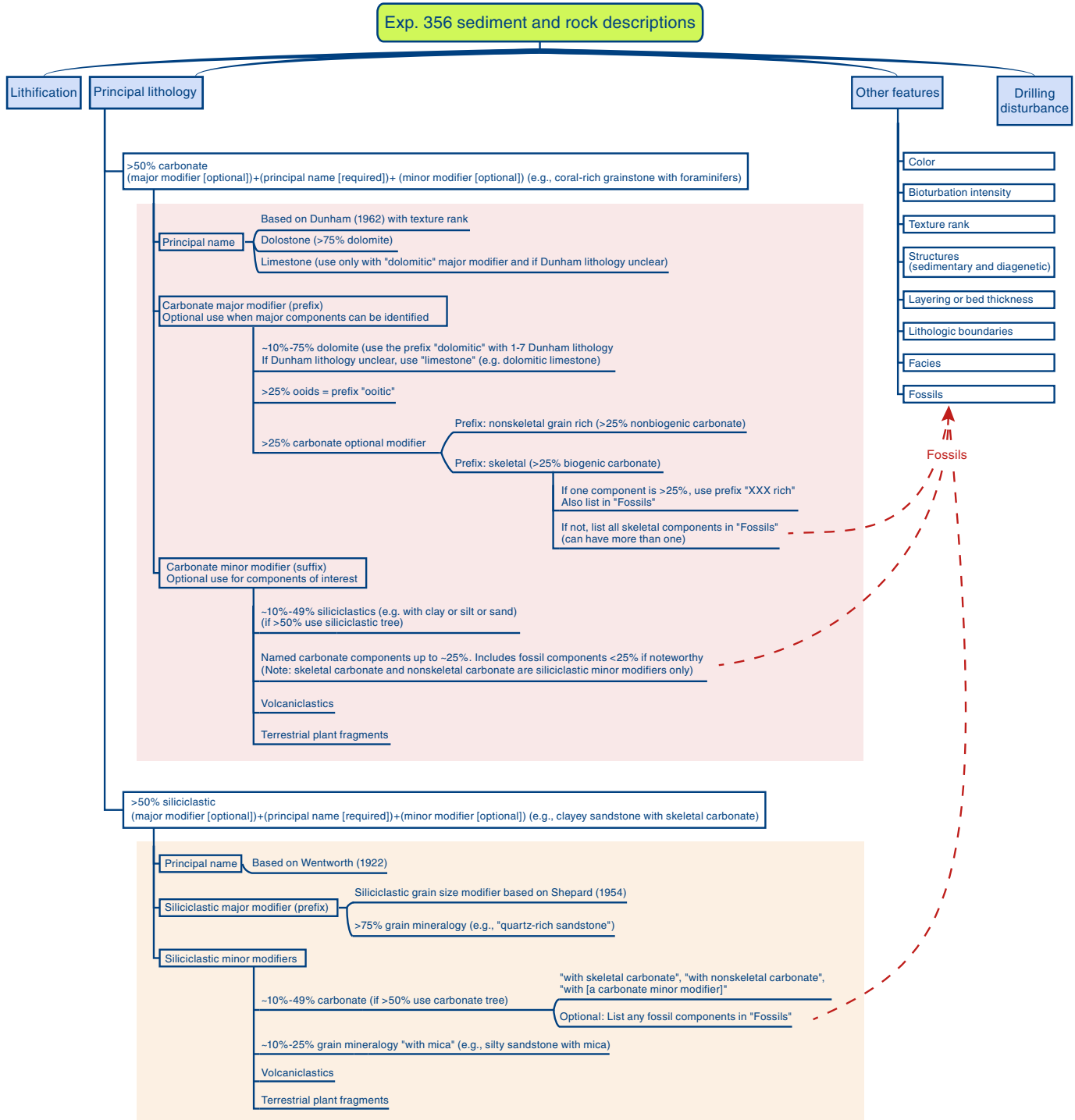
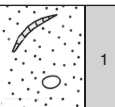
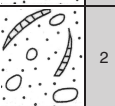
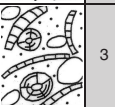
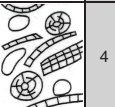


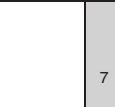


Figure F3. Classification of limestone based on depositional texture, Expedition 356. Numbers are the texture “rank” used to plot texture variations downcore. Figure after Dunham (1962), with modifications by Embry and Klovan (1971) and Stow (2005).

Original components not bound together during deposition	Mud supported	Less than 10% grains	Mudstone		1
		More than 10% grains	Wackstone		2
	Grain supported	Packstone		3	
	Lacks mud and is grain supported	Grainstone		4	
Original components not organically bound during deposition	>10% grains >2 mm	Matrix supported	Floatstone		5
		Supported by >2 mm component	Rudstone		6
Original components organically bound during deposition	Boundstone				7

der a hand lens or binocular microscope or with smear slide or thin section analysis.

Floatstone and rudstone matrixes may range from mudstone to grainstone. For example, a sediment with 10 mm diameter rhodoliths with grains in contact with one another and having a skeletal grainstone matrix is classed as a rudstone.

Strictly speaking, the Dunham (1962) classification applies only to the sorting characteristics in lithified material; however, we also applied the Dunham (1962) classifications to unlithified carbonate sediments because the textures of the carbonate rocks and the sediments recovered during Expedition 356 are very similar. The distinction between rock and sediment was noted under the Lithification descriptor.

Any lithology that appeared to contain more than ~75% dolomite was called “dolostone.” See **Carbonate modifiers** below for further definitions of dolomite classifications.

Carbonate modifiers

The principal name (e.g., packstone) was often given a prefix called a “major modifier” (e.g., skeletal) to describe the lithology of the granular sediments and rocks in greater detail. In some instances the principal name was followed by a suffix or “minor modifier.” All minor modifiers are preceded by the term “with” (e.g., packstone with clay). Major modifiers were primarily used to describe dominant siliciclastic grain sizes (e.g., silty clay), macroscopic biogenic components, constituent mineralogy, and rock composition. Minor modifiers were mainly used to add greater detail about

features noted in the core summaries. For simplicity, minor modifiers were used sparingly.

Carbonate major modifiers (prefix). If the dominant biogenic component was >25% and could be identified and classified taxonomically, the major modifier specified the dominant fossil type followed by the term “rich” (e.g., coral-rich rudstone). The dominant fossil type was also specified in the Fossil column in the DESClogik workbooks.

Most identifiable nonskeletal grains were either peloids or ooids. Ooids from this region commonly comprise superficial coatings on a peloid core, which makes macroscopic differentiation between the two clast types difficult. Therefore, the term “nonskeletal grain rich” was used to indicate the occurrence of >25% nonbioclastic allochems. If nonskeletal grains were present but did not exceed 25%, the term “with nonskeletal grains” was applied (i.e., principal name was assigned a minor modifier). In the case where ooids were clearly identifiable in either the visual core description or thin sections, the major modifier “ooid rich” or the minor modifier “with ooids” was used as appropriate.

“Dolomitic” was used as a major modifier for sediments containing ~10%–75% dolomite or dolomitic texture (e.g., dolomitic packstone). When a unit was dolomitized but it was not possible to identify the principal carbonate lithology of Dunham (1962), the generic term “limestone” was used as the principal name (e.g., dolomitic limestone).

Where the siliciclastic component was ~10%–49%, various minor modifiers were used (described below). A major siliciclastic modifier was never used, because if the siliciclastic component was >49%, then a siliciclastic “principal name” was assigned instead.

If the components could not be identified because of their small grain size or if they were recrystallized, no major modifiers were used.

The major modifiers described here could also be applied to dolostone.

Carbonate minor modifiers (suffix). Minor carbonate modifiers were applied after the principal name where ~10%–50% of grains were siliciclastics (“with clay,” “with silt,” or “with sand,” depending on grain size [e.g., skeletal wackstone with sand]) or other noncarbonatic components (e.g., with anhydrite). Fossil components could also be used as a minor modifier if <25% but particularly noteworthy.

Principal siliciclastic lithologies

Some intervals contained siliciclastic grains of quartz, feldspar, and other minerals eroded from igneous, metamorphic, and non-carbonate sedimentary rocks. When siliciclastic material constituted >50% of the composition, the sediment or rock was deemed siliciclastic.

We used three principal names for siliciclastic sediments and rocks, based on the Udden-Wentworth grain size scale (Wentworth, 1922) (Figure F4):

- Claystone = >50% clay.
- Siltstone = >50% silt.
- Sandstone = >50% sand.

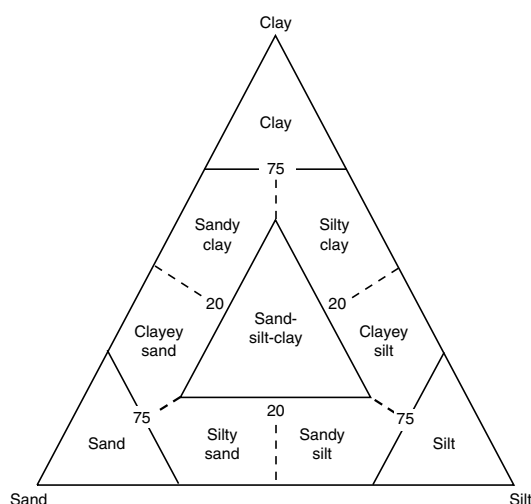
Siliciclastic major modifiers (prefixes)

Names for mixed siliciclastic grain sizes follow Shepard (1954) (e.g., silty claystone) (Figure F5). If siliciclastic material exceeded >75%, grain size modifiers were not used. Instead, the dominant mineral was identified and added as a major modifier (e.g., quartz-rich sandstone).

Figure F4. Udden-Wentworth grain size classification of terrigenous sediments (after Wentworth, 1922), Expedition 356.

Millimeters (mm)	Micrometers (μm)	Phi (ϕ)	Wentworth size class	Rock type
4096		-12.0	Boulder	Conglomerate/ Breccia
256		-8.0	Cobble	
64		-6.0	Pebble	
4		-2.0	Granule	
2.00		-1.0	Very coarse sand	
1.00		0.0	Coarse sand	Sandstone
1/2	500	1.0	Medium sand	
1/4	250	2.0	Fine sand	
1/8	125	3.0	Very fine sand	
1/16	63	4.0	Coarse silt	
1/32	31	5.0	Medium silt	Siltstone
1/64	15.6	6.0	Fine silt	
1/128	7.8	7.0	Very fine silt	
1/256	3.9	8.0	Clay	Claystone
0.0006	0.06	14.0		

Figure F5. Diagram showing the classification scheme used for siliciclastic sediments and rocks (after Shepard, 1954), Expedition 356.



Siliciclastic minor modifiers (suffix)

Minor siliciclastic modifiers were applied after the principal name where carbonate was ~10%–50% of the material (e.g., sandstone with coral). Taxonomic minor modifiers were used where the carbonate component could be identified; otherwise, the generic terms “with skeletal carbonate,” “with nonskeletal carbonate,” or “with carbonate” were used.

Minor modifiers based on grain mineralogy were applied for components up to 25% (e.g., sandstone with mica).

Other features

Additional features were used to distinguish between lithologic units or to describe specific features (see below and Figure F6 for examples) of the core.

Texture rank

Principal carbonate lithology was assigned a rank and then plotted on the visual core description to aid visualization of sediment and rock texture changes. Carbonates were ranked using the number order given in **Principal carbonate names**. No texture rank was assigned to siliciclastic principal lithologies.

Color

A general description of color in conjunction with other features was used as an indicator of changes within and between lithologic units.

Bioturbation

Five degrees of bioturbation were differentiated, based on Droser and Bottjer (1986):

- 1 = bioturbation absent (0%).
- 2 = slight bioturbation (<10%–30%).
- 3 = moderate bioturbation (30%–60%).
- 4 = common bioturbation (60%–90%).
- 5 = complete bioturbation (>90%).

Fossils

Micro- and macrofossils that either constituted a major component of the total sediment or rock or were noteworthy for other reasons (e.g., as facies indicators and/or index fossils) were recorded.

Structures and diagenesis

The location and nature of primary sedimentary structures (e.g., planar laminations) and deformational structures (e.g., partly cemented fractures) were noted.

Diagenetic features, especially marine noncarbonate authigenic minerals such as pyrite, glauconite, phosphate, celestite, and anhydrite, were noted. Glauconite is a black to greenish, iron-rich sheet silicate, which can infill chambers in microfossil tests and pores or occur as rounded sand-sized grains. Descriptors for dolomitization are discussed in **Carbonate modifiers** above.

Layer or bed thickness

Seven terms for layer and bed thickness were used following the terminology of McKee and Weir (1953) for sedimentary beds and laminae:

- Very thickly bedded = >100 cm.
- Thick bedded = >30–100 cm.
- Medium bedded = >10–30 cm.
- Thin bedded = >3–10 cm.
- Very thinly bedded = >1–3 cm.
- Thickly laminated = 1–0.3 cm.
- Thinly laminated = <0.3 cm.

Lithologic boundaries

Lithologic boundaries were described by the nature of the contact surface (“bioturbated,” “erosive,” “gradational,” “hardground,” “scoured,” “sharp,” or “wavy”) and by the angle of the contact (“horizontal,” “subhorizontal,” “subvertical,” “vertical,” and “irregular”).

Facies

Four categories of sediments and rocks were based on mineralogy and origin.

Pelagic facies. Pelagic sediments and rocks consist of fine-grained skeletons and skeletal debris produced primarily within the upper part of the water column in open-marine environments by calcareous microfauna (e.g., foraminifers and pteropods) and microflora (e.g., coccolithophores) and siliceous microfauna (e.g., radiolarians) and microflora (e.g., diatoms).

Hemipelagic facies. Hemipelagic sediments contain the same major components as pelagic sediments with the addition of >10% neritic carbonate and/or siliciclastic material representing transi-

Figure F6. Symbols used in visual core and smear slide descriptions, Expedition 356.

Structure	Fossil	Diagenetic structure
Chickenwire structure	Barnacle	Anhydrite nodule
Cross-bedded	Bivalve	Chert nodule
Fault	Brachiopod	Concretion
Flaser bedding	Bryozoa	Dissolution cavities
Grading (normal)	Coral (branching)	Dissolution seam
Grading (reverse)	Coral (massive)	Filled cavities
Intraclasts	Coral (solitary)	Fully cemented fracture
Lenticular bedding	Coralline algae	Glauconite nodules
Load cast	Echinoderm	Gypsum nodule
Low-angle cross-stratification	Foraminifer	Manganese crust
Microbialite	Foraminifer (planktonic)	Partly cemented fracture
Parallel lamination	Foraminifer (large benthic)	Phosphatic nodule
Slump fold	Foraminifer (small benthic)	Pyrite (disseminated)
Solution cavity/surface		Pyrite nodule
Wavy lamination		
Wavy strata		

Core disturbance	Boundary contact	Facies
Biscuit	Bioturbated	Pelagic
Brecciated	Erosive	Hemipelagic
Fall-in	Gradational	Neritic
Flow-in	Hardground	Littoral
Fractured	Scoured	
Fragmented	Sharp	
Mixed	Wavy	
Soupy		
Void		

tional facies between pelagic and neritic. Because of the continental margin setting and the strong influence of carbonate platform sedimentation at all Expedition 356 sites, virtually all nonneritic sediments were deemed to be hemipelagic.

Neritic facies. Neritic sediments consist of coarse- to fine-grained particles originating in shallow-water areas (e.g., inner to outer ramp) and consisting mostly of skeletal (i.e., bioclastic) carbonate components, nonskeletal grains, and micrite. The term micrite defines very fine calcareous particles (<20 μm) of various origins. Neritic carbonate grains (as described by Tucker and Wright, 1990) observed during Expedition 356 had two origins:

Skeletal components = these include the remains of large and small benthic foraminifers, bivalves, bryozoans, coralline algae, corals, echinoderms, gastropods, minor green algae, and planktonic foraminifers; rhodoliths consisting of gravel-sized, subspherical nodules of concentrically encrusted coralline algae were also present.

Nonskeletal components = minor intraclasts and lithoclasts were occasionally encountered; thin sections were used to identify the nature of these nonskeletal components because ooids and peloids were difficult to distinguish by eye in the core.

Littoral facies. Littoral sediments are deposited close to the marine shoreline. The term was mainly used during Expedition 356 to refer to sediments deposited in the inter- and supratidal zones. These sediments consist mainly of dolostones and dolomitic limestones with solution cavities or surfaces, algal laminites, and evaporitic minerals.

Drilling disturbance

Six types of drilling/coring disturbance were described using the following terms:

- Fall-in = displaced material from higher in the hole that has fallen downhole onto the top surface of a core.
- Biscuit = sediments of intermediate stiffness showing vertical variations in the degree of disturbance; softer intervals are washed and/or soupy, whereas firmer intervals are relatively undisturbed.
- Fractured = firm sediments broken into pieces that remain in place and may be partly displaced from their original orientation.
- Fragmented = firm sediments broken into pieces that are often displaced or rotated.
- Flow-in = soft-sediment stretching and/or compressional shearing structures attributed to coring/drilling; this can include

the presence of coring/drilling slurry; the particular type of deformation may also be noted.

Soupy = intervals are water saturated and have lost aspects of original bedding.

Mixed = sediments are entirely or partially homogenized along core (up or down).

Void = interval with no core material due the coring process (different from a diagenetic dissolution cavity).

Four relatively subjective terms were used to describe the intensity of disturbance types:

Slightly disturbed = bedding contacts are only partially deformed or core pieces are broken but in place and kept their original orientation.

Moderately disturbed = bedding contacts have undergone strong bowing or core pieces are partly displaced from their original orientation.

Severe = bedding is completely deformed, or some core pieces may not be in correct stratigraphic position and may not represent the entire sequence, and/or original orientation is lost.

Destroyed = intervals have lost all signs of original bedding, orientation, and stratigraphic position; core pieces are often mixed with drilling slurry; core liner may even be damaged or destroyed.

Smear slides

Smear slides provided information on the composition and grain size of fine-fraction sediments by giving a semiquantitative estimate of proportions of fine-fraction components. Smear slide samples were collected from the working half of most cores. At least two samples were taken per full core (one for half cores) and were co-located with the moisture and density (MAD) samples where possible (see [Physical properties](#)). For cores with complex lithologies, the dominant lithology was sampled. Additional smear slides were taken to assist with the classification of grainstones (e.g., confirming the absence of mud) and from areas of interest (e.g., skeletal carbonates and lithologic changes). Duplicates of cored intervals were sampled for smear slide analysis to assist with the definition of lithologic boundaries or the correlation of lithologic units between holes.

Smear slides were prepared either by using a toothpick to collect a small amount of unlithified sediment or by using a spatula to scrape material from partially lithified and lithified sediment. Sediments consisting primarily of sand and larger grain sizes were not sampled for smear slides. The sediment sample was placed on a 2.5 cm × 7.5 cm glass slide, homogenized with a drop of deionized water, and spread evenly across the slide to create a very thin (<50 μm), uniform layer of sediment. The slide was placed on a hot plate to evaporate the water. Once dry, a glass coverslip was fixed to the slide using a drop of Norland optical adhesive, taking care to avoid trapping air bubbles under the coverslip. Finally, the slide was placed in a UV light box for ~15 min to cure the adhesive.

Smear slides were examined with a Zeiss Axioskop transmitted-light microscope equipped with a standard eyepiece micrometer and a digital camera. The texture of siliciclastic and carbonate components (relative abundance of sand-, silt-, and clay-sized grains) and the presence and proportions of biogenic and mineral components were recorded and entered into DESClogik. Grain size definitions follow Wentworth (1922) (Figure [F4](#)):

Clay = <4 μm.

Silt = 4–63 μm.

Sand = >63 μm.

Micrite in carbonate samples was defined as <20 μm following Dunham (1962), to ensure consistent definitions between macro- and microdescriptions.

Smear slides were used to identify major minerals within a sample. Although smear slide analyses cannot definitively identify all mineral components, they can differentiate quartz, feldspar, mica, calcite (separated into micrite and sparite), dolomite, opaque sulfides and oxides, glauconite, peloids, and ooids. The mineralogy of clay-sized grains could not be determined from smear slides.

Smear slides were also used to identify whole and fragmented microfossils, including dinoflagellate cysts, diatoms, silicoflagellates, radiolarians, sponge spicules, ostracods, calcareous nanofossils, echinoid spines, benthic and planktonic foraminifers, algae, bryozoan and mollusk fragments, plant fragments (including pollen), and fish debris.

The relative abundances of minerals and the total fossil content were estimated using the visual percentage charts of Rothwell (1989). Note that smear slide analyses tend to underestimate the amount of sand-sized and larger grains because these grains are difficult to incorporate onto the slide.

Thin section petrography

Thin sections were analyzed using a Zeiss Axioplan microscope equipped with a digital camera. Observations were recorded on a customized spreadsheet and uploaded into the LIMS system.

XRD analysis

XRD analyses were used as a diagnostic tool to identify and semiquantitatively analyze the relative content of mineral phases in bulk samples. XRD samples were selected based on visual core observations (e.g., changes in color, lithology, and texture). A 2.5 cm³ sample was taken. Samples for bulk mineralogy analyses were freeze-dried and ground by hand (soft sediment) or in an agate ball mill (rock) as necessary.

The XRD samples were then top-mounted onto a sample holder and analyzed using a Bruker ASX D-4 Endeavor X-ray diffractometer mounted with a Vantec-1 detector using nickel-filtered CuKα radiation.

The standard locked coupled scan was

Voltage = 40 kV,

Current = 40 mA,

Goniometer scan = 4°–70°2θ,

Step size = 0.0087°2θ,

Scan speed = 0.2 s/step, and

Divergence slit = 0.3 mm.

The external corundum standard NIST 176 was measured periodically to monitor data quality.

Diffractograms of bulk samples were evaluated using the DIFFRACplus EVA software package, which allowed for mineral identification and basic peak characterization (e.g., baseline removal and maximum peak intensity). Files were created containing d-spacing values, diffraction angles, and peak intensities with background removed. These files were scanned by the EVA software to find d-spacing values characteristic of a limited range of minerals.

Once minerals were identified by their peak heights, I/I_{corundum} values from the International Centre for Diffraction Data PDF data-

base were used as a semiquantitative measure of their relative percentages. If quartz was present, it was used as an internal standard, and the measured quartz major peak d-spacing was adjusted to align with the known quartz major peak d-spacing. All other mineral phases were adjusted accordingly. Where dolomite was present in a sample, the MgCO_3 content of dolomite was calculated based on the d-value of the [104] peak (Lumsden, 1979).

Digital files with the diffraction patterns are available from the LIMS database (<http://web.iodp.tamu.edu/LORE/>).

XRF analysis

XRF analyses were used to investigate the composition of sediments. XRF was measured with a handheld Thermo-Niton XL3t GOLDD+ instrument, placed directly at the face of the split core or selected sample (in situ sampling). The instrument is equipped with an Ag anode and a large-area drift detector for energy-dispersive X-ray analysis. The detector is nominally Peltier cooled to -27°C , which is achieved within 1–2 min after powering up. X-ray ranges and corresponding filters were preselected by the instrument software as “light” (e.g., Mg, Al, and Si), “low” (e.g., Ca, K, Ti, Mn, and Fe), “main” (e.g., Rb, Sr, Y, and Zr), and “high” (e.g., Ba and Th). Spectrum acquisition was limited to the main-, low-, and light-energy range (30 s integration time each) because elements measured in the high mode were generally near the limit of detection or unreliable. The “Mining” profile uses generator settings of 50 kV, a current of 40 mA, and a sampling time of 90 s.

Two factory-set modes for spectrum quantification were piloted for Hole U1459B samples. Seven samples were run on the “Soil” profile, which reports measurements in parts per million for the elements Si, K, Ca, Zr, Sr, and Sc. Four samples were measured on the Mining profile, which includes a fundamental parameter calibration that accounts for the matrix effects for the elements analyzed in the spectrum. The Mining profile reports the elements Si, Al, K, Ca, Mg, Fe, Zr, Sr, and Sc and was used for Expedition 356 XRF samples because it reported a wider range of useful elements for diagnosing sediment composition (based on pilot data).

Note that for Hole U1459B, the Mining profile results in Table T7 in the Site U1459 chapter (Gallagher et al., 2017) (the pilot data) were converted to parts per million for comparison with the Soil profile data.

Image logging

Prior to macroscopic analysis, archive halves of sediment cores were photographed using the SHIL, which is fitted with a CV-L107CL 3CCD high-speed color line-scan camera. The line-scan camera uses three 2048 pixel line sensors mounted on a prism for the red (R), green (G), and blue (B) channels, and it operates with a 40 MHz pixel clock that allows for a maximum line rate of 19,047 lines/s. The SHIL is equipped with a mounted lighting system that moves with the camera and is specifically designed to light the surface of section halves evenly and to prevent shadows being cast where surfaces are uneven. The SHIL photographs one core section at a time, automatically uploading TIF and JPEG files to the LIMS database. Immediately after scanning, the JPEG file is manually cropped to remove the edges of the core liner, creating a publication-ready photograph. This cropped JPEG is also uploaded to the LIMS database. Prior to scanning, some section halves were dewatered (i.e., standing water removed by syringe) and/or dried (i.e.,

dabbed with paper towel) to reduce light reflectance and interference.

Spectrophotometry

Reflectance of visible light from the archive halves of sediment cores was measured using an Ocean Optics USB4000 spectrophotometer mounted on the automated SHMSL (see also [Physical properties](#)). For Sites U1458–U1463, freshly split soft, wet cores were covered with clear plastic wrap and placed on the SHMSL. For Site U1464, a measurement issue (not detected for the other sites) arose because of a discrepancy in the use of the clear plastic wrap. To account for and eliminate this issue, all section halves (both wet and dry) at Site U1464 were covered in clear plastic wrap prior to being measured by the SHMSL. Measurements were taken every 2.5 cm to provide a high-resolution stratigraphic record of color variations for visible wavelengths. Each measurement was recorded in 2 nm wide spectral bands from 380 to 900 nm. Raw data were automatically normalized by the logger software and reported as three reflectance parameters: lightness (L^*), the ratio of red to green reflectance (a^*), and the ratio of yellow to blue reflectance (b^*).

The SHMSL takes measurements in empty intervals and over intervals where the core surface is well below the level of the core liner, but it cannot recognize relatively small cracks, disturbed areas of core, or plastic section dividers. Thus, SHMSL data may contain spurious measurements that need to be edited from the data set. Any foam spacers in core section halves (indicating voids in recovery or samples removed [e.g., by the paleontology group]) were removed prior to scanning because scanning these spacers also yields inaccurate measurements. Foam spacers were returned to section halves prior to macroscopic examination. See Balsam et al. (1997, 1998) and Balsam and Damuth (2000) for additional details about the measurement and interpretation of spectral data. All data measured by the SHMSL (spectrophotometry and MS) were uploaded to the LIMS database at the time of scanning. MS measurements were also made on the SHMSL and plotted on VCDs (see below). The MS methods are described in [Physical properties](#).

Visual core descriptions

Ultimately, data from the sediment and rock descriptions were compiled into one VCD sheet per core, and these were summarized for each hole and site to visualize lithologic changes. The core and hole visual core description summaries were combined with other downhole descriptions (e.g., lithification, fossils, structures, and core recovery) and with data from smear slides, thin sections, XRD and XRF analyses, and the $L^*a^*b^*$ image scans. These combined data were used to define lithologic units and subunits for each site. Visual core description site summary figures were then produced showing the parameters used to define the main features of lithologic units and to give an overview of the key changes downhole. Information displayed in the VCDs are summarized in Table T1, although not all information is presented in every visual core description hole or site summary figure. VCD symbols are illustrated in Figures F6 and F7.

Smear slide description sheets were summarized by hole and site. The smear slide description summaries show smear slide sample locations in relation to the major lithologic units, grain size estimates, and estimates of the percentages of constituents in the smear slides. Smear slide summaries are provided in each site chapter, al-

Table T1. Specific elements displayed in visual core description (VCD) columns, Expedition 356. [Download table in .csv format.](#)

Parameter	Description
Meters	Calculated composite depth below seafloor (CSF-A) of the core.
Core sections	Each core was cut into 1.5 m sections (or less depending on the percent recovery) and numbered according to IODP convention. The core and section number are listed.
Drilling disturbance	Drilling disturbance features are indicated with symbols (Figure F6).
Lithification	A visualization of the state of sediment or rock lithification.
Lith. unit	Boundaries and numbering of major lithologic units defined downhole.
Samples	Samples taken from each core: SS = smear slide, TS = thin section, PAL = micropaleontology, DCP = close-up photo, IW = interstitial water, XRD = X-ray diffraction, XRF = X-ray fluorescence.
Core image	Stitched digital photography from the Section Half Imaging Logger (SHIL).
Graphic lithology	Lithologies are represented by patterns (Figure F7). Single lithologies occupy the full column width. Mixed lithologies are indicated by splitting the graphic symbol vertically, with the center 1/3 of the total width of the column representing the principal name, the left 1/3 of the column representing the major modifier, and the right 1/3 of the column representing the minor modifier.
Texture	Textural classifications (Figure F3) are represented by a plot of the texture rank (Dunham classification number). For siliciclastic or dolostone where texture was lost, this column is left blank. Dunham (1962) texture classifications are also displayed in the graphic lithology column with the "limestone" symbol and different colors representing the different textures.
Other features	Columns showing lithologic boundaries, structures, diagenesis, fossils, color, bioturbation, layer or bed thicknesses, and facies are displayed on the VCDs using patterns and symbols (Figures F6, F7). Only those features that helped define lithologic units or features of interest are displayed.
Smear slide results	Summary smear slide data are given in more detail in the smear slide description sheets.
Multisensor Logger Data (SHMSL)	Spectrophotometer and magnetic susceptibility core logger data.
Natural gamma radiation (NGR)	Natural Gamma Radiation Logger (NGRL) data (see Physical properties) are used to augment geologic interpretation.
Core summary	A written summary of the lithologies present in each core.

Figure F7. Lithology patterns used in visual core and smear slide descriptions, Expedition 356.



though the parameters selected for display vary among sites, depending on changes in their downhole profile.

Biostratigraphy and micropaleontology

Calcareous nannofossils and planktonic and benthic foraminifers were studied in core catcher samples at all sites. Samples from core sections were also examined when a more refined age determination was necessary or a significant change in lithostratigraphy occurred. Nannofossils and planktonic foraminifers were used for biostratigraphy, and benthic foraminifers were mainly used to acquire estimates of paleobathymetry.

Calcareous nannofossils

Calcareous nannofossil assemblages were examined and described from standard smear slides made from core catcher (CC) samples at 10–20 m intervals and from mudline samples at each site and in multiple holes. Additional toothpick samples were taken between core catcher samples from split-core sections when necessary to refine the stratigraphic position of bioevents.

Standard smear slides were made from bulk sediment. In cases of coarse sand or strongly lithified sediments, the sample was suspended in distilled water and sonicated before an aliquot of the suspension was left to settle and dry on a coverslip. Slides were fixed with Norland optical adhesive and cured under UV light for immediate biostratigraphic examination using a Zeiss Axioscope. Samples were analyzed under (cross) polarized light using oil immersion at a magnification of 1000 \times . All photomicrographs were taken using a Spot RTS system with the IODP Image Capture and Spot commercial software. Additional observations with the scanning electron microscope (SEM) were made to identify *Emiliania huxleyi* and verify the preservational state of calcareous nannofossils. The semiquantitative abundance of all species encountered was described (see below) and notes were taken on the (abiotic) fine-grained matrix (e.g., micrite and dolomite grains).

Nannofossil taxonomy followed Perch-Nielsen (1985) and Young (1998), as compiled in the online Nannotax 3 (<http://ina.tmsoc.org/Nannotax3>) and the shipboard Nannoware (Bugware, Inc. 2002) databases. The zonal scheme of Martini (1971) was used to report on the Neogene (NN code) and Paleogene (NP code) calcareous nannofossil biostratigraphy (Figure F8; Table T2). This zonation represents a general framework for the biostratigraphic classification of middle- to low-latitude nannofossil assemblages. In addition, we consulted the Neogene zonal schemes of Okada and Bukry (1980) (CN code) and Backman et al. (2012) (CNPL and CNM codes) (Figure F8). The CNPL and CNM zonations are based on numerous high-resolution quantitative nannofossil assemblage data from low-latitude deep-sea sediments (Backman et al., 2012). Finally, the Paleogene biozonation of Agnini et al. (2014) was consulted for additional biostratigraphic constraints in Hole U1459C. All datum ages used herein are calibrated to the geological time-scale of Gradstein et al. (2012) (GTS2012) (Table T2).

We use base and top, respectively, to describe the stratigraphic lowest and highest occurrences of nannofossil taxa (Figure F8). The base of *E. huxleyi* denotes the youngest biozone (<0.29 Ma; NN21) sampled during Expedition 356. The top of *Pseudoemiliania lacunosa* (0.44 Ma) and the top of *Discoaster brouweri* (1.93 Ma) bracket the Middle Pleistocene–late early Pleistocene. The biostratigraphic range of *Reticulofenestra asanoi* (1.14–0.91 Ma) and the top of *Calcidiscus macintyreii* (1.6 Ma) were consistently recorded within this time interval. The Pliocene/Pleistocene bound-

ary (2.58 Ma; Gradstein et al., 2012) falls within the top part of Biozone NN16 and is approximated by the top of *Discoaster surculus* (2.49 Ma). The tops of *Sphenolithus* spp. (3.54 Ma) and *Reticulofenestra pseudoumbilicus* (3.7 Ma) were useful datums to correlate late early Pliocene strata between all the Expedition 356 sites. The late Miocene and early Pliocene marker species *Amaurolithus* and *Ceratolithus* were absent or rarely encountered in Expedition 356 samples, limiting our nannofossil biostratigraphic constraints for the Miocene/Pliocene boundary (5.3 Ma, within Biozone NN12; Gradstein et al., 2012). However, the top of *Discoaster quinqueramus* (5.59 Ma) and the top of *Reticulofenestra rotaria* (at the Subchron C3An.1n/C3An.1r reversal boundary; compare Young [1998]; 6.252 Ma) (Figure F8) proved useful datums to identify late Miocene, Messinian-aged strata (upper part of Biozone NN11).

The following coding was used in the DESClogik spreadsheet program and uploaded into the LIMS database.

Total calcareous nannofossil abundance (all codes cf. [A22]) within the sediment was recorded using the following criteria:

- D = dominant (>90% of sediment particles).
- A = abundant (>50%–90% of sediment particles).
- C = common (>10%–50% of sediment particles).
- F = few (1%–10% of sediment particles).
- R = rare (<1% of sediment particles).
- B = barren (none present).

Abundance of individual calcareous nannofossil taxa was recorded using the following criteria:

- V = very abundant (>100 specimens per field of view [FOV] at 1000 \times magnification).
- A = abundant (10–100 specimens per FOV at 1000 \times magnification).
- C = common (1–9 specimens per FOV at 1000 \times magnification).
- F = few (1 specimen per 2–10 FOV at 1000 \times magnification).
- R = rare (1 specimen per 11–100 FOV at 1000 \times magnification).
- P = present (1 specimen per >100 FOV at 1000 \times magnification).

Preservation of calcareous nannofossils was recorded using the following criteria:

- VG = very good (no evidence of dissolution and/or recrystallization, no alteration of primary morphological characteristics, and specimens identifiable to the species level).
- G = good (little or no evidence of dissolution and/or recrystallization, primary morphological characteristics unaltered or only slightly altered, and specimens were identifiable to the species level).
- M = moderate (specimens exhibit some etching and/or recrystallization, primary morphological characteristics somewhat altered, and most specimens were identifiable to the species level).
- P = poor (specimens were severely etched or overgrown, primary morphological characteristics largely destroyed, fragmentation has occurred, and specimens often could not be identified at the species and/or generic level).

Foraminifers

Core catcher and mudline samples were prepared and analyzed for benthic and planktonic foraminifers. Core catcher samples of 5–10 cm³ were soaked in a hydrogen peroxide solution (30%) when necessary, heated on a hot plate (~90°C), and washed over 63 and 150 μ m mesh sieves. Lithified samples were gently broken with a

Figure F8. Biostratigraphic framework used during Expedition 356. All biostratigraphic datums for planktonic foraminifers and nanofossils are calibrated to GTS2012 (Gradstein et al., 2012). Bold = main events found during Expedition 356. For calcareous nanofossils, the zonal schemes of Martini (1971) (NN code, as referenced in all site chapters), Okada and Bukry (1980) (CN code), and Backman et al. (2012) (CNPL and CNM codes) are indicated for comparison.

GTS2012
Neogene

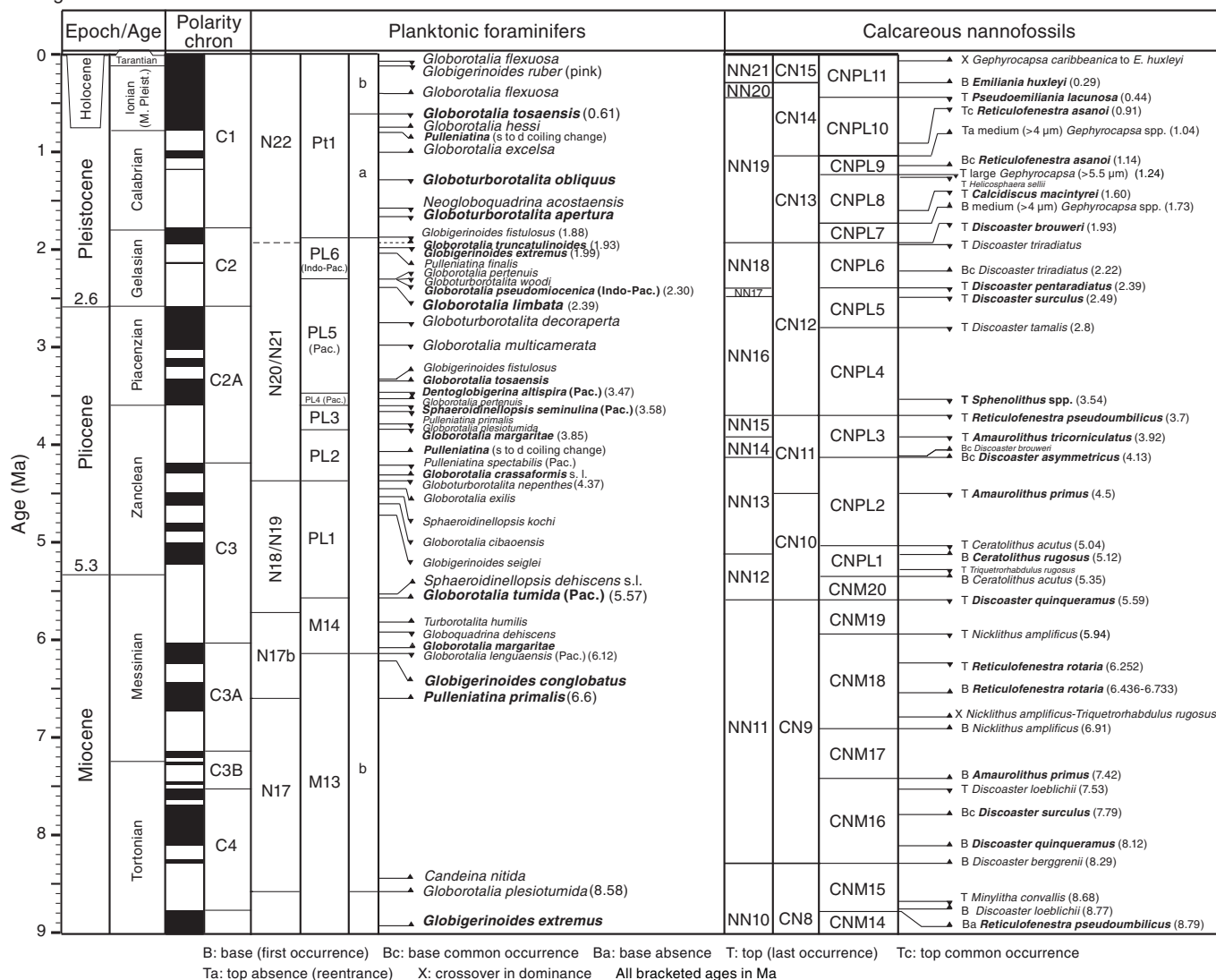


Table T2. Biostratigraphic event datums for calcareous nanofossils based on Gradstein et al. (2012), Expedition 356. B = base (first occurrence), Ba = base absence, Bc = base common occurrence, T = top (last occurrence), Ta = top absence (reentrance), Tc = top common occurrence, Td = top dominance, X = crossover in dominance. Bold = boundary age. (Continued on next three pages.) [Download table in .csv format.](#)

Zone base (Martini, 1971; Sissingh, 1977)	Zone base (Okada and Bukry, 1980; Roth, 1978)	Species event	GTS2012 age (Ma)	Calibration reference		
NN21	CN15	X <i>Gephyrocapsa caribbeanica</i> – <i>E. huxleyi</i>	0.09	Gradstein et al., 2012		
		B <i>Emiliania huxleyi</i>	0.29	Gradstein et al., 2012		
		T <i>Pseudoemiliania lacunosa</i>	0.44	Gradstein et al., 2012		
		Tc <i>Reticulofenestra asanoi</i>	0.91	Gradstein et al., 2012		
		Td small <i>Gephyrocapsa</i> spp.	1.02	Gradstein et al., 2012		
		B <i>Gephyrocapsa omega</i>	1.02	Gradstein et al., 2012		
		Ta (reentrance) medium <i>Gephyrocapsa</i> spp.	1.04	Gradstein et al., 2012		
		Bc <i>Reticulofenestra asanoi</i>	1.14	Gradstein et al., 2012		
		T large <i>Gephyrocapsa</i> spp. (>5.5 μm)	1.24	Gradstein et al., 2012		
		Bc small <i>Gephyrocapsa</i> spp.	1.24	Gradstein et al., 2012		
NN20	CN14a	T <i>Helicosphaera sellii</i>	1.26	Gradstein et al., 2012		
		B large <i>Gephyrocapsa</i> spp.	1.46	Gradstein et al., 2012		
		T <i>Calcidiscus macintyre</i>	1.6	Gradstein et al., 2012		
		B medium (>4 μm) <i>Gephyrocapsa</i> spp.	1.73	Gradstein et al., 2012		
		CN13b	CN14a	T <i>Discoaster brouweri</i>	1.93	Gradstein et al., 2012
				T <i>Discoaster triradiatus</i>	2.22	Gradstein et al., 2012
				T <i>Discoaster pentaradiatus</i>	2.39	Gradstein et al., 2012
				T <i>Discoaster surculus</i>	2.49	Gradstein et al., 2012
				T <i>Discoaster tamalis</i>	2.8	Gradstein et al., 2012
				T <i>Sphenolithus</i> spp.	3.54	Gradstein et al., 2012
NN15	CN11	T <i>Reticulofenestra pseudoumbilicus</i>	3.7	Gradstein et al., 2012		
		T <i>Amaurolithus tricorniculatus</i>	3.92	Gradstein et al., 2012		
		Bc <i>Discoaster brouweri</i>	4.13	Gradstein et al., 2012		
		Bc <i>Discoaster asymmetricus</i>	4.13	Gradstein et al., 2012		
		T <i>Amaurolithus primus</i>	4.5	Gradstein et al., 2012		
		NN12	CN10	T <i>Ceratolithus acutus</i>	5.04	Gradstein et al., 2012
				B <i>Ceratolithus rugosus</i>	5.12	Gradstein et al., 2012
				T <i>Triquetrorhabdulus rugosus</i>	5.35	Gradstein et al., 2012
				B <i>Ceratolithus acutus</i>	5.35	Gradstein et al., 2012
				T <i>Discoaster quinqueramus</i>	5.59	Gradstein et al., 2012
NN11	CN9			T <i>Nicklithus amplifucus</i>	5.94	Gradstein et al., 2012
				T <i>Reticulofenestra rotaria</i>	6.252	Gradstein et al., 2012
				B <i>Reticulofenestra rotaria</i>	6.436–6.733	Gradstein et al., 2012
				X <i>Nicklithus amplifucus</i> – <i>Triquetrorhabdulus rugosus</i>	6.91	Gradstein et al., 2012
				B <i>Nicklithus amplifucus</i>	6.91	Gradstein et al., 2012
		NN10	CN8	B <i>Amaurolithus primus</i>	7.42	Gradstein et al., 2012
				T <i>Discoaster loeblichii</i>	7.53	Gradstein et al., 2012
				Bc <i>Discoaster surculus</i>	7.79	Gradstein et al., 2012
				B <i>Discoaster quinqueramus</i>	8.12	Gradstein et al., 2012
				B <i>Discoaster berggrenii</i>	8.29	Gradstein et al., 2012
T <i>Minylitha convallis</i>	8.68			Gradstein et al., 2012		
B <i>Discoaster loeblichii</i>	8.77			Gradstein et al., 2012		
Ba <i>Reticulofenestra pseudoumbilicus</i>	8.79			Gradstein et al., 2012		
NN10	CNM14			T <i>Minylitha convallis</i>	8.68	Gradstein et al., 2012
				B <i>Discoaster loeblichii</i>	8.77	Gradstein et al., 2012
		Ba <i>Reticulofenestra pseudoumbilicus</i>	8.79	Gradstein et al., 2012		

Table T2 (continued). (Continued on next page.)

Zone base (Martini, 1971; Sissingh, 1977)	Zone base (Okada and Bukry, 1980; Roth, 1978)	Species event	GTS2012 age (Ma)	Calibration reference
NN19	CN13a	T <i>Discoaster brouweri</i>	1.93	Gradstein et al., 2012
		T <i>Discoaster triradiatus</i>	1.95	Gradstein et al., 2012
		Bc <i>Discoaster triradiatus</i>	2.22	Gradstein et al., 2012
NN18	CN12d	T <i>Discoaster pentaradiatus</i>	2.39	Gradstein et al., 2012
NN17	CN12c	T <i>Discoaster surculus</i>	2.49	Gradstein et al., 2012
	CN12b	Pliocene/Pleistocene boundary	2.59	Gradstein et al., 2012
		T <i>Discoaster tamalis</i>	2.8	Gradstein et al., 2012
NN16	CN12a	T <i>Sphenolithus</i> spp.	3.54	Gradstein et al., 2012
NN15		T <i>Reticulofenestra pseudoumbilicus</i>	3.7	Gradstein et al., 2012
		T <i>Amaurolithus tricorniculatus</i>	3.92	Gradstein et al., 2012
NN14	CN11b	Bc <i>Discoaster brouweri</i>	4.12	Gradstein et al., 2012
	CN11a	Bc <i>Discoaster asymmetricus</i>	4.13	Gradstein et al., 2012
NN13	CN10c	T <i>Amaurolithus primus</i>	4.5	Gradstein et al., 2012
		T <i>Ceratolithus acutus</i>	5.04	Gradstein et al., 2012
		B <i>Ceratolithus rugosus</i>	5.12	Gradstein et al., 2012
		T <i>Triquetrorhabdulus rugosus</i>	5.28	Gradstein et al., 2012
		Pliocene/Miocene boundary	5.33	Gradstein et al., 2012
NN12	CN10b	B <i>Ceratolithus larrymayeri</i>	5.34	Gradstein et al., 2012
		B <i>Ceratolithus acutus</i>	5.35	Gradstein et al., 2012
	CN9d	T <i>Discoaster quinqueramus</i>	5.59	Gradstein et al., 2012
	CN9c	T <i>Nicklithus amplificus</i>	5.94	Gradstein et al., 2012
		X <i>Nicklithus amplificus</i> – <i>Triquetrorhabdulus rugosus</i>	6.79	Gradstein et al., 2012
NN11	CN9a	B <i>Nicklithus amplificus</i>	6.91	Gradstein et al., 2012
		B <i>Amaurolithus primus</i> , <i>Amaurolithus</i> spp.	7.42	Gradstein et al., 2012
		Bc <i>Discoaster loeblichii</i>	7.53	Gradstein et al., 2012
		Bc <i>Discoaster surculus</i>	7.79	Gradstein et al., 2012
		B <i>Discoaster quinqueramus</i>	8.12	Gradstein et al., 2012
		B <i>Discoaster berggrenii</i>	8.29	Gradstein et al., 2012
		T <i>Minylitha convallis</i>	8.68	Gradstein et al., 2012
		B <i>Discoaster loeblichii</i>	8.77	Gradstein et al., 2012
		Ba <i>Reticulofenestra pseudoumbilicus</i>	8.79	Gradstein et al., 2012
		T <i>Discoaster bollii</i>	9.21	Gradstein et al., 2012
NN10	CN8	Bc <i>Discoaster pentaradiatus</i>	9.37	Gradstein et al., 2012
		T <i>Discoaster hamatus</i>	9.53	Gradstein et al., 2012
		T <i>Catinaster calyculus</i>	9.67	Gradstein et al., 2012
		T <i>Catinaster coalitus</i>	9.69	Gradstein et al., 2012
		B <i>Minylitha convallis</i>	9.75	Gradstein et al., 2012
		X <i>Discoaster hamatus</i> – <i>Discoaster neohamatus</i>	9.76	Gradstein et al., 2012
		B <i>Discoaster bellus</i>	10.4	Gradstein et al., 2012
		X <i>Catinaster calyculus</i> – <i>Catinaster coalitus</i>	10.41	Gradstein et al., 2012
		B <i>Discoaster neohamatus</i>	10.52	Gradstein et al., 2012
		B <i>Discoaster hamatus</i>	10.55	Gradstein et al., 2012
NN9	CN7	Bc <i>Helicosphaera stalis</i>	10.71	Gradstein et al., 2012
		Tc <i>Helicosphaera walbersdorfensis</i>	10.74	Gradstein et al., 2012
		B <i>Discoaster brouweri</i>	10.76	Gradstein et al., 2012
		B <i>Catinaster calyculus</i>	10.79	Gradstein et al., 2012
		B <i>Catinaster coalitus</i>	10.89	Gradstein et al., 2012
NN8	CN6	T <i>Coccolithus miopelagicus</i>	10.97	Gradstein et al., 2012
		T <i>Calcidiscus premacintyreii</i>	11.21	Gradstein et al., 2012
		Tc <i>Discoaster kugleri</i>	11.58	Gradstein et al., 2012
		T <i>Cyclicargolithus floridanus</i>	11.85	Gradstein et al., 2012
		Bc <i>Discoaster kugleri</i>	11.9	Gradstein et al., 2012
NN7	CN5b	T <i>Coronocyclus nitescens</i>	12.12	Gradstein et al., 2012
		Tc <i>Calcidiscus premacintyreii</i>	12.38	Gradstein et al., 2012
		Bc <i>Calcidiscus macintyreii</i>	12.46	Gradstein et al., 2012
		B <i>Reticulofenestra pseudoumbilicus</i>	12.83	Gradstein et al., 2012
		B <i>Triquetrorhabdulus rugosus</i>	13.27	Gradstein et al., 2012
		Tc <i>Cyclicargolithus floridanus</i>	13.28	Gradstein et al., 2012
		B <i>Calcidiscus macintyreii</i>	13.36	Gradstein et al., 2012
NN6	CN5a	T <i>Sphenolithus heteromorphus</i>	13.53	Gradstein et al., 2012
NN5	CN4	T <i>Helicosphaera ampliaperta</i>	14.91	Gradstein et al., 2012
		Ta <i>Discoaster deflandrei</i> group	15.8	Gradstein et al., 2012
		B <i>Discoaster signus</i>	15.85	Gradstein et al., 2012
NN4	CN3	B <i>Sphenolithus heteromorphus</i>	17.71	Gradstein et al., 2012
		T <i>Sphenolithus belemnus</i>	17.95	Gradstein et al., 2012

Table T2 (continued). (Continued on next page.)

Zone base (Martini, 1971; Sissingh, 1977)	Zone base (Okada and Bukry, 1980; Roth, 1978)	Species event	GTS2012 age (Ma)	Calibration reference
NN3	CN2	<i>T Triquetrorhabdulus carinatus</i>	18.28	Gradstein et al., 2012
		<i>B Sphenolithus belemnus</i>	19.03	Gradstein et al., 2012
		<i>B Helicosphaera ampliapertura</i>	20.43	Gradstein et al., 2012
		<i>X Helicosphaera euphratis–Helicosphaera carteri</i>	20.92	Gradstein et al., 2012
		<i>Bc Helicosphaera carteri</i>	22.03	Gradstein et al., 2012
		<i>T Orthorhabdulus serratus</i>	22.42	Gradstein et al., 2012
		<i>B Sphenolithus disbelemnus</i>	22.76	Gradstein et al., 2012
		<i>B Discoaster druggi</i> (sensu stricto)	22.82	Gradstein et al., 2012
		<i>T Sphenolithus capricornutus</i>	22.97	Gradstein et al., 2012
		NN2	CN1c	Miocene/Oligocene boundary
<i>T Sphenolithus delphix</i>	23.11			Gradstein et al., 2012
NN1	CN1a-b	<i>T Reticulofenestra bisecta</i>	23.13	Gradstein et al., 2012
		<i>B Sphenolithus delphix</i>	23.21	Gradstein et al., 2012
		<i>T Zygrhablithus bijugatus</i>	23.76	Gradstein et al., 2012
		<i>T Sphenolithus ciproensis</i>	24.43	Gradstein et al., 2012
		<i>Tc Cyclicargolithus abisectus</i>	22.67	Gradstein et al., 2012
		<i>X Triquetrorhabdulus lungus–Triquetrorhabdulus carinatus</i>	24.67	Gradstein et al., 2012
		<i>T Chiasmolithus altus</i>	25.44	Gradstein et al., 2012
		<i>Bc Triquetrorhabdulus carinatus</i>	26.57	Gradstein et al., 2012
		<i>T Sphenolithus distentus</i>	26.84	Gradstein et al., 2012
		<i>T Sphenolithus predistentus</i>	26.93	Gradstein et al., 2012
NP25	CP19b	<i>T Sphenolithus pseudoradians</i>	28.73	Gradstein et al., 2012
NP24	CP19a	<i>B Sphenolithus ciproensis</i>	29.62	Gradstein et al., 2012
		<i>B Sphenolithus distentus</i>	30.00	Gradstein et al., 2012
NP23	CP17	<i>T Reticulofenestra umbilicus</i>	32.02	Gradstein et al., 2012
		<i>T Coccolithus formosus</i>	32.92	Gradstein et al., 2012
NP22	CP16c	<i>Ta Clausiococcus subdistichus</i>	33.43	Gradstein et al., 2012
		Oligocene/Eocene boundary	33.89	Gradstein et al., 2012
NP21	CP16a	<i>T Discoaster saipanensis</i>	34.44	Gradstein et al., 2012
		<i>T Discoaster barbadiensis</i>	34.76	Gradstein et al., 2012
NP20–NP19	CP16a	<i>T Reticulofenestra reticulata</i>	35.40	Gradstein et al., 2012
		<i>B Isthmolithus recurvus</i>	36.97	Gradstein et al., 2012
		<i>B Chiasmolithus oamaruensis</i>	37.32	Gradstein et al., 2012
		<i>T Chiasmolithus grandis</i>	37.98	Gradstein et al., 2012
NP18	CP15	<i>B Chiasmolithus oamaruensis</i>	38.09	Gradstein et al., 2012
		<i>B Reticulofenestra bisecta</i>	38.25	Gradstein et al., 2012
NP17	CP14b	<i>T Chiasmolithus solitus</i>	40.4	Gradstein et al., 2012
		<i>B Reticulofenestra reticulata</i>	41.66	Gradstein et al., 2012
NP16	CP14a	<i>T Nannotetrina</i> spp.	41.85	Gradstein et al., 2012
		<i>T Nannotetrina fulgens</i>	42.87	Gradstein et al., 2012
NP15c	CP13c	<i>B Reticulofenestra umbilicus</i>	43.32	Gradstein et al., 2012
		<i>T Chiasmolithus gigas</i>	44.12	Gradstein et al., 2012
NP15b	CP13b	<i>B Chiasmolithus gigas</i>	45.49	Gradstein et al., 2012
		<i>T Discoaster sublodoensis</i> (5-rayed)	46.21	Gradstein et al., 2012
NP15a	CP13a	<i>B Nannotetrina fulgens</i>	46.29	Gradstein et al., 2012
		<i>T Discoaster lodoensis</i>	47.41	Gradstein et al., 2012
		<i>T Blackites piriformis</i>	47.73	Gradstein et al., 2012
		<i>B Nannotetrina cristata, Nannotetrina</i> spp.	47.73	Gradstein et al., 2012
NP14b	CP12b	<i>B Blackites inflatus</i>	47.84	Gradstein et al., 2012
		<i>B Blackites piriformis</i>	47.94	Gradstein et al., 2012
NP14a	CP12a	<i>B Discoaster sublodoensis</i> (5-rayed)	49.11	Gradstein et al., 2012
NP13	CP11	<i>T Tribachiatus orthostylus</i>	50.50	Gradstein et al., 2012
		<i>B Reticulofenestra</i>	50.50	Gradstein et al., 2012
NP12	CP10	<i>B Discoaster lodoensis</i>	53.70	Gradstein et al., 2012
		<i>T Tribachiatus contortus</i>	54.17	Gradstein et al., 2012
NP11	CP9b	<i>B Sphenolithus radians</i>	54.17	Gradstein et al., 2012
		<i>B Tribachiatus orthostylus</i>	54.37	Gradstein et al., 2012
		<i>T Tribachiatus bramlettei</i>	54.42	Gradstein et al., 2012
		<i>B Tribachiatus contortus</i>	54.76	Gradstein et al., 2012
		<i>B Discoaster diastypus</i>	54.95	Gradstein et al., 2012
		<i>Bc Tribachiatus bramlettei</i>	55.42	Gradstein et al., 2012
		<i>T Fasciculithus</i> spp.	55.64	Gradstein et al., 2012
		<i>Bc Campylosphaera eodela</i>	55.81	Gradstein et al., 2012
		<i>B Tribachiatus bramlettei</i>	55.86	Gradstein et al., 2012
		<i>B Rhomboaster</i> spp.	55.96	Gradstein et al., 2012
NP10	CP8b	Eocene/Paleocene boundary	55.96	Gradstein et al., 2012
		<i>B Campylosphaera eodela</i>	56.66	Gradstein et al., 2012
		<i>T Ericsonia robusta</i>	56.78	Gradstein et al., 2012

Table T2 (continued).

Zone base (Martini, 1971; Sissingh, 1977)	Zone base (Okada and Bukry, 1980; Roth, 1978)	Species event	GTS2012 age (Ma)	Calibration reference
NP9	CP8a	Bc <i>Discoaster multiradiatus</i>	57.21	Gradstein et al., 2012
		B <i>Discoaster multiradiatus</i> (rare)	57.32	Gradstein et al., 2012
		T <i>Discoaster okadae</i>	57.47	Gradstein et al., 2012
		B <i>Discoaster okadae</i>	57.50	Gradstein et al., 2012
		B <i>Discoaster nobilis</i>	57.50	Gradstein et al., 2012
NP8	CP8a	B <i>Heliolithus riedelii</i>	58.70	Gradstein et al., 2012
		T <i>Heliolithus kleinpellii</i>	58.80	Gradstein et al., 2012
NP7	CN7	B <i>Discoaster mohleri</i>	58.97	Gradstein et al., 2012
NP6	CP6	B <i>Heliolithus kleinpellii</i>	59.54	Gradstein et al., 2012
		B <i>Heliolithus cantabriae</i>	59.60	Gradstein et al., 2012
		B <i>Sphenolithus anarrhopus</i>	59.68	Gradstein et al., 2012
		T <i>Fasciculithus pileatus</i>	60.73	Gradstein et al., 2012
		B <i>Chiasmolithus consuetus</i>	61.03	Gradstein et al., 2012
NP5	CP5	B <i>Fasciculithus tympaniformis</i>	61.51	Gradstein et al., 2012
		B <i>Fasciculithus</i> 2nd radiation (B <i>F. ulii</i>)	61.59	Gradstein et al., 2012
		B <i>Neochiastozygus perfectus</i>	61.76	Gradstein et al., 2012
		B <i>Sphenolithus primus</i>	61.98	Gradstein et al., 2012
		B <i>Chiasmolithus bidens/edentulus</i>	62.07	Gradstein et al., 2012
		B <i>Fasciculithus</i> 1st radiation	62.13	Gradstein et al., 2012
NP4	CP4	B <i>Ellipsolithus macellus</i>	63.25	Gradstein et al., 2012
NP3	CP2	B <i>Chiasmolithus danicus</i>	64.81	Gradstein et al., 2012
		B <i>Cruciplacolithus tenuis</i>	65.47	Gradstein et al., 2012
NP2	CP1b	B <i>Cruciplacolithus primus</i> (3.5–5 µm)	65.76	Gradstein et al., 2012
		B <i>Neobiscutum parvulum</i>	65.9	Gradstein et al., 2012
		Cretaceous/Paleogene boundary	66.04	Gradstein et al., 2012
		T <i>Micula murus</i> , Cretaceous nannofossils	66.04	Gradstein et al., 2012
NP1	CP1	B <i>Biantholithus sparsus</i> ; B <i>Calcispheres</i>	66.06	Gradstein et al., 2012

hammer. All samples were oven-dried at 50°C, and the dried samples were transferred to labeled glass vials. When a significant amount of coarse material was present, an additional 2 mm mesh sieve was used. This fraction was described separately. The 63 µm fraction was retained for additional observation for paleobathymetric indicators. Cross contamination between samples was avoided by ultrasonically cleaning sieves between samples. In addition, mudline samples from each hole were analyzed for planktonic and benthic foraminifers. Mudline samples were collected by emptying the sediment/water from the top core liner of each hole into a bucket and then washed with tap water over 63 and 150 µm mesh sieves. Rose bengal was added to identify the presence of recently living foraminifers. After several days soaking in rose bengal, the samples were treated similarly to the core catcher samples. The >150 µm size fraction was split into suitable aliquots and then examined under a Zeiss Discovery V8 microscope. Foraminifers were identified using a Zeiss microscope equipped with a Spot RTS system with the IODP Image Capture and Spot commercial software for taking photomicrographs. An SEM was used for acquiring characteristic images of specific species and to assess the state of preservation of the foraminifers.

Planktonic foraminifers

Planktonic foraminifers were identified following the taxonomy of Kennett and Srinivasan (1983), Bolli and Saunders (1985), and Saito et al. (1981). The planktonic foraminifer zonation schemes of Blow (1969, 1979) and Berggren et al. (1995), as modified by Wade et al. (2011), were used. Calibrated ages for bioevents are from Gradstein et al. (2012) and Wade et al. (2011) (Figure F8; Table T3). Eocene foraminifers (Hole U1459C) were identified following Pearson et al. (2006).

Individual planktonic foraminifers were recorded in qualitative terms based on an assessment of forms observed in a random sam-

ple of ~100 specimens from the >150 µm size fraction. Both the relative amounts of planktonic versus benthic and planktonic foraminifer contribution to the total sample were recorded. The total abundance of planktonic foraminifer species within the assemblage was defined as follows:

- A = abundant (>30% planktonic foraminifer specimens in total assemblage).
- C = common (>10%–30% planktonic foraminifer specimens in total assemblage).
- F = few (5%–10% planktonic foraminifer specimens in total assemblage).
- R = rare (1%–5% planktonic foraminifer specimens in total assemblage).
- VR = very rare (<1% planktonic foraminifer specimens in total assemblage).
- B = barren (no planktonic foraminifer specimens in total assemblage).

Preservation of planktonic foraminifer assemblages was recorded as follows:

- VG = very good (no evidence of breakage or dissolution).
- G = good (>80% of specimens unbroken with only minor evidence of diagenetic alteration).
- M = moderate (30%–80% of the specimens unbroken).
- P = poor (strongly recrystallized or dominated by fragments and broken or corroded specimens).

Benthic foraminifers

Taxonomic assignments followed Albani and Geijskes (1973), Van Marle (1991), Hottinger et al. (1993), Loeblich and Tappan (1994), Haig (1997), Langer and Hottinger (2000), Gallagher et al. (2009), and Parker (2009). The generic classification of Loeblich and

Table T3. Biostratigraphic event datums for planktonic foraminifers based on Gradstein et al. (2012), Expedition 356. * = regional age only. Bold = main events found during Expedition 356. B = base, T = top, X = change in coiling direction. (Continued on next page.) [Download table in .csv format.](#)

Species event	Age (Ma)	Zone/Subzone (base)	Reference
T <i>Globorotalia flexuosa</i>	0.07	PT1b	Berggren et al., 1995a
T <i>Globigerinoides ruber</i> (pink)*	0.12	PT1b	Thompson et al., 1979
B <i>Globigerinella calida</i>	0.22	PT1b	Chaproniere et al., 1994
B <i>Globorotalia flexuosa</i>	0.40	PT1b	Berggren et al., 1995a
B <i>Globorotalia hirsuta</i>	0.45	PT1b	Pujol and Duprat, 1983
T <i>Globorotalia (Truncorotalia) tosaensis</i>	0.61	PT1b/PT1a	Srinivasan and Sinha, 1992
B <i>Globorotalia hessi</i>	0.75	PT1a	Chaproniere et al., 1994
X <i>Pulleniatina</i> coiling change random to dextral*	0.80	PT1a	Pearson, 1995
T <i>Globoturborotalita obliquus</i>	1.30	PT1a	Chaisson and Pearson, 1997
T <i>Globoturborotalita apertura</i>	1.64	PT1a	Chaisson and Pearson, 1997
T <i>Globigerinoides fistulosus</i>	1.88	PT1a/PL6	Shackleton et al., 1990
T <i>Globigerinoides extremus</i>	1.99	PL6	Chaisson and Pearson, 1997
T <i>Globoturborotalita woodi</i>	2.30	PL6	Chaisson and Pearson, 1997
T <i>Globorotalia pertenuis</i>	2.30	PL6	Chaisson and Pearson, 1997
T <i>Globorotalia pseudomiocenica</i>*	2.39	PL6/PL5	Berggren et al., 1995a
Pliocene/Pleistocene boundary	2.59		Gradstein et al., 2012
T <i>Globoturborotalita decoraperta</i>	2.75	PL5	Chaisson and Pearson, 1997
T <i>Globorotalia (Menardella) multicamerata</i>	2.98	PL5	Chaisson and Pearson, 1997
B <i>Globigerinoides fistulosus</i>	3.33	PL5	Berggren et al., 1995a
T <i>Dentoglobigerina altispira</i>*	3.47	PL5/PL4	Chaisson and Pearson, 1997
B <i>Globorotalia pertenuis</i>	3.52	PL4	Chaisson and Pearson, 1997
T <i>Sphaeroidinellopsis seminulina</i>*	3.59	PL4/PL3	Chaisson and Pearson, 1997
T <i>Pulleniatina primalis</i>	3.66	PL3	Berggren et al., 1995a
T <i>Globorotalia plesiotumida</i>	3.77	PL3	Chaisson and Pearson, 1997
T <i>Globorotalia (Hirsutella) margaritae</i>	3.85	PL3/PL2	Chaisson and Pearson, 1997
X <i>Pulleniatina</i> coiling change sinistral to dextral	4.08	PL2	Chaisson and Pearson, 1997
T <i>Pulleniatina spectabilis</i> *	4.21	PL2	Berggren et al., 1995a
T <i>Globoturborotalita nepenthes</i>	4.37	PL2/PL1	Chaisson and Pearson, 1997
T <i>Sphaeroidinellopsis kochi</i>	4.53	PL1	Chaisson and Pearson, 1997
T <i>Globorotalia (Hirsutella) cibaoensis</i>	4.60	PL1	Berggren et al., 1995b
Miocene/Pliocene boundary	5.33		Gradstein et al., 2012
B <i>Sphaeroidinella dehisces</i> s.l.	5.53	PL1	Chaisson and Pearson, 1997
B <i>Globorotalia tumida</i>*	5.57	PL1/M14	Shackleton et al., 1995
B <i>Turborotalita humilis</i>	5.81	M14	Chaisson and Pearson, 1997
T <i>Globoquadrina dehisces</i>	5.92	M14	Chaisson and Pearson, 1997
B <i>Globorotalia (Hirsutella) margaritae</i>	6.08	M14	Chaisson and Pearson, 1997
T <i>Globorotalia linguaensis</i>*	6.14	M14/M13b	Berggren et al., 1995b
B <i>Globigerinoides conglobatus</i>	6.20	M13b	Chaisson and Pearson, 1997
X <i>N. acostaensis</i> coiling change sinistral to dextral	6.37	M13b	Berggren et al., 1995b
B <i>Pulleniatina primalis</i>	6.60	M13b	Berggren et al., 1995b
X <i>N. acostaensis</i> coiling change dextral to sinistral	6.77	M13b	Berggren et al., 1995b
B <i>Candeina nitida</i>	8.43	M13b	Berggren et al., 1995b
B <i>Neogloboquadrina humerosa</i>	8.56	M13b	Berggren et al., 1995b
B <i>Globorotalia plesiotumida</i>	8.58	M13b/M13a	Chaisson and Pearson, 1997
B <i>Globigerinoides extremus</i>	8.93	M13a	Turco et al., 2002
B <i>Globorotalia cibaoensis</i>	9.44	M13a	Chaisson and Pearson, 1997
B <i>Globorotalia juanai</i>	9.69	M13a	Chaisson and Pearson, 1997
B <i>Neogloboquadrina acostaensis</i> ([sub]tropical)*	9.83	M13a/M12	Chaisson and Pearson, 1997
T <i>Paragloborotalia mayeri</i> ([sub]tropical)*	10.46	M12/M11	Chaisson and Pearson, 1997
B <i>Neogloboquadrina acostaensis</i> (temperate)*	10.57	M11	Chaisson and Pearson, 1997
B <i>Globorotalia limbata</i>	10.64	M11	Chaisson and Pearson, 1997
T <i>Cassigerinella chipolensis</i>	10.89	M11	Turco et al., 2002
B <i>Globoturborotalita apertura</i>	11.18	M11	Chaisson and Pearson, 1997
B <i>Globoturborotalita decoraperta</i>	11.49	M11	Chaisson and Pearson, 1997
T <i>Globigerinoides subquadratus</i>	11.54	M11	Turco et al., 2002
B <i>Globoturborotalita nepenthes</i>	11.63	M11/M10	Turco et al., 2002
T <i>Globorotalia (Fohsella) fohsi</i> s.l. (including <i>lobata</i> and <i>robusta</i>)	11.79	M10/M9b	Chaisson and Pearson, 1997
B <i>Globorotalia linguaensis</i>	12.84	M9b	Turco et al., 2002
B <i>Globorotalia (Fohsella) fohsi robusta</i>	13.13	M9b/M9a	Chaisson and Pearson, 1997
B <i>Globorotalia (Fohsella) fohsi</i> s.l.	13.41	M9a/M8	Chaisson and Pearson, 1997
B <i>Globorotalia (Fohsella) "praefohsi"</i>	13.77	M8/M7	Turco et al., 2002
T <i>Globorotalia (Fohsella) peripheroronda</i>	13.80	M7	Turco et al., 2002
T <i>Clavatorella bermudezi</i>	13.82	M7	Shackleton et al., 1999
T <i>Globorotalia archeomenardii</i>	13.87	M7	Turco et al., 2002
B <i>Globorotalia (Fohsella) peripheroacuta</i>	14.24	M7/M6	Pearson and Chaisson, 1997

Table T3 (continued).

Species event	Age (Ma)	Zone/Subzone (base)	Reference
<i>B Globorotalia praemenardii</i>	14.38	M6	Pearson and Chaisson, 1997
<i>T Praeorbulina sicana</i>	14.53	M6	Shackleton et al., 1999
<i>T Globigerinatella insueta</i>	14.66	M6	Pearson and Chaisson, 1997
<i>B Orbulina suturalis</i>	15.10	M6/M5b	Shackleton et al., 1999

Tappan (1988) was used in combination with Sen Gupta (1999), and name validity was confirmed using the World Foraminifera Database (Hayward et al., 2015).

Individual benthic and planktonic foraminifers were recorded to determine assemblage composition and paleodepth estimates in qualitative terms. This was done by counting foraminifers in a random sample of ~100 specimens from the >150 µm size fraction. Both the relative amount of benthic versus planktonic and benthic foraminifer contribution to the total sample were recorded.

Paleobathymetric estimates were based on dominant species in benthic assemblages. Modern shelfal foraminiferal assemblages on Australia's continental margin are similar to Pliocene–Pleistocene assemblages and can therefore be used as modern analogs for paleodepth and paleonutrient interpretations (Li et al., 1996a, 1996b; Gallagher et al., 1999; Smith et al., 2001; Smith and Gallagher, 2003). Similarly, modern benthic foraminiferal assemblage analog data from the region may be used for this purpose, including Sunda shelf from 5°N to 10°N (Biswas, 1976), Banda Sea and Timor Trough from 5°S to 10°S (van Marle, 1988), Sahul shelf and Timor Sea from 8°S to 14°S (Loeblich and Tappan, 1994), Exmouth Gulf at 22°S (Haig, 1997; Orpin et al., 1999), Ningaloo Reef at 24°29'S (Parker, 2009), and the western Australian continental shelf from 20°S to 34°S (Li et al., 1999; Betjeman, 1969; Quilty, 1977). These distributions are supplemented with data from the Indonesian archipelago (Szarek et al., 2006), Ontong Java Plateau (Hermelin, 1989), and broader Indo-Pacific syntheses (Gallagher et al., 2009). A summary of the depth distribution of key nonlarger foraminifers from these papers is compiled in Figure F9. These analog data may be enhanced with paleodepth estimates from larger foraminiferal distribution (Renema, 2006; James et al., 1999; Hohenegger, 1995, 2005; Langer and Hottinger, 2000). Paleobathymetric estimates were classified as inner shelf (0–50 m water depth), middle shelf (50–100 m), outer shelf (100–200 m), and upper bathyal (200 to >400 m).

The percentage of planktonic foraminifers in total assemblage (%P) data can also be used to estimate paleodepths (van der Zwaan et al., 1990) and has been used to obtain paleobathymetric estimates prior to backstripping and generation of subsidence curves (van Hinsbergen et al., 2005; Gallagher et al., 2013). The error on paleodepth estimates increases with increasing %P. Van der Zwaan et al. (1990) determined the 90% confidence limit on a single %P value of 50% planktonic specimens (430 m paleodepth) was 100–150 m, and the error on a 99% value (1200 m paleodepth) was approximately 400 m.

The relative abundance of foraminifer species in analyzed samples (>150 µm) were estimated as follows:

- D = dominant (>30% benthic foraminifer specimens in total assemblage).
- A = abundant (>10%–30% benthic foraminifer specimens in total assemblage).
- F = few (>5%–10% benthic foraminifer specimens in total assemblage).
- R = rare (1%–5% benthic foraminifer specimens in total assemblage).
- P = present (<1% benthic foraminifer specimens in total assemblage).

Paleobathymetric zones were estimated via isolating the most dominant/abundant species in each sample and associating them with established zones (Li et al., 1996a, 1996b; Smith et al., 2001; Smith and Gallagher, 2003) (Figure F9). These zones include the following:

- P = photic zone.
- IS = inner shelf.
- MS = middle shelf.
- OS = outer shelf.
- UB = upper bathyal.

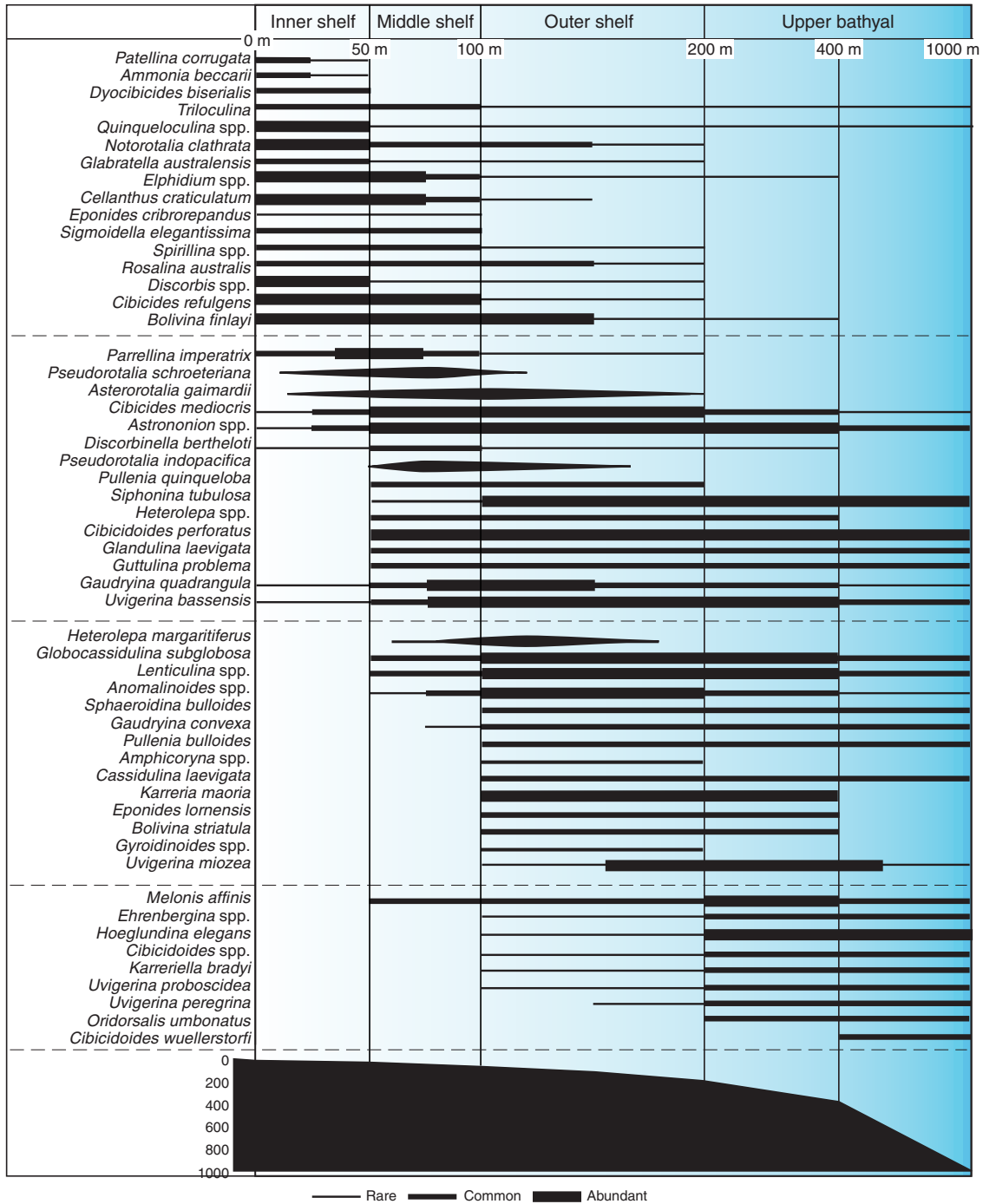
The degree of preservation of the benthic foraminifers (>150 µm), describing the degree of test breakage and surficial damage, was estimated as follows:

- VG = very good (no evidence of breakage or dissolution).
- G = good (>80% of specimens unbroken with only minor evidence of diagenetic alteration).
- M = moderate (30%–80% of the specimens unbroken).
- P = poor (strongly recrystallized or dominated by fragments and broken or corroded specimens).

Additional microfossil groups

In addition to the detailed analyses of nannofossils and foraminifers, the samples were scanned for the presence of other microfossil groups. These groups include pteropods, ostracods, bryozoans, mollusks, and sponge spicules. Notable and/or dominant occurrences of specific groups were also documented.

Figure F9. Summary of common modern shelf to bathyal foraminifer depth distributions off the western and southern coasts of Australia.



Geochemistry

The shipboard geochemistry program for Expedition 356 included measurements for

- Headspace gas content;
- IW composition, including pH, alkalinity, salinity, and major and minor elements; and

- Bulk sediment geochemistry, including total inorganic carbon (TIC), total organic carbon (TOC), and total nitrogen (TN).

These analyses were carried out to satisfy routine shipboard safety, characterize IW and sediment geochemistry for shipboard interpretation, and provide a basis for sampling for shore-based research. The geochemistry methods used during Expedition 356 are generally similar to those used during other recent IODP expeditions.

Interstitial water geochemistry

Sample collection

Routine IW samples were obtained by squeezing whole-round sections cut from cores. Standard whole-round samples were 5 cm long, but as water content decreased downhole, the size of the whole-round samples was increased to up to 15 cm to enable extraction of the ~15 mL of water needed for shipboard and shore-based analyses. Whole-round samples were cut and capped as quickly as possible after the core arrived on deck and immediately moved to the chemistry laboratory for squeezing. Whole-round samples were collected at a frequency of 1 sample per core for Hole A or the first hole at a site cored to a significant depth, which in some cases (e.g., Site U1463) was Hole B. Whole-round samples were also collected at a frequency of 1 sample every third core for subsequent holes, starting at the depth below that covered in previous holes. The exterior of the whole-round sample was carefully cleaned with a spatula to remove potential contamination by drilling fluid. For XCB cores, the intruded drilling mud between biscuits was also removed to eliminate contamination from drilling fluid. The cleaned sediment was placed into a 9 cm diameter titanium squeezer that was then placed in a Carver hydraulic press (Manheim and Sayles, 1974) and squeezed at pressures no higher than 25,000 lb (~17 MPa) to prevent the release of interlayer water from clay minerals. The squeezed IW was collected into a 60 mL deionized water-washed (18 M Ω /cm) high-density polyethylene syringe attached to the squeezing assembly and subsequently filtered through a 0.45 μ m polyethersulfone membrane filter into various sample containers.

Sample allocation was determined based on the pore fluid volume obtained and analytical priorities of the expedition. Aliquots for alkalinity, pH, salinity, ammonia, and phosphate analyses were placed in 8 mL glass vials. Aliquots for major and minor element concentration analyses by inductively coupled plasma-atomic emission spectroscopy (ICP-AES) were acidified by adding ~10 μ L of trace metal-grade concentrated HNO₃ and placed in 5 mL cryovials. Remaining IW was put in 40 mL glass vials and kept for post-cruise sample analyses. Samples were stored at 4°C after collection.

After IW extraction was complete, sediment squeeze cakes were divided and sealed in plastic bags for shipboard and shore-based analyses and stored at 4°C.

Interstitial water analyses

IW samples were analyzed on board the ship following the protocols in Gieskes et al. (1991), Murray et al. (2000), and the IODP user manuals for shipboard instrumentation.

Salinity, alkalinity, and pH were measured immediately after squeezing, following the procedures in Gieskes et al. (1991). Salinity was measured using a Fisher temperature-compensated handheld refractometer, pH was measured with a combined glass electrode, and alkalinity was determined by Gran titration with an autotitrator (Metrohm 794 basic Titrino) using 0.1 M HCl at 25°C. International Association for the Physical Sciences of the Oceans (IAPSO) standard seawater was used as a standard to check for instrument drift every 20 samples. Alkalinity titrations had a precision better than 5% based on repeated analysis of IAPSO standard seawater.

Dissolved major and minor elements were determined by Lee-man ICP-AES. For major cation (Na⁺, K⁺, Ca²⁺, and Mg²⁺) analyses, dilutions of IAPSO standard seawater were used as calibration standards. Standards and acidified samples were diluted 1:100 (v/v) with a 2% HNO₃ (by volume) solution (matrix) with 10 ppm yttrium (Y)

as an internal standard. Calibration for minor elements (Mn²⁺, Fe²⁺, B, Si, Sr²⁺, Ba²⁺, and Li⁺) was done with dilutions of a multielement synthetic standard solution (composed of single-element standards). Acidified samples measured for minor elements on the ICP-AES were diluted 1:20 (v/v) with the same matrix used for the major element analysis. Drift correction was made for both major and minor elements using the factor from a drift monitor solution (100% IAPSO for major elements and 100% stock solution for minor elements) that was analyzed every eight samples. The ICP-AES auto-sampler and analysis chamber were rinsed with a 3% (by volume) HNO₃ solution between samples. Major cations (Mg²⁺, Ca²⁺, K⁺, and Na⁺) were also determined by ion chromatography (IC) at 1:100 dilutions.

For PO₄³⁻ and NH₄⁺, colorimetric methods were applied. Ammonium adsorption of indophenol blue at 640 nm wavelength was measured with a spectrophotometer (Agilent Technologies UV-Vis), with an aliquot of 100 μ L IW used as minimum volume. Blank and 50, 100, 200, 400, 600, 800, 1000, 1500, 2000, and 3000 μ M NH₄⁺ standard solutions were prepared in the same manner as the sample solutions and analyzed within 5 h. Phosphate (an aliquot of 600 μ L IW) was analyzed using adsorption of molybdate blue at 885 nm wavelength with the spectrophotometer used for NH₄⁺. Blank and 5, 10, 15, 20, 40, 60, 80, 100, 200, and 300 μ M PO₄³⁻ standard solutions were prepared in the same manner as that of the sample solutions. Relative standard deviations (RSDs) of repeated analyses of both components are within 2%–5%.

Organic geochemistry

Headspace gas analysis

A 5 cm³ sediment sample from each core was collected immediately after retrieval on deck and placed in a 20 cm³ glass vial, which was sealed with a septum and a crimped metal cap. When consolidated or lithified samples were encountered, chips of material were placed in the vial and sealed. If an IW sample was obtained, the headspace sample was taken from the top of the section immediately next to it whenever possible. The sample was then placed in an oven at 70°C for 30 min. A 5 cm³ volume of gas was extracted through the septum with a gas-tight glass syringe and injected into a gas chromatograph (GC).

An Agilent/HP 6890 series II GC (GC3) equipped with a flame ionization detector (FID) was used to measure the concentrations of methane (C₁), ethane (C₂), ethylene (C₂), propane (C₃), and propylene (C₃). A 2.4 m \times 2.0 mm (inner diameter) Restek stainless steel column packed with 80/100 mesh HayeSep "R" was used. A 1/16 inch Valco union with a 7 μ m screen connected to a Valco-to-Luer lock syringe adaptor was used as the injector, which connected to a 10 port Valco valve that was switched pneumatically by a digital valve interface. The injector temperature was set at 120°C. The GC3 oven temperature was programmed to start at 80°C, hold for 8.25 min, and then ramped at 40°C/min to a final temperature of 150°C, which was held for 5 min. Helium was used as the carrier gas. The FID temperature was set at 250°C.

Bulk sediment geochemistry

Sediment samples were collected from the IW squeeze cakes for inorganic and organic carbon analyses. In a few cases, residues from MAD samples (see [Physical properties](#)) were analyzed when the sediment type did not allow for IW sampling. Samples were freeze-dried for ~24 h, crushed using an agate pestle and mortar, and then analyzed for total carbon (TC), TIC, and TN.

TC and TN of the sediment samples were determined with a ThermoElectron Corporation FlashEA 1112 CHNS elemental analyzer (EA) equipped with a ThermoElectron packed column CHNS/NCS GC and a thermal conductivity detector (TCD). Approximately 10–15 mg of sediment was weighed into a tin cup and then combusted at 950°C in a stream of oxygen. The reaction gases were passed through a reduction chamber to reduce CO₃ to CO₂ and nitrogen oxides to nitrogen and were then separated by the Thermo CHNS/NCS multiseparation column before detection by TCD. All measurements were calibrated to a standard (Soil Reference Material NC [PN 33840025]), which was run every 10 samples. Peak areas from the TCD were calculated to determine TC and TN of the samples.

TIC was determined using a Coulometrics 5015 CO₂ coulometer. Approximately 10–12 mg of sediment was weighed into a glass vial and acidified with 2 M HCl. The liberated CO₂ was titrated, and the corresponding change in light transmittance in the coulometric cell was monitored using a photodetection cell. The weight percent of calcium carbonate was calculated from the inorganic carbon content using the following equation:

$$\text{CaCO}_3 \text{ (wt\%)} = \text{TIC} \times 8.33 \text{ (wt\%)}$$

No correction was made for the presence of other carbonate minerals. A standard of pure (100 wt%) CaCO₃ was analyzed every 10 samples and used to confirm accuracy. TOC was calculated as the difference between TIC (measured by coulometry) and TC (measured by EA):

$$\text{TOC} = \text{TC} - \text{TIC}$$

Paleomagnetism

Paleomagnetic data acquisition focused on natural remanent magnetization (NRM) measurements and alternating field (AF) demagnetization of archive-half core sections and discrete cube samples. Discrete cube samples were taken from selected working halves and subjected to more comprehensive NRM measurements than archive-half sections. Bulk susceptibility and isothermal remanent magnetization (IRM) were also measured, along with backfield IRM on discrete samples when time allowed. Rock magnetism data from discrete sample measurements were used to modify AF demagnetization steps of the archive-half sections if necessary and to augment magnetostratigraphic interpretations.

Magnetic measurements

Remanent magnetization was measured using a 2G superconducting rock magnetometer (SRM) (2G Enterprises Model 760R) equipped with direct-current superconducting quantum interference devices (DC-SQUIDS) and an in-line automated AF demagnetizer. Sediment cores generally carry components of secondary remanence (overprints), including natural viscous remanence and a steep downward-pointing component attributed to the drill string. To separate the overprints from the characteristic remanent magnetization (ChRM), stepwise demagnetization experiments were performed, as described below.

Archive-half sections

Measurements of archive halves were conducted using the software SRM (version 1.0), set up for section measurements, with a nominal sample-area parameter of 15.59 cm². The measurement in-

terval and speed were 10 cm and 10 cm/s, respectively. The response functions of the pick-up coils of the DC-SQUID sensors have a full width of 7–8 cm at half height (Parker and Gee, 2002). Therefore, data collected within ~4 cm of section ends (or voids) are significantly affected by edge effects. Consequently, all data points within 4.5 cm of voids (as documented in the curatorial record) or 8 cm of section ends were either filtered out of the data before analysis or treated with caution. It should be noted that edge effects may also occur in a contiguous core piece if substantial heterogeneity (in intensity or direction) is present in the piece. It is more difficult to filter out such artifacts, but calculating the average ChRM directions for each core piece could provide a means of identifying these problems (Expedition 330 Scientists, 2012).

For all archive-half core sections, we performed NRM measurements with stepwise AF demagnetization by using the in-line AF demagnetizer of the SRM. The in-line AF demagnetizer applies a field to the *x*-, *y*-, and *z*-axes of the SRM in this fixed order. For most of the core sections, we performed demagnetization steps from NRM (0 mT) to 20 or 30 mT. The AF demagnetization results were plotted individually as orthogonal diagrams (Zijderveld, 1967) and collectively as downhole variations with depth. When time allowed, the archive-half core section data were evaluated by principal component analysis (PCA) (Kirschvink, 1980). Otherwise, we inspected the plots visually to judge whether the remanence after demagnetization at the highest AF step reflects the ChRM and geomagnetic polarity sequence.

Technical difficulties with archive-half measurements

The *y*-axis SQUID sensor on the SRM experienced frequent flux jumps while measuring archive-half sections at Sites U1459 and U1460, with a significant increase in frequency during measurements at the top of Hole U1461C. Flux jumps affected only the *y*-axis and sometimes occurred during each step of a section measurement (equivalent to at least one flux jump per 10 min). Remanent magnetizations calculated from data affected by flux jumps produced invariable values for inclination (near 0°), declination (near 270°), and magnetic intensity (that increased linearly downcore in each section half). Manual and magnetic cleaning of the tray and track were carried out in an attempt to remedy the problem. Fine-tuning of the *y*-axis SQUID meter seemed to stabilize the SRM, and flux jumps became less frequent.

Flux jumps on the *y*-axis were described during Integrated Ocean Drilling Program Expedition 342 (Norris et al., 2014). They refer to this occurrence as the “antennae” effect and attribute it to stray magnetic flux being channeled into the magnetometer-sensing region. Similar to Expedition 356 experience, Expedition 342 paleomagnetists also measured sections containing wet carbonate and saw an increase in flux jumps during rough seas. They also found that an unshielded cable near the degausser contributed to the antennae effect, but no unshielded cables were identified during Expedition 356.

After noticing the jumps in flux, the *y*-axis SQUID meter was regularly checked and fine-tuned, especially during rough seas. Flux jump occurrences were much less frequent at Sites U1462, U1463, and U1464 but still occurred occasionally. Section data that were affected during the highest demagnetization step, which are used for magnetostratigraphic interpretation, were corrected by restarting the section measurement as another NRM step. The second NRM step is then used instead of the affected demagnetization step for data plotting and interpretation.

Discrete samples

Oriented discrete samples representative of the lithology were collected from working-half sections. For soft sediments, discrete samples were taken in plastic “Japanese” Natsuhara-Giken sampling cubes (7 cm³ sample volume). Cubes were manually pushed into the working half of the core and an “up” arrow pointing upsection in the core drawn on the cube. For indurated intervals of the core, oriented cubes (~6–7 cm³) were cut with a table saw and trimmed to fit in the plastic JR-6A semiautomatic holder.

A suite of discrete samples were selected and subjected to stepwise AF demagnetization in order to (1) characterize typical intervals, (2) better resolve magnetostratigraphy, and (3) determine whether a ChRM could be resolved, and if so, what level of demagnetization was required to resolve the ChRM. At the beginning of Expedition 356, a few instances of slow core flow allowed us to use the SRM for pass-through discrete sample measurements. For these, we used the in-line AF demagnetizer, controlled by the SRM (version 1.0) software, to demagnetize the samples in 10 mT steps up to 80 mT. Specimens were placed on a discrete sample tray in the “top-away” orientation (arrow on top of the cube pointing away from the body of the SRM). Adjacent samples were separated by 20 cm to avoid convolution effect of the SRM sensor responses. Software bugs, core flow, and other difficulties lead us to use the spinner magnetometer (AGICO Model JR-6A) for the rest of Expedition 356. We used the JR-6A spinner magnetometer and an AF demagnetizer, Model D-2000 (ASC Scientific), for remanence and demagnetization measurements. Measurements were performed in steps of 10–20 mT up to peak field of 80–120 mT (majority of samples) and 160–180 mT (high-coercivity samples).

We analyzed the stepwise demagnetization data of the discrete samples by PCA to define the ChRM. Section-half and discrete data collected on the pass-through SRM were uploaded automatically to the LIMS database. Discrete data collected from the SRM and JR-6A spinner magnetometer were analyzed in Remasoft (version 3.0; AGICO, Inc.) and Puffin Plot (version 1.03; Lurcock and Wilson, 2012), depending on the output file of the instrument.

Low-field MS of both whole rounds (see [Physical properties](#)) and section halves (see [Lithostratigraphy and sedimentology](#) and [Physical properties](#)) was routinely measured to estimate the concentration of ferromagnetic (*sensu stricto*) minerals. Volume-normalized, calibrated bulk susceptibility (χ) measurements were made on an AGICO KLY 4 Kappabridge instrument operating at low alternating induction magnetic field values (~10 kHz at a field value of 0.7 mT). Measurements were carried out with the SUFAR software (AGICO, Inc.).

IRM inquisition measurements were used to obtain information on the magnetic mineralogy content, as well as for quantification of the components of magnetic coercivity. Selected discrete specimens that underwent AF demagnetization over the 100 mT step were subsequently subjected to progressive stepwise magnetic fields from 0 to 1200 mT using an Impulse magnetizer (ASC Model IM10) with the orientation arrows on the top of the cube pointing out of the body of the instrument. These measurements provide information such as the saturation IRM (SIRM) and coercivity of remanence. Induced magnetization was measured with the JR-6A spinner magnetometer. A backfield IRM was then imparted in the same manner, except the orientation arrows on the top of the cubes pointed into the body of the instrument. In some special cases, such as for discrete samples from Sites U1459 and U1460, IRM acquisition curves were modeled using cumulative log analysis as dis-

cussed in Kruiver et al. (2001). Furthermore, some samples that were used for IRM analysis underwent stepwise demagnetization of the SIRM using AFs up to 120 mT on the D-2000 AF demagnetizer, allowing estimation of the median destructive field of the samples.

Coordinates

All magnetic data are reported relative to IODP orientation conventions: +*x* is into the face of the working half, +*y* points toward the left side of the face of the working half, and +*z* points down-section. The relationship between the SRM coordinates (*X*, *Y*, and *Z*) and the data coordinates (*x*, *y*, and *z*) is $x = X$, $y = -Y$, and $z = Z$ for archive halves and $x = -X$, $y = Y$, and $z = Z$ for working halves. The coordinate systems for the JR-6A spinner magnetometer and Natsuhara-Giken sampling cubes are indicated in Figure F10. In order to view discrete sample data in geographic coordinates that agree with SRM data, they were assigned an azimuth of 0 and dip of 90 in the JR-6A spinner software, Rema6W.

Core orientation

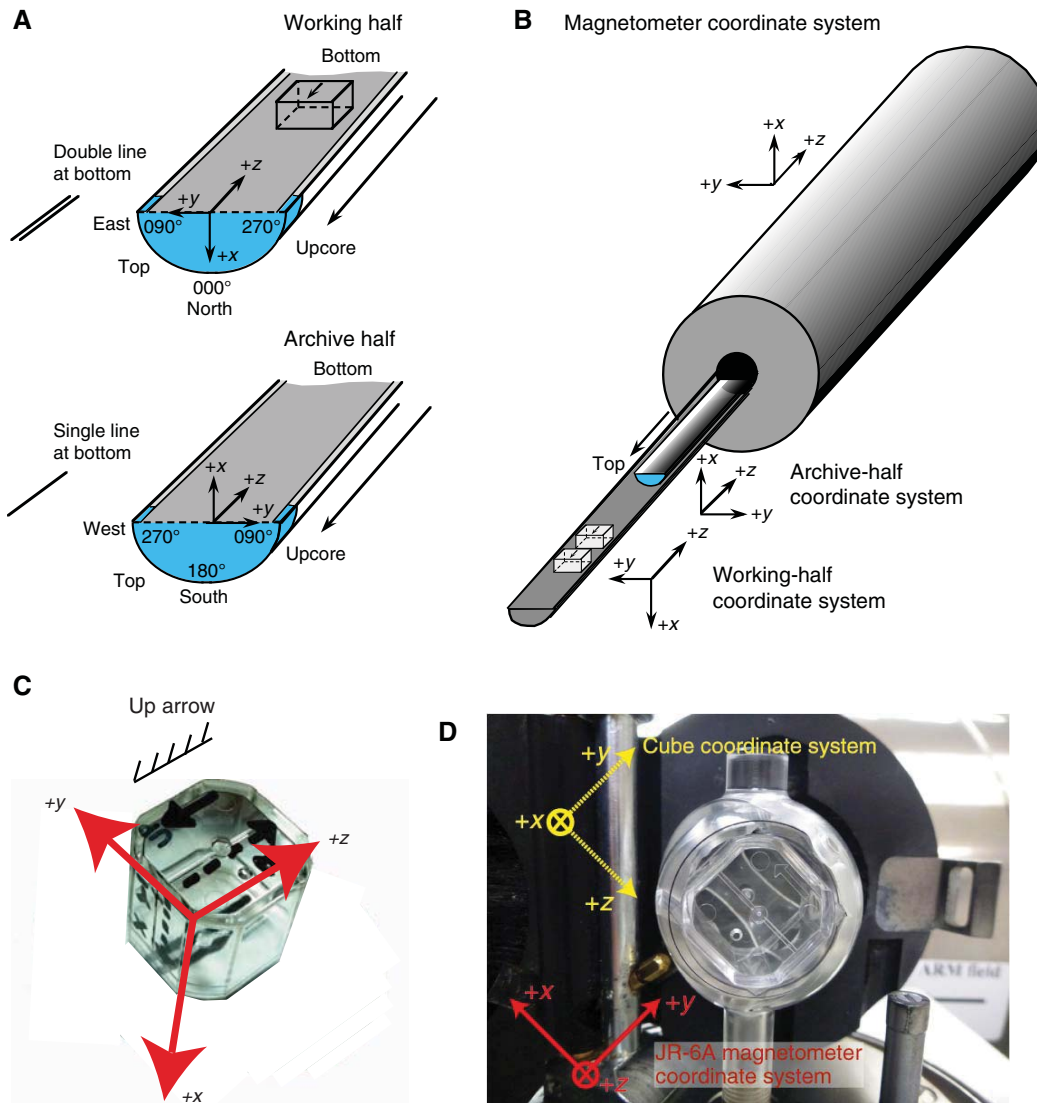
During APC, HLAPC, and RCB coring, nonmagnetic (Monel) core barrels and nonmagnetic drill collars were used, allowing much better quality of magnetic data from these intervals than those related to the XCB system. Only APC cores were oriented; APC core orientation was achieved with the Icefield MI-5 orientation tool, mounted on the core barrel for selected holes (e.g., Holes U1461C and U1463C). The tool consists of three mutually perpendicular fluxgate magnetic sensors and two perpendicular gravity sensors. The information from both sets of sensors allows the azimuth and dip of the hole to be measured, as well as the azimuth of the APC core orientation. The orientation information contributed to paleomagnetic polarity determinations and magnetostratigraphic interpretations.

Magnetostratigraphy

Magnetostratigraphy for each site was constructed by correlating observed polarity sequences with the geomagnetic polarity timescale (GPTS) and compared with biostratigraphic datums (see [Biostratigraphy and micropaleontology](#)). Polarity sequences were established using archive-half and discrete sample data together when possible, but some sites required dependence on one or the other due to technical difficulties and/or the nature of the sediments and limits of shipboard analysis. We adopted the GPTS of Gradstein et al. (2012), in which boundary ages for Chrons C1n–C13n and C24n.1n–C34n are orbitally tuned, whereas those for Chrons C13r–C23r are fit with splines. The mean state of the geomagnetic field corresponds to a geocentric axial dipole (GAD). The field inclination (*I*) can be evaluated by using the relationship $\tan(I) = 2\tan(\lambda)$, where λ is the latitude for a given position. All Expedition 356 sites are located in the Southern Hemisphere where the time-averaged field currently has a negative inclination that is expected to be about -35° . Therefore, negative (positive) inclinations at the magnetostratigraphic evaluations indicated normal (reversed) polarities.

Whenever possible, we offer an interpretation of the magnetic polarity following the naming convention of correlative anomaly numbers prefaced by the letter C (Tauxe et al., 1984). For normal polarity subchrons, suffixes (n1, n2, etc.) that increase with age were affixed to the names. For the younger part of the timescale (Pliocene–Pleistocene), we use traditional names to refer to the various chron and subchrons (e.g., Brunhes, Jaramillo, Olduvai, etc.). In

Figure F10. A. Paleomagnetic sample coordinate systems. B. SRM coordinate system on the *JOIDES Resolution*. C. Natsuhara-Giken sampling cubes (7 cm³ volume) shown with sample coordinate system used during Expedition 356. Hatched arrow is parallel to the “up” arrow on the sample cube and points in the $-z$ axis sample direction. (after Harris et al., 2013). D. Positioning of discrete samples in the automatic holder of the JR-6A spinner magnetometer.



general, polarity reversals occurring at core section ends have been treated with extreme caution.

Physical properties

High-resolution physical properties measurements were made during Expedition 356 with several primary objectives. The first was to measure the lithology-dependent density and porosity of the sections so that the tectonic subsidence of each of the sites could be interpreted in conjunction with the age model and paleobathymetry. Secondly, the physical properties aided the lithostratigraphic characterization and were a valuable tie between core observations, downhole measurements, and seismic profiles. In particular, physical properties data played a major role in hole-to-hole and site-to-site stratigraphic correlation, detection of discontinuities and heterogeneities, identification of differences in sediment composition and texture, and identification of major seismic reflectors. Finally, we also measured the thermal properties of the recovered material and used them in conjunction with the downhole temperature mea-

surements to infer heat flow. A variety of techniques and methods were used to characterize Expedition 356 cores on whole-round, split-core, and discrete samples. Core sections are generally 1.5 m in length, so a typical coring length (stroke) of 9.5 m yields six sections plus a shorter seventh section. Procedures for measuring soft sediment or lithified sediment cores differ slightly.

Sedimentary cores

Recovered whole-round sections were first allowed to equilibrate to ambient room temperature ($\sim 20^{\circ}\text{C}$) and pressure for ~ 4 h. After thermally equilibrating, core sections were run through the WRMSL for measurement of density by gamma ray attenuation (GRA), MS, and, where contact between sediment and core liner was sufficiently good, compressional wave velocity on the P -wave logger (PWL). Cores recovered with the XCB or RCB systems are slightly smaller in diameter than those cored with the APC system. As a result, sections cored with the XCB or RCB typically have gaps between the liner and the core. In these cases, P -wave velocity measurements with the WRMSL were often outside the accepted veloc-

ity range (1000–4500 m/s) and therefore not retained. Sections were subsequently measured with the NGRL.

In one hole at each site, thermal conductivity was measured on approximately one whole-round per core and then repeat measurements were taken in subsequent holes, as needed. Measurements were conducted with a needle probe inserted into the section through a small hole drilled through the plastic core liner close to the middle of the section. In lithified sediments, a contact probe method in a half-space configuration on split cores was used for thermal conductivity measurements.

After completion of measurements on whole-round sections, the cores were split longitudinally, with one half designated as archive and one as working for sampling and analysis (see **Core handling and analysis**). The archive half of the core was passed through the SHMSL for measurement of MSP, colorimetry, and color reflectance (see **Lithostratigraphy and sedimentology**).

Compressional *P*-wave velocity measurements on split cores were typically made on the working halves that had been sampled for MAD, employing the *P*-wave caliper (*x*-axis direction). Shear strength (Torvane) and normal strength (penetrometer) were measured on the same half cores.

Discrete samples were collected from the working halves. Two samples were generally taken in each full-length core and one in each half-length core in the first hole at each site. Depending on lithologic variability, additional samples were taken in conjunction with smear slides or thin sections. These samples were then used to measure wet bulk density, dry bulk density, water content, porosity, and grain density with MAD procedures. Where possible, samples were taken at the same locations as smear slides (see **Lithostratigraphy and sedimentology**) so that a quantitative assessment of grain size and lithology corresponds directly to MAD results.

A full discussion of all methodologies and calculations used aboard the *JOIDES Resolution* in the physical properties laboratory is available in Blum (1997). Details and procedures for each physical properties measurement are described below.

Whole-Round Multisensor Logger measurements

GRA-derived bulk density, *P*-wave velocity, and magnetic susceptibility were measured nondestructively with the WRMSL. To optimize the measurement process, sampling intervals and measurement integration times were the same for all sensors. Sampling intervals were set at 5 cm with an integration time of 3 s for each measurement. These sampling intervals are common denominators of the distances between the sensors installed on the WRMSL (30–50 cm), which allows sequential and simultaneous measurements. After measuring a core, quality control/quality assurance (QC/QA) was monitored by passing a single core liner filled with deionized water through the WRMSL.

We also fast-tracked the whole rounds through the STMSL with 10 cm spacing using the GRA and magnetic susceptibility before the cores had thermally equilibrated. This allowed us to provide preliminary information on the cores to be used for stratigraphic correlation of the overlapping holes at a given site (see **Stratigraphic correlation**).

Gamma ray attenuation bulk density

Bulk density can be used to estimate the pore volume in sediment and evaluate the consolidation state of sediment. GRA density is an estimate of bulk density based on the attenuation of a gamma ray beam. The beam is produced by a ¹³⁷Cs gamma ray source at a radiation level of 370 MBq within a lead shield with a 5 mm collimator, which is directed through the whole-round core. The gamma

ray detector on the opposite side of the core from the source includes a scintillator and an integral photomultiplier tube to record the gamma radiation that passes through the core. The attenuation of gamma rays occurs primarily by Compton scattering, in which gamma rays are scattered by electrons in the formation; the degree of scattering is related to the material bulk density. Therefore, for a known thickness of sample, the density (ρ) is proportional to the intensity of the attenuated gamma rays and can be expressed as

$$\rho = \ln(I/I_0)/(\mu d),$$

where

I = the measured intensity of gamma rays passing through the sample,

I_0 = gamma ray source intensity,

μ = Compton attenuation coefficient, and

d = sample diameter.

μ and I_0 are treated as constants, such that ρ can be calculated from I .

In general, WRMSL measurements are most accurate when taken on a completely filled core liner with minimal drilling disturbance; otherwise, measurements tend to underestimate true values. By default, the instrument reports measurements using the internal diameter of the core liner (66 mm) as the assumed sample diameter. This assumption is suitable for most sediment cores obtained by the APC; however, for sediment and/or hard rock cored by the XCB or RCB, core diameter is usually about 58 mm or less. The spatial resolution of the GRA densitometer is less than ± 1 cm. The gamma ray detector is calibrated with sealed calibration cores (one standard core liner filled with distilled water and aluminum cylinders of various diameters). To establish the calibration curves, gamma ray counts were taken through each aluminum cylinder for 60 s. Each aluminum cylinder has a density of 2.7 g/cm³, and d is 1, 2, 3, 4, 5, or 6 cm. The relationship between I and μd is

$$\ln(I) = A(\mu d)^2 + B(\mu d) + C,$$

where A , B , and C are coefficients determined from the calibration.

Recalibration was performed as needed when the deionized water QC/QA standard deviated significantly (more than a few percent) from 1 g/cm³.

Magnetic susceptibility

Magnetic susceptibility (χ) is a dimensionless measure of the degree to which a material can be magnetized by an external magnetic field:

$$\chi = M/H,$$

where M is the magnetization induced in the material by an external field of strength H . Magnetic susceptibility is primarily sensitive to the concentration of ferrimagnetic minerals (e.g., magnetite, pyrite, and a few other iron oxides). It is also sensitive to magnetic mineralogy and can be related to the origin of the materials in the core and their subsequent diagenesis.

The measurements were made using a Bartington MS2C loop sensor with a 9 cm diameter. An oscillator circuit in the sensor, which operates at a frequency of 0.565 kHz and an AF of ~ 140 A/m, produces a low-intensity nonsaturating alternating magnetic field. Sediment core sections going through the influence of this field cause a change in oscillator frequency. Frequency information re-

turned in pulse form to the susceptometer is converted into magnetic susceptibility. The loop sensor has a spatial resolution of 23–27 mm and is accurate to within 2%.

P-wave velocity

P-wave sonic velocity data can be used to assist in the correlation between the core and seismic sections, correlate between downhole logging and core data, and evaluate porosity and cementation. *P*-wave (compressional) velocity (V_p) is defined by the time required for a compressional wave to travel a specific distance:

$$V_p = d/t_{\text{core}}$$

where d is the path length of the wave across the core and t_{core} is the travelt ime through the core.

The PWL measures the travelt ime of 500 kHz ultrasonic waves horizontally across the core at 5 cm intervals while it remains in the core liner. Waves are transmitted to the core by transducer contacts connected to linear actuators. Pressure is applied to the actuators to ensure coupling between the transducers and the core liner, and the space between the core liner and transducers was kept wet to ensure good coupling. *P*-wave velocity transducers measure total travelt ime of the compressional wave between transducers. The wave travels horizontally across the whole core and core liner. The total observed travelt ime t_{core} is composed of

t_{delay} = time delay related to transducer faces and electronic circuitry,

t_{pulse} = delay related to the peak detection procedure,

t_{liner} = transit time through the core liner, and

t_{core} = travelt ime through the sediment.

The system is calibrated using a core liner filled with distilled water, which provides control for t_{delay} , t_{pulse} , and t_{liner} . From these calibrations, V_p can be calculated for the whole-round specimens in core liners as

$$V_p = (d_{\text{cl}} - 2d_{\text{liner}})/(t_o - t_{\text{pulse}} - t_{\text{delay}} - 2t_{\text{liner}}),$$

where

d_{cl} = measured diameter of core and liner,

d_{liner} = liner wall thickness, and

t_o = measured total travelt ime.

The above equation assumes that the core completely fills the core liner. Measurements outside the accepted range of 1000–4500 m/s were discarded.

Natural Gamma Radiation Logger measurements

Gamma radiation is emitted from the decay of 238-uranium (^{238}U), 232-thorium (^{232}Th), and 40-potassium (^{40}K) within the core sample. The NGRL measures this natural emission on whole-round cores using a system designed and built at Texas A&M University (USA) (Vasiliev et al., 2011; Dunlea et al., 2013). When ^{238}U , ^{232}Th , and ^{40}K radioisotopes decay, they and their daughter products emit gamma radiation at specific energy levels unique to each isotope. Natural gamma radiation (NGR) spectroscopy measures a wide energy spectrum that can be used to estimate the abundance of each isotope based on the strength of the signal at characteristic energies (Blum, 1997; Gilmore, 2008). Spectral data were collected and can be used for postcruise processing for U, Th, and K abundance but

were not processed on board. Total counts were used on board, with high counts usually identifying fine-grained deposits containing K-rich clay minerals and their absorbed U and Th isotopes. NGR data thus revealed stratigraphic details that aid in core-to-core correlations. The main NGRL detector unit consists of 8 sodium iodide (NaI) detectors arranged along the core measurement axis at 20 cm intervals surrounding the lower half of the section. The detector array has passive (layers of lead) and active (plastic scintillators) shielding to reduce the background environmental and cosmic radiation. The overlying plastic scintillators detect incoming high-energy gamma and muon cosmic radiation and cancel this signal from the total counted by the NaI detectors.

The quality of the energy spectrum measured in a core depends on the concentration of radionuclides in the sample but also on the counting time, with higher times yielding better spectra. Therefore, a measurement run consisted of counting on each core section for 300 s at Position 1. After 300 s, the section was offset by 10 cm (Position 2) and measured again for 300 s. This yielded a total of 16 measurements (10 cm apart) per 150 cm section. These settings yielded statistically significant energy spectra. In some cores, the spatial resolution of NGR measurements was decreased to 20 cm by counting only at Position 1, thus speeding up core flow.

Thermal conductivity measurements

After NGR measurements were completed, thermal conductivity was measured with the TK04 (Tekla Bolin) system using a needle probe method in full-space configuration for whole-round sediment cores (Von Herzen and Maxwell, 1959) or a contact probe method in half-space configuration on split cores for lithified sediments. The probes contain a heater wire and calibrated thermistor.

For soft sediment, the needle probe was inserted into a 2 mm diameter hole drilled through the liner along one of the lines that later guided core splitting. To avoid interference from airflow in the laboratory, the core was placed into an enclosed box outfitted with foam insulation. For lithified sediment cores, the section half was put in the enclosed box, and the contact probe was put on the cut face of the sample. The contact probe was embedded in the surface of an epoxy block with a low thermal conductivity (Vacquier, 1985).

The calibrated heat source of the probe was turned on and the increase in temperature was recorded over 80 s for measurements with the needle probe and 60 s for measurements with the contact probe. A heating power of 1 W/m was typically used in soft sediment and 0.5–1.5 W/m for lithified sediments. The solution to the heat conduction equation with a line source of heat was then fit to the temperature measurements to obtain the thermal conductivity. Because the probe is much more conductive than sediment, the probe is assumed to be a perfect conductor. Under this assumption, the temperature of the superconductive probe has a linear relationship with the natural logarithm of the time after the initiation of the heat:

$$T(t) = (q/4\pi k) \times \ln(t) + C,$$

where

T = temperature (K),

q = heat input per unit length per unit time (J/m/s),

k = thermal conductivity (W/[m·K]),

t = time after the initiation of the heat (s), and

C = instrumental constant.

Three automatic measuring cycles were used to calculate average conductivity. A self-test, which included a drift study, was conducted at the beginning of each measurement cycle. Once the probe temperature stabilized, the heater circuit was closed and the temperature rise in the probe was recorded. Thermal conductivity was calculated from the rate of temperature rise while the heater current was flowing. Temperatures measured during the first 60 or 80 s of the heating cycle were fit to an approximate solution of a constantly heated line source (for details, see Kristiansen [1982] and Blum [1997]). Measurement errors were 5%–10%. Thermal conductivity measurements were routinely taken in one section per core throughout the first hole. Some cores yielded no results for thermal conductivity because cracks in the sediment caused bad coupling of the needle probe to the sediment.

Section Half Multisensor Logger measurements

We measured color reflectance and magnetic susceptibility on archive halves using the SHMSL. The archive half of the split core was placed on the core track, above which an electronic platform moves along a track, recording the height of the split-core surface with a laser sensor. The laser establishes the location of the bottom of the section, and then the platform reverses the direction of movement, moving from bottom to top making MSP and color reflectance measurements. All foam inserts were removed from the half cores before measurement, so that the measured range of values represents that of the core material only. During Expedition 356, MSP and color reflectance data were collected at constant intervals of 2.5 cm. This resolution facilitates comparison with results obtained from the magnetic susceptibility loop of the WRMSL, which has a sampling interval of 5 cm.

Color reflectance spectrometry

The color reflectance spectrometer uses an Ocean Optics 30 mm integrating sphere and both halogen and LED light sources, which covers wavelengths from UV through visible to near infrared. The measurements were taken from 380 to 900 nm wavelengths at 2 nm intervals. The approximate 3 s data acquisition offset was applied for the entire scan of the archive half. The data are reported using the $L^*a^*b^*$ color system, in which L^* is lightness, a^* is redness (positive) versus greenness (negative), and b^* is yellowness (positive) versus blueness (negative) of the rock. The color reflectance spectrometer calibrates on two spectra, pure white (reference) and pure black (dark). Color calibration was conducted approximately once every 6 h (twice per shift). See additional details in [Lithostratigraphy and sedimentology](#).

Point magnetic susceptibility

MSP was measured with a Bartington MS2 meter and an MS2K contact probe with a flat 15 mm diameter round sensor with a field of influence of 25 mm and an operation frequency of 930 Hz. The archive halves of split cores were covered with clear plastic wrap to ensure a flush contact between the MSP sensor and the split core without sediment contaminating the sensor. Different instrument settings were used, with the instrument averaging one, two, or three measurements from the sensor for each offset. Early during Expedition 356, we observed a drift in instrument readings during the measurements of every section half. This drift was empirically estimated by repeated measurements of a split core liner filled with Styrofoam. We found that a third-order polynomial best describes the observed drift and used this equation to correct the MSP measurements:

$$d = ax^3 + bx^2 + cx,$$

where d is the drift during the measurement of a section half and x is the offset of the measurement within the section in centimeters. The constants a , b , and c are -1.70×10^{-6} , 1.49×10^{-4} , and 1.99×10^{-2} for three averaged measurements per offset and -2.29×10^{-6} , 1.88×10^{-4} , and 2.44×10^{-2} for two averaged measurements per offset. The drift-corrected SHMSL MSP results were made available to the entire science party during Expedition 356. However, only the raw data are available through the LIMS database.

The spatial resolution of the MSP instrument is ~ 3.8 mm. As with whole-round measurements, the output displayed by the MSP sensor must be converted to dimensionless SI units by multiplying by 10^{-5} . The probe is zeroed in air before each measurement location to avoid influence from the metal track. The MSP meter was calibrated by the manufacturer before installation on the ship and is quality checked every ~ 6 h at the same time as color reflectance sensor calibration.

Section Half Measurement Gantry measurements

For soft-sediment cores, P -wave velocity and shear strength measurements were performed on the working half of split cores. P -wave velocity measurements used the x -axis caliper contact probe transducer on the Section Half Measurement Gantry (SHMG), with at least one analysis per core. Cores drilled with the XCB system generally did not provide usable data because of bad sediment/liner contact and disturbed sediment. For lithified sediments, P -wave velocity was measured on discrete samples and/or on samples taken within core liners and/or on MAD cubes, prior to MAD analyses.

P -wave velocity

The P -wave velocity system uses Panametrics-NDT Microscan delay line transducers, which transmit at 0.5 MHz. The signal received through the section half or discrete sample was recorded by the computer attached to the system. During Expedition 356, if the automatic picker failed to give sensible results, we manually picked the point of maximum change in slope at the start of the first arrival. The distance between transducers was measured with a built-in linear voltage displacement transformer. Calibration was performed with a series of acrylic cylinders of differing thicknesses and a known P -wave velocity of 2750 ± 20 m/s. The determined system time delay from calibration was subtracted from the picked arrival time to give a traveltime of the P -wave through the sample. The thickness of the sample (calculated by the linear voltage displacement transformer, in meters) was divided by the traveltime (in seconds) to calculate P -wave velocity in meters per second.

Shear strength

Shear strength is the resistance of a material to failure in shear. Shear stress in unconsolidated materials is resisted only by the network of solid particles. Shear strength (τ_f) can be expressed as a function of the effective normal stress at failure (σ'), the effective cohesion (c'), and friction angle (ϕ'):

$$\tau_f = c' + \sigma' \tan \phi',$$

where c' and ϕ' are the shear strength parameters that define a linear relationship between τ_f and ϕ' , according to the Mohr-Coulomb failure criterion.

Shear strength parameters can be determined by means of multiple laboratory tests. The c' and ϕ' are relevant in situations where

field drainage conditions correspond to test conditions. The shear strength of a soil under undrained conditions (interstitial water drainage does not occur during failure) is different from that under drained conditions (interstitial water drainage occurs).

Undrained shear strength (S_u) can be expressed in terms of total stress in the case of fully saturated materials of low permeability (e.g., clays). The most common strength tests in shipboard laboratories are the vane shear and penetrometer tests, which provide measurement of undrained shear strength (Blum, 1997).

During Expedition 356, S_u was measured in undisturbed fine-grained sediment using the handheld Torvane shear device in working-half cores. Undrained shear strength was determined by inserting an eight-bladed vane into the split core and putting it under shear stress to cause a cylindrical surface to be sheared by the vane. This procedure provides a measurement of the peak shear strength, expressed in units of kilograms per square centimeter. Measurements were made with the vane rotation axis perpendicular to the split surface. Shear strength was measured once in each core when sediments were within the instrument range.

A pocket penetrometer (Model 29-3729, Ele International) was used to measure the sediment's response to normal stress (units of kilograms per square centimeter). Measurements were made close to the stratigraphic position of the S_u measurements described above.

Discrete sample measurements of moisture and density

Discrete samples were collected from the working halves to determine wet and dry bulk density, grain density, water content, and porosity. In soft sediment, $\sim 10 \text{ cm}^3$ samples were collected with a plastic syringe, a diameter that fit within that of the glass vials. As a general rule, two samples were taken in each full-length core and one in each half-length core in the first hole at each site. Depending on lithologic variability, additional samples were taken in conjunction with smear slides or thin sections. In indurated sediment and hard rock, sawed $1.4 \text{ cm} \times 1.4 \text{ cm} \times 3 \text{ cm}$ (to $1 \text{ cm} \times 1 \text{ cm} \times 1.5 \text{ cm}$) cubes were extracted from the working halves for physical properties measurements, and many of these cubes were also used for orthogonal P -wave velocity measurements. Sampling frequency was reduced to 1–2 samples every other core or less from overlapping portions of Holes B, C, and/or D. However, certain sections of overlapping cores were targeted for repeat measurements or even increased sampling in order to refine observational trends suggested by earlier cores or discrepancies between holes seen in WRMSL data. As we selected the locations for discrete sampling of physical properties, we attempted to co-locate them with those for slide smears and thin sections.

Sample preparation

Soft-sediment samples were placed in numbered preweighed $\sim 16 \text{ mL}$ Wheaton glass vials for wet and dry sediment weighing, drying, and dry volume measurements. A more complex procedure is traditionally followed for lithified sediments. To determine the wet mass of lithified sediment, we placed the samples in individual plastic vials filled with seawater and used a vacuum chamber to force saturation in the pore spaces. The vacuum pump removed the air from the chamber to a pressure of $\sim 40\text{--}50 \text{ kPa}$ below atmospheric pressure, in theory forcing seawater into the samples. These samples were kept under saturation for at least 24 h, with the vacuum maintained in the chamber by turning the pump on for 10 min every 1 h. After removal from the saturator, the cubes were patted

dry with a paper towel and wet mass immediately determined using the dual balance system. However, we also measured these wet samples before placing them in the 24 h seawater bath under vacuum and found that the wet mass was not changed within observational uncertainty by this procedure. That is, pore water saturation was not affected by 24 h in seawater under a vacuum. Thus, subsequent lithified samples were not placed in a seawater bath under a vacuum. The only lithified samples for which we followed the above procedures were several PAL samples that had been cored 4 days prior to our processing of the samples. These samples were also weighed before and after the 24 h vacuum seawater bath and all weighed less after 24 h in the seawater bath, supporting our earlier decision to dispense with soaking of lithified material.

P -wave velocities were then measured on some of the wet lithified samples. Following the velocity measurements, the samples were placed in numbered preweighed $\sim 16 \text{ mL}$ Wheaton glass vials for wet and dry sediment weighing, drying, and dry volume measurements. Samples were dried in a convection oven for at least 24 h at $105^\circ\text{C} \pm 5^\circ\text{C}$. Dried samples were then cooled in a desiccator for at least 60 min before dry mass and volume were measured.

Dual balance mass measurement

The weights of wet and dry sample masses were determined to a precision of 0.005 g using two Mettler Toledo electronic balances, with one acting as a reference. A standard weight of similar value to the sample was placed on the reference balance to increase accuracy. A computer averaging system was used to compensate for the ship's motion. The default setting of the balances is 300 measurements (taking $\sim 1.5 \text{ min}$).

Pycnometer volume measurement

Dry sample volume was determined using a hexapycnometer system of a six-celled custom-configured Micrometrics AccuPyc 1330TC helium-displacement pycnometer. The precision of each cell is 1% of the full-scale volume. Volume measurement was preceded by three purges of the sample chamber with helium warmed to $\sim 28^\circ\text{C}$. Three measurement cycles were run for each sample. A reference volume (set of two calibration spheres) was placed sequentially in one of the chambers to check for instrument drift and systematic error. The volumes occupied by the numbered Wheaton vials were calculated before the cruise by multiplying each vial's weight against the average density of the vial glass. Dry mass and volume were measured after samples were heated in an oven at $105^\circ\text{C} \pm 5^\circ\text{C}$ for 24 h and allowed to cool in a desiccator. The procedures for the determination of these physical properties comply with the American Society for Testing and Materials (ASTM) designation (D) 2216 (ASTM International, 1990). The fundamental relation and assumptions for the calculations of all physical properties parameters are discussed by Blum (1997) and summarized below.

Mass and volume calculation

We measured wet mass (M_{wet}), dry mass (M_{dry}), and dry volume (V_{dry}). The ratio of mass (rm) is a computational constant of 0.965 (i.e., 0.965 g of freshwater per 1 g of seawater). Salt precipitated in sediment pores during the drying process is included in the M_{dry} and V_{dry} values. The mass of the evaporated water (M_{water}) and salt (M_{salt}) in the sample are given by

$$M_{\text{water}} = M_{\text{wet}} - M_{\text{dry}}, \text{ and}$$

$$M_{\text{salt}} = M_{\text{water}}[s/(1 - s)],$$

where s is the assumed saltwater salinity (0.035) corresponding to a pore water density (ρ_{pw}) of 1.024 g/cm³ and a salt density (ρ_{salt}) of 2.22 g/cm³.

The corrected mass of pore water (M_{pw}), volume of pore water (V_{pw}), mass of solids excluding salt (M_{solid}), volume of salt (V_{salt}), volume of solids excluding salt (V_{solid}), and wet volume (V_{wet}) are

$$M_{pw} = (M_{wet} - M_{dry})/rm,$$

$$V_{pw} = M_{pw}/\rho_{pw},$$

$$M_{solid} = M_{wet} - M_{pw},$$

$$M_{salt} = M_{pw} - (M_{wet} - M_{dry}),$$

$$V_{salt} = M_{salt}/\rho_{salt},$$

$$V_{wet} = V_{dry} - V_{salt} + V_{pw}, \text{ and}$$

$$V_{solid} = V_{wet} - V_{pw}.$$

Calculation of bulk properties

For all sediment samples, water content (w) is expressed as the ratio of mass of pore water to wet sediment (total) mass:

$$w = M_{pw}/M_{wet}.$$

Wet bulk density (ρ_{wet}), dry bulk density (ρ_{dry}), sediment grain density (ρ_{solid}), porosity (ϕ), and void ratio (VR) are calculated as

$$\rho_{wet} = M_{wet}/V_{wet}$$

$$\rho_{dry} = M_{solid}/V_{wet}$$

$$\rho_{solid} = M_{solid}/V_{solid}$$

$$\phi = V_{pw}/V_{wet}, \text{ and}$$

$$VR = V_{pw}/V_{solid}.$$

MAD properties reported and plotted in the physical properties sections of all site chapters were calculated with the MADMax ship-board program, set with "Method C" calculation process.

Downhole measurements

Downhole logs are used to determine physical, chemical, and structural properties of the formation penetrated by a borehole. The data are rapidly collected, continuous with depth, and measured in situ; they can be interpreted in terms of the stratigraphy, lithology, physical properties, mineralogy, magnetic characteristics, and geochemical composition of the penetrated formation. Where core recovery is incomplete or disturbed, log data may provide the only way to characterize the sedimentary succession. Where core recovery is good, log and core data complement one another and may be interpreted jointly.

Downhole logs measure formation properties on a scale that is intermediate between that of laboratory measurements on core samples and that of geophysical surveys. The logs are useful in calibrating the interpretation of geophysical survey data and provide a necessary link for the integrated understanding of physical and

chemical properties on different scales. Moreover, the physical properties of the recovered core can be changed from in situ characteristics either because of the drilling process or the change in pressure, and downhole measurements can thus help to characterize these changes.

In addition, during the initial coring of some holes, we also measured the formation temperature as a function of depth, and this allowed us to estimate the heat flux, which is important for assessing the viability of models governing the tectonic subsidence regionally.

Wireline logging

During wireline logging operations, the logs are recorded with Schlumberger logging tools combined into tool strings, which are lowered into the open borehole after completion of coring operations. Three tool strings were used during Expedition 356: the triple combination (combo), which measures borehole width, total spectral gamma ray (HSGR), porosity, density, resistivity, and MS; the Formation MicroScanner (FMS)-sonic, which provides FMS resistivity images of the borehole wall and sonic velocities; and the Versatile Seismic Imager (VSI) for the vertical seismic profile (VSP). Each tool string also contains a telemetry cartridge for communicating through the wireline to the Schlumberger data acquisition system (MAXIS unit) on the ship. In preparation for logging, the boreholes were reamed in their lower sections, flushed of debris by circulating drilling fluid, and were at least partially filled with seawater-based logging gel (sepiolite mud mixed with seawater and weighted with barite; density ~1258 kg/m³) to help stabilize the borehole walls in sections where instability was expected from drilling and coring disturbance. The BHA was pulled up to ~80 meters below seafloor (mbsf), where it protected the unstable upper part of the hole. The tool strings were then lowered downhole on a seven-conductor wireline cable before being pulled up at a constant speed of 550 m/h for the triple combo and FMS-sonic to provide continuous log measurements of several properties simultaneously.

Each tool string deployment is termed a logging "run." During each run, tool strings can be lowered and pulled up in the hole several times to check repeatability or to increase coverage of the FMS borehole images. Each lowering or hauling-up of the tool string while collecting data constitutes a "pass." Incoming data were recorded and monitored in real time on the MCM MAXIS logging computer. A wireline heave compensator (WHC) was used to minimize the effect of ship's heave on the tool position in the borehole (see below).

Logged sediment properties and tool measurement principles

The logged properties and the principles the tools use to measure them are briefly described below. More detailed information on individual tools and their geological applications may be found in Serra (1984, 1986, 1989), Schlumberger (1989), Rider (1996), Goldberg (1997), Lovell et al. (1998), and Ellis and Singer (2007). A complete online list of acronyms for the Schlumberger tools and measurement curves is at <http://iodp.tamu.edu/tools/logging/index.html>.

Natural gamma radiation

The Hostile Environment Natural Gamma Ray Sonde (HNGS) was used on both the triple combo and FMS-sonic tool strings to measure HSGR in the formation. The HNGS uses two bismuth germanate scintillation detectors and five-window spectroscopy to determine concentrations of potassium (in weight percent), thorium

(in parts per million), and uranium (in parts per million) from the characteristic gamma ray energies of isotopes in the ^{40}K , ^{232}Th , and ^{238}U radioactive decay series, which dominate the natural radiation spectrum. The computation of the elemental abundances uses a least-squares method of extracting U, Th, and K elemental concentrations from the spectral measurements. The HNGS filters out gamma ray energies below 500 keV, eliminating sensitivity to bentonite or KCl in the drilling mud and improving measurement accuracy. The HNGS also provides a measure of the HSGR and uranium-free or computed gamma ray (HCGR) that are measured in American Petroleum Institute units (gAPI). The HNGS response is influenced by the borehole diameter; therefore, the HNGS data are corrected for borehole diameter variations during acquisition.

An additional gamma ray sensor was housed in the Enhanced Digital Telemetry Cartridge (EDTC), which was used primarily to communicate data to the surface. The sensor includes a sodium iodide scintillation detector that measures the total natural gamma ray emissions of the formation. It is not a spectral tool (does not provide U, Th, and K concentrations), but it provides total gamma radiation for each pass.

The inclusion of the HNGS in every tool string allows use of the gamma ray data for precise depth-match processing between logging strings and passes and for core-log integration.

Density and photoelectric factor

Formation density was measured with the Hostile Environment Litho-Density Sonde (HLDS). The HLDS contains a radioactive cesium (^{137}Cs) gamma ray source (622 keV) and far and near gamma ray detectors mounted on a shielded skid, which is pressed against the borehole wall by a hydraulically activated decentralizing arm. Gamma rays emitted by the source undergo Compton scattering, in which gamma rays are scattered by electrons in the formation. The number of scattered gamma rays that reach the detectors is proportional to the density of electrons in the formation, which is in turn related to bulk density. Porosity may also be derived from this bulk density if the matrix (grain) density is known.

The HLDS also measures the photoelectric effect (PEF), a measure of the photoelectric absorption of low-energy gamma radiation. Photoelectric absorption of the gamma rays occurs when their energy falls below 150 keV as a result of being repeatedly scattered by electrons in the formation. PEF is determined by comparing the counts from the far detector in the high-energy region, where only Compton scattering occurs, with those in the low-energy region, where count rates depend on both reactions. Because PEF depends on the atomic number of the elements in the formation (heavier elements have higher PEF), it also varies according to the chemical composition of the minerals present and can be used for the identification of the overall mineral make-up of the formation. For example, the PEF of calcite is 5.08 barn/e⁻, illite is 3.03 barn/e⁻, quartz is 1.81 barn/e⁻, and hematite is 21 barn/e⁻.

Good contact between the tool and borehole wall is essential for good HLDS logs; poor contact results in underestimation of density values. During Expedition 356, some holes were often wide throughout the cored interval, and thus not ideally suited for this tool. For this reason and to limit the possibility of losing an environmentally hazardous package during deployment, the HLDS was not run in some holes. Both the density correction and caliper measurement of the hole are used to check the contact quality. In the deeper parts of the hole, the PEF log should be used with caution, especially in washouts, because barium in the logging mud swamps the signal despite a correction for the influence of mud.

Porosity

Formation porosity was measured with the Accelerator Porosity Sonde (APS). It was not run in some holes because the often-wide borehole and porous sediments were not ideally suited for the APS porosity measurement. The APS includes a minitron neutron generator that produces fast (14.4 MeV) neutrons and five neutron detectors (four epithermal and one thermal) positioned at different distances from the minitron. The tool's detectors count neutrons that arrive at the detectors after being scattered and slowed by collisions with atomic nuclei in the formation.

The highest energy loss occurs when neutrons collide with hydrogen nuclei, which have practically the same mass as the neutron (the neutrons bounce off of heavier elements without losing much energy). If the hydrogen (i.e., water) concentration is low, as in low-porosity formations, neutrons can travel farther before being captured and the count rates increase at the detector. The opposite effect occurs in high-porosity formations where the water content is high. However, because hydrogen bound in minerals such as clays or in hydrocarbons also contributes to the measurement, the raw porosity value is often an overestimate. The detector also allows the standoff distance between the wall and the tool to be estimated.

Upon reaching thermal energies (0.025 eV), the neutrons are captured by the nuclei of Cl, Si, B, and other elements, resulting in a gamma ray emission. This neutron capture cross section (Σ_f) is also measured by the tool.

Electrical resistivity

The High-Resolution Laterolog Array (HRLA) tool provides six resistivity measurements with different depths of investigation, including the borehole, or mud, resistivity and five measurements of formation resistivity with increasing penetration into the formation. The tool sends a focused current into the formation and measures the intensity necessary to maintain a constant drop in voltage across a fixed interval, providing direct resistivity measurements. The array has one central (source) electrode and six electrodes above and below it, which serve alternatively as focusing and returning current electrodes. By rapidly changing the roles of these electrodes, a simultaneous resistivity measurement at six penetration depths is achieved. The tool is designed to ensure that all signals are measured at exactly the same time and tool position to reduce the sensitivity to "shoulder bed" effects when crossing sharp beds thinner than the electrode spacing. The design of the HRLA, which eliminates the need for a surface reference electrode, improves formation resistivity evaluation compared to traditional dual induction and allows the full range of resistivity to be measured, from low (e.g., in high-porosity sediments) to high (e.g., in basalt). The HRLA needs to be run centralized in the borehole for optimal results, so knuckle joints were used to centralize the HRLA while allowing the density and porosity tools to maintain good contact with the borehole wall.

Calcite, silica, and hydrocarbons are electrical insulators, whereas ionic solutions like interstitial water are conductors. Electrical resistivity, therefore, can be used to evaluate porosity for a given salinity and resistivity of the interstitial water. Clay surface conduction also contributes to the resistivity values, but at high porosities, this is a relatively minor effect.

Acoustic velocity

The Dipole Sonic Imager (DSI) measures the transit times between sonic transmitters and an array of eight receivers. It combines replicate measurements, thus providing a direct measurement of sound velocity through formations that is relatively free from the ef-

fects of formation damage and an enlarged borehole (Schlumberger, 1989). Along with the monopole transmitters found on most sonic tools, it also has two crossed-dipole transmitters that allow the measurement of shear wave velocity in addition to compressional wave velocity. Dipole measurements are necessary to measure shear velocities in slow formations with shear velocity less than the velocity of sound in the borehole fluid. Such slow formations are typically encountered in deep-ocean drilling.

Magnetic susceptibility sonde

The magnetic susceptibility sonde (MSS) is a nonstandard wire-line tool designed by Lamont-Doherty Earth Observatory (LDEO). It measures the ease with which formations are magnetized when subjected to a magnetic field. The ease of magnetization is ultimately related to the concentration and composition (size, shape, and mineralogy) of magnetic minerals (principally magnetite) in the formation. These measurements provide one of the best methods for investigating stratigraphic changes in mineralogy and lithology because the measurement is quick, repeatable, and nondestructive and because different lithologies often have strongly contrasting susceptibilities.

The MSS dual-coil sensor provides ~36 cm vertical resolution measurements, with ~20 cm depth of horizontal investigation. The MSS was run as the lowermost tool in the triple combo tool string, using a specially developed data translation cartridge to enable the MSS to be run in combination with the Schlumberger tools. The MSS also has an optional single-coil sensor to provide high-resolution measurements (~10 cm), but this was not used during Expedition 356 because it has a large bowspring that would require the MSS to be run higher up in the tool string and because it is very sensitive to separation from the borehole wall.

MS data are plotted as uncalibrated units. The MSS reading responses are affected by temperature and borehole size (higher temperatures lead to higher susceptibility measurements). The MS values were not fully corrected for temperature on shore during Expedition 356 such that values deeper than several hundred meters were generally not interpretable. When the MS signal in sediment is very low, the detection limits of the tool may be reached. For quality control and environmental correction, the MSS also measures internal tool temperature, *z*-axis acceleration, and low-resolution borehole conductivity.

Formation MicroScanner

The FMS provides high-resolution electrical resistivity-based images of borehole walls. The tool has four orthogonal arms and pads, each containing 16 button electrodes that are pressed against the borehole wall during logging. The electrodes are arranged in two diagonally offset rows of 8 electrodes each. A focused current is emitted from the button electrodes into the formation, with a return electrode near the top of the tool. Resistivity of the formation at the button electrodes is derived from the intensity of current passing through each electrode on the button.

Processing transforms the resistivity measurements into oriented high-resolution images that reveal geologic structures of the borehole wall. Features such as bedding, stratification, fracturing, slump folding, and bioturbation can be resolved (Lovell et al., 1998; Serra, 1989). Because the images are oriented to magnetic north, further analysis can provide measurement of the dip and direction (azimuth) of planar features in the formation. In addition, when the corresponding planar features can be identified in the recovered

core samples, individual core pieces can be reoriented with respect to true north.

Approximately 30% of a borehole with a diameter of 25 cm is imaged during a single pass. Standard procedure is to make two full uphole passes with the FMS to maximize the borehole coverage with the pads. The maximum extension of the caliper arms is 40.6 cm. In holes with a diameter greater than this maximum, the pad contact at the end of the caliper arms will be inconsistent, and the FMS images may appear out of focus and too conductive. Irregular (rough) borehole walls will also adversely affect the images if contact with the wall is poor.

Acceleration and inclinometry

Three-component acceleration and magnetic field measurements were made with the General Purpose Inclinometry Tool (GPIT). The primary purpose of this tool, which incorporates a three-component accelerometer and a three-component magnetometer, is to determine the acceleration and orientation of the FMS-sonic and Ultrasonic Borehole Imager (not run during Expedition 356) tool strings during logging. This information allows the FMS and UBI images to be corrected for irregular tool motion and the dip and direction (azimuth) of features in the images to be determined. The GPIT was also run on the triple combo tool string in order to provide data to optimize the WHC before logging began and hence to acquire the best possible downhole data. Tools on both the triple combo and FMS-sonic tool strings can carry remanent or induced magnetization; therefore, GPIT magnetic measurements can be affected. However, on the FMS-sonic tool string, the GPIT has greater nonmagnetic insulation from the other tools, which greatly reduces extraneous effects on its magnetic measurements.

Vertical seismic profile

In a VSP experiment, a borehole seismic tool (VSI) is anchored against the borehole wall at regularly spaced intervals and records the full waveform of elastic waves generated by a seismic source positioned just below the sea surface. These “check shot” measurements relate depth in the hole to traveltime in reflection seismic profiles. The VSI used on the ship contains a three-axis geophone. In a VSP survey, the VSI was anchored against the borehole wall at approximately 25 m station intervals (where possible), with 5–10 air gun shots typically taken at each station. The recorded waveforms were stacked and a one-way traveltime was determined from the median of the first breaks for each station. The seismic source used was a Sercel G-gun parallel cluster composed of two 250 in³ air guns separated by 1 m. It was positioned on the port side of the *JOIDES Resolution* at a water depth of ~7 m below sea level with a borehole offset of ~45 m.

Precautions were taken to protect marine mammals, turtles, and diving sea birds. If there were no mammals in or approaching the safety radius of 1850 m stipulated for shallow-water depths between 98 and 205 m during Expedition 356, air gun operations commenced using a ramp-up, or “soft start” procedure (gradually increasing the operational pressure and air gun firing interval) to provide time for undetected animals to respond to the sounds and vacate the area. Diving sea birds are subject to different exclusion zones, which for Expedition 356, was restricted to the immediate vicinity of the vessel. Once the air guns were at full power, the check shot survey proceeded. Marine mammal, turtle, and sea bird observations continued during the check shot survey, and if a protected species entered the designated safety radius, the survey was suspended.

Log data quality

The main influence on log data quality is the condition of the borehole wall. Where the borehole diameter varies over short intervals because of washouts of softer material or ledges of harder material, the logs from tools that require good contact with the borehole wall (i.e., FMS, density, and porosity) may be degraded. Deep investigation measurements such as gamma radiation, resistivity, MS, and sonic velocity, which do not require contact with the borehole wall, are generally less sensitive to borehole conditions. “Bridged” sections, where borehole diameter is significantly below the bit size, will also cause irregular log results. The quality of the borehole is improved by minimizing the circulation of drilling fluid while drilling, flushing the borehole to remove debris, and logging as soon as possible after drilling and conditioning are completed.

The quality of the wireline depth determination depends on several factors. The depth of the logging measurements is determined from the length of the cable payed out from the winch on the ship. The seafloor is identified on the HSGR log by the abrupt upward reduction in gamma ray count at the water/sediment interface (mudline). Discrepancies between the drilling depth and the wireline log depth may occur. For the case of drilling depth, discrepancies are due to core expansion, incomplete core recovery, or incomplete heave compensation. In the case of log depth, discrepancies between successive runs occur because of incomplete heave compensation, incomplete correction for cable stretch, and cable slip. Tidal changes in sea level affect both drilling and logging depths, with tidal amplitude up to 4 m at the northernmost sites of Expedition 356.

Wireline heave compensator

During wireline logging operations, the up-and-down motion of the ship (heave) causes a similar motion of the downhole logging tools. If the amplitude of this motion is large, depth discrepancies can be introduced into the logging data. The risk of damaging downhole instruments is also increased. A WHC system was thus designed to compensate for the vertical motion of the ship and maintain a steady motion of the logging tools to ensure high-quality logging data acquisition (Liu et al., 2013; Iturrino et al., 2013). The WHC uses a vertical accelerometer (motion reference unit [MRU]) positioned under the rig floor near the ship’s center of gravity to calculate the vertical motion of the ship with respect to the seafloor. It then adjusts the length of the wireline by varying the distance between two sets of pulleys through which the cable passes in order to minimize downhole tool motion. Real-time measurements of up-hole (surface) and downhole acceleration are made simultaneously by the MRU and the EDTC, respectively. An LDEO-developed software package allows these data to be analyzed and compared in real time, displaying the actual motion of the logging tool string and enabling monitoring of the efficiency of the compensator.

Logging data flow and log depth scales

Data for each wireline logging run were monitored in real time and recorded using the Schlumberger MAXIS 500 system. Initial logging data were referenced to the rig floor (wireline log depth below rig floor [WRF]). After logging was completed, the data were shifted to a seafloor reference (WSF), which was based on the step in gamma radiation at the sediment/water interface.

Data were transferred onshore to LDEO where standardized data processing took place. The main part of the processing is depth matching to remove depth offsets between logs from different log-

ging runs, which results in a new depth scale: WMSF. Also, corrections are made to certain tools and logs (e.g., FMS imagery is corrected for tool acceleration, including “stick and slip”), documentation for the logs (with an assessment of log quality) is prepared, and the data are converted to ASCII for the conventional logs and GIF for the FMS images. The data were transferred back to the ship within a few days of logging, and this processed data set was made available to the science party (in ASCII and digital log information standard [DLIS] formats) through the shipboard IODP logging database and shipboard servers. The Schlumberger Petrel software was used to visualize and unbundle the DLIS.

In situ temperature measurements

During Expedition 356, in situ temperature measurements were made with the advanced piston corer temperature tool (APCT-3) at several sites; we often chose the second APC hole for the measurements after the ease of APC coring was assessed in the first APC hole. The APCT-3 fits directly into the coring shoe of the APC and consists of a battery pack, data logger, and platinum resistance-temperature device calibrated over a temperature range from 0° to 30°C. Before entering the borehole, the tool is first stopped at the mudline for 5 min to thermally equilibrate with bottom water. When the APC is plunged into the formation, it causes an instantaneous temperature rise from frictional heating. This heat gradually dissipates into the surrounding sediment as the temperature at the APCT-3 equilibrates toward the temperature of the sediment. After the APC penetrated the sediment, it was held in place for about 10 min while the APCT-3 recorded the temperature of the cutting shoe every 1 s.

The equilibrium temperature of the sediment was estimated by applying a heat-conduction model to the temperature decay record (Horai and Von Herzen, 1985). The synthetic thermal decay curve for the APCT-3 is a function of the geometry and thermal properties of the probe and the sediment (Bullard, 1954; Horai and Von Herzen, 1985). Equilibrium temperature was estimated by applying a fitting procedure (Pribnow et al., 2000). However, if the APC does not achieve a full stroke or if ship heave pulls the APC up from full penetration, the temperature equilibration curve is disturbed and temperature determination is less accurate. The nominal accuracy of the APCT-3 temperature measurements is $\pm 0.05^\circ\text{C}$.

APCT-3 temperature data were combined with thermal conductivity measurements (see [Physical properties](#)) obtained from whole-round core sections to obtain heat flow values. Heat flow was calculated according to the Bullard method, to be consistent with the synthesis of ODP heat flow data by Pribnow et al. (2000).

Stratigraphic correlation

Some Expedition 356 scientific objectives required recovery of complete stratigraphic sections to the fullest extent possible. Continuous sedimentary sections cannot be recovered from a single borehole because gaps in recovery occur between successive cores, even when 100% or more nominal recovery is attained (Ruddiman et al., 1987; Hagelberg et al., 1995). Construction of a complete stratigraphic section, referred to as a splice, requires combining intervals from two or more holes cored at the same site. To maximize the probability that missing sedimentary sections from within a given hole are recovered in one or more adjacent holes, we attempt to offset between holes the depths below the seafloor from which cores are recovered. At least two complete holes, and in many cases three or more holes, are needed to recover a complete section in the interval cored by the APC.

Our methods for developing composite depths and splices followed the basic strategy that is now common practice on all high-resolution paleoceanographic expeditions. We used initial measurements of MS and gamma ray density run on the STMSL to develop preliminary composite depths for purposes of making real-time drilling decisions (Mix, Tiedemann, Blum, et al., 2003). STMSL data were collected immediately after recovery, at a time when the cores had not yet reached equilibrium temperature. Therefore, differences are expected between STMSL and WRMSL values. The depth scale was refined as different data sets (e.g., NGR) and more detailed information became available during drilling.

Our goals for stratigraphic correlation, in priority order, were to

- Guide drilling to ensure recovery of a complete stratigraphic section,
- Establish a composite depth scale,
- Define a stratigraphically complete and representative sampling splice,

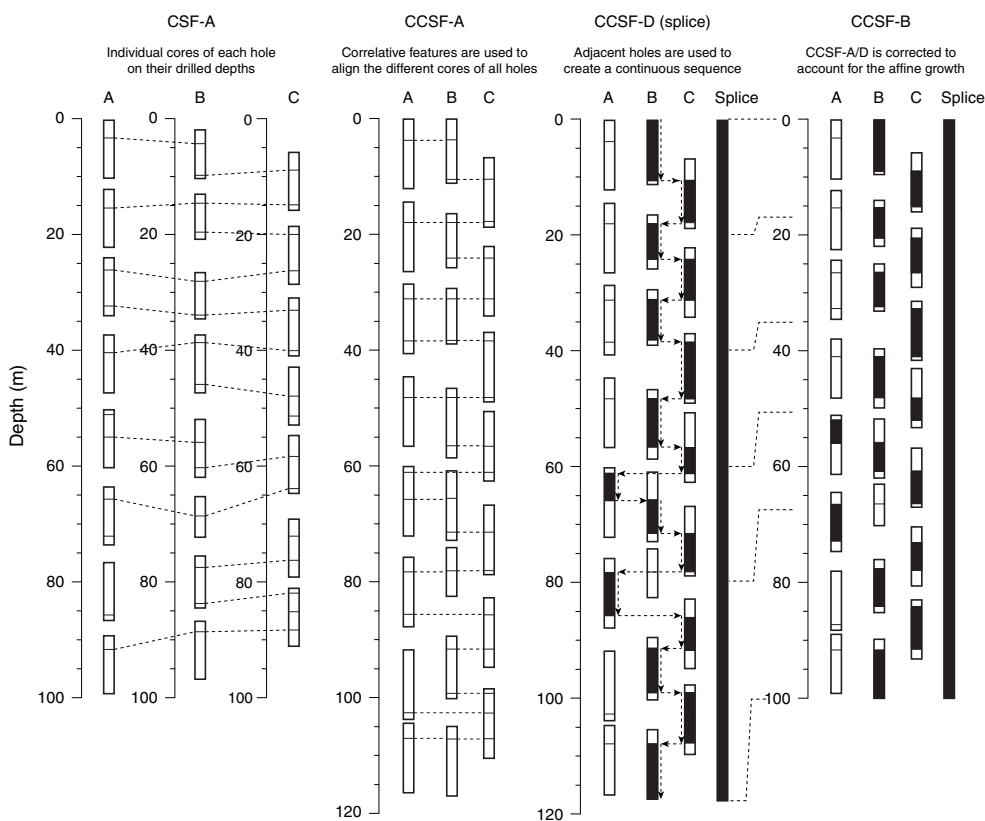
- Evaluate and refine shipboard stratigraphic age models and their uncertainties by synthesizing all available age information in a common depth framework, and
- Develop preliminary reconstructions of sedimentation rates.

Drilling was guided using the MS and GRA data from the STMSL system to monitor stratigraphic position and assess mud-line targets during operations. During drilling, notes were kept on core handling (e.g., if core had to be pushed within the liner) and core quality (e.g., possible flow-in or crushed liner). Correlations were developed using MS data and refined with NGR data, which were collected after thermal equilibrium. Because Expedition 356 sediments are hemipelagic, variation was anticipated and observed between holes. Catwalk notes and VCDs were helpful in determining if the variation was real or the result of drilling disturbances. The correlation was used to generate the splice. As a result of this stratigraphic correlation process, several different depth models are created. Table T4 and Figure F11 summarize these various IODP

Table T4. Definitions of different depth scales used during Expedition 356. [Download table in .csv format.](#)

IODP depth scale	Complete name	Definition
CSF-A	Core depth below seafloor (mbsf)	Initial drilling depth.
CCSF-A	Core composite depth below seafloor, appended	Composite depth scale in which cores from all holes are aligned by adding an affine specific to each core.
CCSF-D	Splice	Composite sequence representing the complete stratigraphy at a site. It is composed of core sections from adjacent holes such that coring gaps or sampling gaps in one hole are filled with sediment from an adjacent hole.

Figure F11. Schematic illustration of depth scales used during Expedition 356. The black section in individual cores reflects the interval used to construct a continuous splice (black continuous sequence). Note the expansion in depth (affine growth) in the CCSF-A and -D depth scales. The CCSF-B scale corrects for this apparent expansion.



depth models. Detailed discussion of the definitions of these depth scales, and the processes by which they are created, appear below.

Composite depth scale

The initial CSF-A depth scale is based on the length that the drill string is advanced core by core. This is equivalent to the ODP scale mbsf. The CSF-A scale is inaccurate because of ship heave (which is not compensated for during APC coring), tidal variations in sea level (see below), and other sources of error. Before a splice can be constructed, the cores from the various holes must be stratigraphically correlated with each other. Such correlation transfers CSF-A depths into a composite depth scale referred to as CCSF-A. The splice that results is known as core composite depth below seafloor, Method D (CCSF-D). Differences between these depth scales occur because depths to features measured using the individual CSF-A scales for adjacent holes may be slightly offset from their depths in the splice on the CCSF-D scale. These IODP depth scales are approximately equivalent to the ODP depth scale meters composite depth (mcd) and are further described below.

The CCSF-A scale is built by assuming that the uppermost sediment (commonly referred to as the “mudline”) in the first core of a hole is the sediment/water interface. At each site, this selected core becomes the “anchor” in the composite depth scale and is usually the only one in which depths are the same on both the CSF-A and CCSF-A scales. From this anchor, core logging data are correlated among holes by working downsection. For each core in adjacent holes, a (constant) depth offset, or affine value, chosen to best align observed lithologic variations to the equivalent cores in adjacent holes, is added to the CSF-A depth in sequence downhole. The differential offset is the increase in these affine values between cores. For example, when Core A2 has an affine value of 2 m and Core A4 has an affine value of 3 m, the differential offset between Cores A2 and A3 is 1 m.

During Expedition 356, an initial composite depth scale was created using whole-round GRA and MS measured with a loop sensor from the STMSL. The STMSL measurements were initially taken at coarse (10 cm) resolution immediately after recovery (before thermal equilibration) to provide initial data for the correlators. Correlations based primarily on whole-round GRA and MS data were augmented by NGR data from the core logger and digital color parameters ($L^*a^*b^*$) measured on the SHMSL and MS data obtained with the WRMSL following 4 h of acclimatization and thermal equilibration (see [Physical properties](#)). The final CCSF-A scale and the splice for each site were based on color reflectance b^* and NGR data; however, the STMSL data are retained in the database as a useful check on the final data and because some damaged sections fit through the STMSL but could not be run on the WRMSL. In some cases, small depth offsets were found for features within core sections measured by the STMSL and WRMSL; a common cause of this offset is gas expansion in the cores between the STMSL and WRMSL measurements. In these cases, attempts were made to define composite depths using the last data measured prior to core splitting, but this was not always possible. Some depth mismatches (typically on the scale of centimeters, but potentially tens of centimeters) may exist between composite depths defined by whole-round sensing and the depths at which particular features appear in split cores.

Specific methods for STMSL, WRMSL, and SHMSL measurements are described in [Physical properties](#), and SHIL measurements are described in [Lithostratigraphy and sedimentology](#).

Most core logging data were collected at 2.5, 5, 10, or 20 cm intervals, depending on time availability and core flow.

Composite depth scale construction

The core logging data were imported into the specialized shipboard software program Correlator. Correlator enables construction of a composite depth scale for each hole at a given site by depth-shifting individual cores to maximize the correlation of reproducible features in the core logging data. For hole-to-hole correlations and for plotting results, data were masked to avoid incorporating anomalous data influenced by edge effects at section boundaries, at core tops, or in voids where no sediment was present; however, all original data were retained in the LIMS database.

Because of inherent problems associated with the program Correlator, most notably the difficulty of adjusting mistakes and evaluating alternatives, Microsoft Excel was also used for correlation. Offsets were determined by graphic comparison between records, and the resulting offset table was modified to create an affine table suitable for upload to LIMS. Specifically, correlations were evaluated in a graphical display of the offsets in a graph in which each core was plotted separately. Additional guidance for the correlation was provided by using the recovery plots and CSF-A depth scale of each hole to constrain the number of possible correlations. The use of an alternative correlation method (Microsoft Excel) proved to be a useful in intervals with (1) little variability in the physical properties measured and (2) very repetitive variation in the physical properties. The quality of the correlations was noted based on the amount of overlap between the connected cores, similarity of the correlated profiles, variability between cores, and quality of the cores.

Depth intervals within cores are not squeezed or stretched; thus, it is not possible to align all the correlative features within each core. Differences between features in different holes may reflect small-scale differences in sedimentation and/or distortion caused by the coring and archiving processes. For example, the tops of APC cores may be stretched and the bottoms compressed, although this depends on lithology and the extent of lithification. In addition, sediment of unknown age occasionally falls from higher levels in the borehole onto the tops of cores as they are recovered, and as a result the tops of some cores are not reliable. Data from such intervals are masked as noted above. Tides, especially at the lower latitude sites, where tidal ranges can reach nearly 3 m, generate further complications in fidelity between CCSF-A depth and actual depth position. Fortunately, the sites most impacted by tides (Sites U1463 and U1464) were cored during neap tide, so tidal corrections were only applied for the mudline shots and not to subsequent downhole piston cores.

The depth offsets for each core that are necessary to convert CSF-A depths to the CCSF-A scale are recorded in an affine table for each site. The CCSF-A depth for any point within a core equals the CSF-A depth plus the affine offset. Correlation at finer resolution is not possible because depth adjustments are applied linearly to individual cores. At this stage, no adjustments are made in the length of each core, such as numerically squeezing and stretching within cores. Finer scale adjustments of individual cores relative to the splice (e.g., Hagelberg et al., 1995; Pälke et al., 2005) or relative to logging data (e.g., Harris et al., 1995) can be done following the development of the composite section.

Ideally, the base of the continuous CCSF-A scale is the bottom of the deepest core recovered from the deepest hole. In practice, however, the base often occurs where core recovery gaps align

across all holes and below which constructing a splice is impossible. Deeper cores cannot be tied directly into the overlying continuous CCSF-A scale. These cores are appended, and CCSF-A depths are calculated by adding a constant offset, which is usually the largest affine value from each hole. An exception to this case occurs when some cores from two or more holes deeper than the base of the splice can be correlated with each other, allowing the generation of a “floating” CCSF-A scale and splice for some intervals deeper than the continuous CCSF-A scale.

The length of the CCSF-A depth scale at a given site is typically ~10%–20% greater than the length of the cored interval in any one hole as indicated by the CSF-A depth scale. Although the exact reasons for this apparent expansion of the sediment column are not completely known, it is commonly attributed to rebound following release of overburden in the deeper sections, stretching during the coring process, gas expansion during the core recovery process, and other factors (Moran, 1997).

Splice

The splice is a composite stratigraphic section representing the complete record at a site. It is composed of core sections from adjacent holes such that coring gaps or sampling gaps, like those generated by taking IW samples, in one hole are filled with core from an adjacent hole. The splice does not generally contain coring gaps, and an effort has been made to minimize inclusion of disturbed sections by examining core photographs. The splice guides core sampling for high-resolution studies. Tables and figures in each site chapter summarize the intervals from each hole used to construct the splice. The portion of the CCSF-A depth scale that is applied to the splice is referred to as the CCSF-D depth scale. Within the splice sections, CCSF-D is identical to CCSF-A.

Note, however, that because of stretching and squeezing within cores, some features may not correlate precisely between the splice and samples taken off the splice, even though all samples have CCSF-A depths. Therefore, the final composite depth scale, CCSF-D, is only formally defined within the primary splice.

The choice of splice tie points is a somewhat subjective exercise. We constructed the splice by visually determining tie points in the aligned core profiles in Microsoft Excel. Our method in the construction of a splice followed four rules. First, where possible, we avoided using the first and last sections of cores, where disturbance due to drilling artifacts (even if not apparent in core logging data) was most likely. Second, we attempted to incorporate those realizations of the stratigraphic section that in our judgment were most representative of the holes recovered. Third, we tried to minimize tie points (i.e., to use the longest possible sections within individual cores) in order to simplify sampling. Fourth, we tried to minimize use of intervals sampled during the expedition to leave room for high-resolution postexpedition sampling in the splice.

Tidal effects on coring depth

Tidal influence on APC shot depth was previously documented by correlation of affine offset changes and tide height during ODP Leg 202 (Mix, Tiedemann, Blum, et al., 2003). Data on tidal heights at the drill sites were provided by the Australian Bureau of Meteorology at a 30 min resolution. Expedition 356 tidal amplitudes vary strongly from the southern sites to the northern sites. Predicted tidal amplitudes were <1.2 m at Sites U1459 and U1460, ~2 m at Sites U1461 and U1462, and ~4 m at Sites U1463 and U1464 over a tidal cycle. At Sites U1458–U1460, no tidal corrections were applied. For Sites U1461–U1464, the difference in tidal height was de-

termined relative to the tidal height at the time the mudline core in Hole A was taken. The Operations Superintendent took the difference into account when placing the mudline cores at the second and third hole, but tidal height was not taken into account for the subsequent cores in the hole.

Age models and sedimentation rates

Hole summaries were developed using the core data (e.g., MS, NGR, and color reflectance b^*) as a framework for organizing biostratigraphic and magnetostratigraphic data. Stratigraphic datums (see **Biostratigraphy and micropaleontology** and **Paleomagnetism**) were plotted on the hole summaries, and sedimentation rates were calculated assuming linear sedimentation between points. Biostratigraphic sampling was not conducted at the same intervals in every hole at each site, and in some cases sampling was only conducted in the section of the hole that differed from the first hole. Site summaries were developed using the synthesis table of biostratigraphic datums (see **Biostratigraphy and micropaleontology**) from multiple holes; therefore, although site summary sedimentation rates follow the same trend, they are usually a bit different from those of the individual holes.

References

- Agnini, C., Fornaciari, E., Raffi, I., Catanzariti, R., Pälke, H., Backman, J., and Rio, D., 2014. Biozonation and biochronology of Paleogene calcareous nannofossils from low and middle latitudes. *Newsletters on Stratigraphy*, 47(2):131–181. <http://dx.doi.org/10.1127/0078-0421/2014/0042>
- Albani, A.D., and Geijskes, R., 1973. Appendix 1: recent foraminifera from the northwest shelf. In Jones, H.A. (Ed.), *Marine Geology of the Northwest Australian Continental Shelf* (Bulletin 136): Canberra, ACT (Bureau of Mineral Resources, Geology and Geophysics), 59–82.
- ASTM International, 1990. Standard method for laboratory determination of water (moisture) content of soil and rock (Standard D2216–90). In *Annual Book of ASTM Standards for Soil and Rock* (Volume 04.08): Philadelphia (American Society for Testing Materials). [revision of D2216-63, D2216-80]
- Backman, J., Raffi, I., Rio, D., Fornaciari, E., and Pälke, H., 2012. Biozonation and biochronology of Miocene through Pleistocene calcareous nannofossils from low and middle latitudes. *Newsletters on Stratigraphy*, 45(3):221–244. <http://dx.doi.org/10.1127/0078-0421/2012/0022>
- Balsam, W.L., and Damuth, J.E., 2000. Further investigations of shipboard vs. shore-based spectral data: implications for interpreting Leg 164 sediment composition. In Paull, C.K., Matsumoto, R., Wallace, P., and Dillon, W.P. (Eds.), *Proceedings of the Ocean Drilling Program, Scientific Results*, 164: College Station, TX (Ocean Drilling Program), 313–324. <http://dx.doi.org/10.2973/odp.proc.sr.164.222.2000>
- Balsam, W.L., Damuth, J.E., and Schneider, R.R., 1997. Comparison of shipboard vs. shore-based spectral data from Amazon Fan cores: implications for interpreting sediment composition. In Flood, R.D., Piper, D.J.W., Klaus, A., and Peterson, L.C. (Eds.), *Proceedings of the Ocean Drilling Program, Scientific Results*, 155: College Station, TX (Ocean Drilling Program), 193–215. <http://dx.doi.org/10.2973/odp.proc.sr.155.210.1997>
- Balsam, W.L., Deaton, B.C., and Damuth, J.E., 1998. The effects of water content on diffuse reflectance spectrophotometry studies of deep-sea sediment cores. *Marine Geology*, 149(1–4):177–189. [http://dx.doi.org/10.1016/S0025-3227\(98\)00033-4](http://dx.doi.org/10.1016/S0025-3227(98)00033-4)
- Bejteman, K.J., 1969. Recent foraminifera from the western continental shelf of Western Australia. *Contributions from the Cushman Foundation for Foraminiferal Research*, 20(4):119–138.
- Biswas, B., 1976. Bathymetry of Holocene foraminifera and Quaternary sea-level changes on the Sunda Shelf. *Journal of Foraminiferal Research*, 6(2):107–133. <http://dx.doi.org/10.2113/gsjfr.6.2.107>
- Berggren, W.A., Kent, D.V., Swisher, C.C., III, and Aubry, M.-P., 1995. A revised Cenozoic geochronology and chronostratigraphy. In Berggren,

- W.A., Kent, D.V., Aubry, M.-P., and Hardenbol, J. (Eds.), *Geochronology, Time Scales and Global Stratigraphic Correlation*. Special Publication - SEPM (Society for Sedimentary Geology), 54:129–212. <http://dx.doi.org/10.2110/pec.95.04.0129>
- Blow, W.H., 1969. Late middle Eocene to recent planktonic foraminiferal biostratigraphy. *Proceedings of the International Conference on Planktonic Microfossils*, 1:199–422.
- Blow, W.H., 1979. *The Cainozoic Globigerinida: A Study of the Morphology, Taxonomy, Evolutionary Relationships and the Stratigraphical Distribution of Some Globigerinida (mainly Globigerinacea)*: Leiden, The Netherlands (E.J. Brill).
- Blum, P., 1997. *Technical Note 26: Physical Properties Handbook—A guide to the Shipboard Measurement of Physical Properties of Deep-Sea Cores*. Ocean Drilling Program. <http://dx.doi.org/10.2973/odp.tn.26.1997>
- Bolli, H.M., and Saunders, J.B., 1985. Oligocene to Holocene low latitude planktic foraminifera. In Bolli, H.M., Saunders, J.B., and Perch-Nielsen, K. (Eds.), *Plankton Stratigraphy (Volume 1): Planktic Foraminifera, Calcareous Nannofossils and Calpionellids*: Cambridge, United Kingdom (Cambridge University Press), 155–262.
- Bullard, E.C., 1954. The flow of heat through the floor of the Atlantic Ocean. *Proceedings of the Royal Society of London, Series A: Mathematical, Physical and Engineering Sciences*, 222(1150):408–429. <http://dx.doi.org/10.1098/rspa.1954.0085>
- Droser, M.L., and Bottjer, D.J., 1986. A semi-quantitative field classification of ichnofabric. *Journal of Sedimentary Research*, 56(4):558–559. <http://dx.doi.org/10.1306/212F89C2-2B24-11D7-8648000102C1865D>
- Dunham, R.J., 1962. Classification of carbonate rocks according to depositional texture. In Ham, W.E. (Ed.), *Classification of Carbonate Rocks*. AAPG Memoir, 1:108–121. <http://archives.datapages.com/data/spec-pubs/carbona2/data/a038/a038/0001/0100/0108.htm>
- Dunlea, A.G., Murray, R.W., Harris, R.N., Vasiliev, M.A., Evans, H., Spivack, A.J., and D'Hondt, S., 2013. Assessment and use of NGR instrumentation on the *JOIDES Resolution* to quantify U, Th, and K concentrations in marine sediment. *Scientific Drilling*, 15:57–63. <http://dx.doi.org/10.2204/iodp.sd.15.05.2013>
- Ellis, D.V., and Singer, J.M., 2007. *Well Logging for Earth Scientists* (2nd edition): New York (Elsevier).
- Embry, A.F., III, and Klovan, J.E., 1971. A late Devonian reef tract on north-eastern Banks Island, Northwest Territories. *Bulletin of Canadian Petroleum Geology*, 19(4):730–781. <http://archives.datapages.com/data/cspg/data/019/019004/0730.htm>
- Expedition 330 Scientists, 2012. Methods. In Koppers, A.A.P., Yamazaki, T., Geldmacher, J., and the Expedition 330 Scientists, *Proceedings of the Integrated Ocean Drilling Program*, 330: Tokyo (Integrated Ocean Drilling Program Management International, Inc.). <http://dx.doi.org/10.2204/iodp.proc.330.102.2012>
- Gallagher, S.J., Fulthorpe, C.S., Bogus, K., Auer, G., Baranwal, S., Castañeda, I.S., Christensen, B.A., De Vleeschouwer, D., Franco, D.R., Groeneveld, J., Gurnis, M., Haller, C., He, Y., Henderiks, J., Himmler, T., Ishiwa, T., Iwatani, H., Jatiningrum, R.S., Kominz, M.A., Korpanty, C.A., Lee, E.Y., Levin, E., Mamo, B.L., McGregor, H.V., McHugh, C.M., Petrick, B.F., Potts, D.C., Rastegar Lari, A., Renema, W., Reuning, L., Takayanagi, H., and Zhang, W., 2017. Site U1459. In Gallagher, S.J., Fulthorpe, C.S., Bogus, K., and the Expedition 356 Scientists, *Indonesian Throughflow*. Proceedings of the International Ocean Discovery Program, 356: College Station, TX (International Ocean Discovery Program). <http://dx.doi.org/10.14379/iodp.proc.356.104.2017>
- Gallagher, S.J., Jonasson, K., and Holdgate, G., 1999. Foraminiferal biofacies and palaeoenvironmental evolution of an Oligo–Miocene cool-water carbonate succession in the Otway Basin, southeast Australia. *Journal of Micropaleontology*, 18(2):143–168. <http://dx.doi.org/10.1144/jm.18.2.143>
- Gallagher, S.J., Wallace, M.W., Li, C.L., Kinna, B., Bye, J.T., Akimoto, K., and Torii, M., 2009. Neogene history of the West Pacific Warm Pool, Kuroshio and Leeuwin Currents. *Paleoceanography*, 24(1):PA1206. <http://dx.doi.org/10.1029/2008PA001660>
- Gallagher, S.J., Villa, G., Drysdale, R.N., Wade, B.S., Scher, H., Li, Q., Wallace, M.W., and Holdgate, G.R., 2013. A near-field sea level record of East Antarctic Ice Sheet instability from 32 to 27 Myr. *Paleoceanography*, 28(1):1–13. <http://dx.doi.org/10.1029/2012PA002326>
- Gealy, E.L., Winterer, E.L., and Moberly, R., Jr., 1971. Methods, conventions, and general observations. In Winterer, E.L., Riedel, W.R., et al., *Initial Reports of the Deep Sea Drilling Project*, 7: Washington, DC (U.S. Government Printing Office), 9–26. <http://dx.doi.org/10.2973/dsdp.proc.7.102.1971>
- Gieskes, J.M., Gamo, T., and Brumsack, H., 1991. *Technical Note 15: Chemical Methods for Interstitial Water Analysis Aboard JOIDES Resolution*. Ocean Drilling Program. <http://dx.doi.org/10.2973/odp.tn.15.1991>
- Gilmore, G.R., 2008. *Practical Gamma-ray Spectrometry* (2nd edition): Hoboken, NJ (John Wiley & Sons). <http://dx.doi.org/10.1002/9780470861981>
- Goldberg, D., 1997. The role of downhole measurements in marine geology and geophysics. *Reviews of Geophysics*, 35(3):315–342. <http://dx.doi.org/10.1029/97RG00221>
- Gradstein, F.M., Ogg, J.G., Schmitz, M.D., and Ogg, G.M. (Eds.), 2012. *The Geological Time Scale 2012*: Amsterdam (Elsevier).
- Hagelberg, T.K., Pisias, N.G., Shackleton, N.J., Mix, A.C., and Harris, S., 1995. Refinement of a high-resolution, continuous sedimentary section for studying equatorial Pacific paleoceanography, Leg 138. In Pisias, N.G., Mayer, L.A., Janecek, T.R., Palmer-Julson, A., and van Andel, T.H. (Eds.), *Proceedings of the Ocean Drilling Program, Scientific Results*, 138: College Station, TX (Ocean Drilling Program), 31–46. <http://dx.doi.org/10.2973/odp.proc.sr.138.103.1995>
- Haig, D.W., 1997. Foraminifera from Exmouth Gulf, Western Australia. *Journal of the Royal Society of Western Australia*, 80(4):263–280. [http://www.rswa.org.au/publications/Journal/80\(4\)/80\(4\)haig.pdf](http://www.rswa.org.au/publications/Journal/80(4)/80(4)haig.pdf)
- Harris, R.N., Sakaguchi, A., Petronotis, K., Baxter, A.T., Berg, R., Burkett, A., Charpentier, D., Choi, J., Diz Ferreiro, P., Hamahashi, M., Hashimoto, Y., Heydolph, K., Jovane, L., Kastner, M., Kurz, W., Kutterolf, S.O., Li, Y., Malinverno, A., Martin, K.M., Millan, C., Nascimento, D.B., Saito, S., Sandoval Gutierrez, M.I., Scream, E.J., Smith-Duque, C.E., Solomon, E.A., Straub, S.M., Tanikawa, W., Torres, M.E., Uchimura, H., Vannucchi, P., Yamamoto, Y., Yan, Q., and Zhao, X., 2013. Methods. In Harris, R.N., Sakaguchi, A., Petronotis, K., and the Expedition 344 Scientists, *Proceedings of the Integrated Ocean Drilling Program*, 344: College Station, TX (Integrated Ocean Drilling Program). <http://dx.doi.org/10.2204/iodp.proc.344.102.2013>
- Harris, S., Hagelberg, T., Mix, A., Pisias, N.G., and Shackleton, N.J., 1995. Sediment depths determined by comparisons of GRAPE and logging density data during Leg 138. In Pisias, N.G., Mayer, L.A., Janecek, T.R., Palmer-Julson, A., and van Andel, T.H. (Eds.), *Proceedings of the Ocean Drilling Program, Scientific Results*, 138: College Station, TX (Ocean Drilling Program), 47–57. <http://dx.doi.org/10.2973/odp.proc.sr.138.104.1995>
- Hayward, B.W., Cedhagen, T., Kaminski, M., and Gross, O. (Eds.), 2015. Data from: *World Foraminifera Database*. <http://www.marinespecies.org/foraminifera>
- Hermelin, J.O.R., 1989. Pliocene benthic foraminifera from the Ontong-Java Plateau (western equatorial Pacific Ocean): faunal response to changing paleoenvironment. *Special Publication - Cushman Foundation for Foraminiferal Research*, 26:1–143.
- Hohenegger, J., 1995. Depth estimation by proportions of living larger foraminifera. *Marine Micropaleontology*, 26(1–4):31–47. [http://dx.doi.org/10.1016/0377-8398\(95\)00044-5](http://dx.doi.org/10.1016/0377-8398(95)00044-5)
- Hohenegger, J., 2005. Estimation of environmental paleogradient values based on presence/absence data: a case study using benthic foraminifera for paleodepth estimation. *Palaeogeography, Palaeoclimatology, Palaeoecology*, 217(1–2):115–130. <http://dx.doi.org/10.1016/j.palaeo.2004.11.020>
- Horai, K., and Von Herzen, R.P., 1985. Measurement of heat flow on Leg 86 of the Deep Sea Drilling Project. In Heath, G.R., Burckle, L.H., et al., *Initial Reports of the Deep Sea Drilling Project*, 86: Washington, DC (U.S. Government Printing Office), 759–777. <http://dx.doi.org/10.2973/dsdp.proc.86.135.1985>

- Hottinger, L., Halicz, E., and Reiss, Z., 1993. *Recent Foraminiferida, Gulf of Aqaba, Red Sea*: Ljubjana, Slovenia (Slovenska Akademija Znanosti in Umetnosti).
- Iturrino, G., Liu, T., Goldberg, D., Anderson, L., Evans, H., Fehr, A., Guerin, G., Inwood, J., Lofi, J., Malinverno, A., Morgan, S., Mrozewski, S., Slagle, A., and Williams, T., 2013. Performance of the wireline heave compensation system onboard D/V *JOIDES Resolution*. *Scientific Drilling*, 15:46–50. <http://dx.doi.org/10.2204/iodp.sd.15.08.2013>
- James, N.P., Collins, L.B., Bone, Y., and Hallock, P., 1999. Subtropical carbonates in a temperate realm; modern sediments on the southwest Australian shelf. *Journal of Sedimentary Research*, 69(6):1297–1321. <http://dx.doi.org/10.2110/jsr.69.1297>
- Kennett, J.P., and Srinivasan, M.S., 1983. *Neogene Planktonic Foraminifera: A Phylogenetic Atlas*: Stroudsburg, PA (Hutchinson Ross).
- Kirschvink, J.L., 1980. The least-squares line and plane and the analysis of palaeomagnetic data. *Geophysical Journal of the Royal Astronomical Society*, 62(3):699–718. <http://dx.doi.org/10.1111/j.1365-246X.1980.tb02601.x>
- Kristiansen, J.I., 1982. The transient cylindrical probe method for determination of thermal parameters of earth materials [Ph.D. dissertation]. Århus University, Århus, Denmark.
- Kruiver, P.P., Dekkers, M.J., and Heslop, D., 2001. Quantification of magnetic coercivity components by the analysis of acquisition curves of isothermal remanent magnetization. *Earth and Planetary Science Letters*, 189(3–4):269–276. [http://dx.doi.org/10.1016/S0012-821X\(01\)00367-3](http://dx.doi.org/10.1016/S0012-821X(01)00367-3)
- Langer, M.R., and Hottinger, L., 2000. Biogeography of selected “larger” foraminifera. *Micropaleontology*, 46(Supplement 1):105–126. <http://www.jstor.org/stable/1486184>
- Li, Q., James, N.P., Bone, Y., and McGowran, B., 1999. Palaeoceanographic significance of Recent foraminiferal biofacies on the southern shelf of Western Australia: a preliminary study. *Palaeogeography, Palaeoclimatology, Palaeoecology*, 147(1–2):101–120. [http://dx.doi.org/10.1016/S0031-0182\(98\)00150-3](http://dx.doi.org/10.1016/S0031-0182(98)00150-3)
- Li, Q., McGowran, B., James, N.P., and Bone, Y., 1996a. Foraminiferal biofacies on the mid-latitude Lincoln shelf, South Australia: oceanographic and sedimentological implications. *Marine Geology*, 129(3–4):285–312. [http://dx.doi.org/10.1016/0025-3227\(96\)83349-4](http://dx.doi.org/10.1016/0025-3227(96)83349-4)
- Li, Q., McGowran, B., James, N.P., Bone, Y., and Cann, J.H., 1996b. Mixed foraminiferal biofacies on the mesotrophic, mid-latitude Lacedpede shelf, South Australia. *Palaios*, 11(2):176–191. <http://dx.doi.org/10.2307/3515069>
- Liu, T., Iturrino, G., Goldberg, D., Meissner, E., Swain, K., Furman, C., Fitzgerald, P., Frisbee, N., Chlimoun, J., Van Hyfte, J., and Beyer, R., 2013. Performance evaluation of active wireline heave compensation systems in marine well logging environments. *Geo-Marine Letters*, 33(1):83–93. <http://dx.doi.org/10.1007/s00367-012-0309-8>
- Loeblich, A.R., Jr., and Tappan, H., 1988. *Foraminiferal Genera and Their Classification*: New York (Van Nostrand Reinhold).
- Loeblich, A.R., Jr., and Tappan, H., 1994. Foraminifera of the Sahul shelf and Timor Sea. *Special Publication Cushman Foundation for Foraminiferal Research*, 31.
- Lovell, M.A., Harvey, P.K., Brewer, T.S., Williams, C., Jackson, P.D., and Williamson, G., 1998. Application of FMS images in the Ocean Drilling Program: an overview. In Cramp, A., MacLeod, C.J., Lee, S.V., and Jones, E.J.W. (Eds.), *Geological Evolution of Ocean Basins: Results from the Ocean Drilling Program*. Geological Society Special Publication, 131(1):287–303. <http://dx.doi.org/10.1144/GSL.SP.1998.131.01.18>
- Lumsden, D.N., 1979. Discrepancy between thin section and X-ray estimates of dolomite in limestone. *Journal of Sedimentary Petrology*, 49(2):429–436. <http://dx.doi.org/10.1306/212F7761-2B24-11D7-8648000102C1865D>
- Lurcock, P.C., and Wilson, G.S., 2012. PuffinPlot: a versatile, user-friendly program for paleomagnetic analysis. *Geochemistry, Geophysics, Geosystems*, 13(6):Q06Z45. <http://dx.doi.org/10.1029/2012GC004098>
- Manheim, F.T., and Sayles, F.L., 1974. Composition and origin of interstitial waters of marine sediments, based on deep sea drill cores. In Goldberg, E.D. (Ed.), *The Sea* (Volume 5): *Marine Chemistry: The Sedimentary Cycle*: New York (Wiley), 527–568.
- Martini, E., 1971. Standard Tertiary and Quaternary calcareous nannoplankton zonation. In Farinacci, A. (Ed.), *Proceedings of the Second Planktonic Conference, Roma 1970*: Rome (Edizioni Tecnoscienza), 2:739–785.
- McKee, E.D., and Weir, G.W., 1953. Terminology for stratification and cross-stratification in sedimentary rocks. *Geological Society of America Bulletin*, 64(4):381–390. [http://dx.doi.org/10.1130/0016-7606\(1953\)64\[381:TFSACI\]2.0.CO;2](http://dx.doi.org/10.1130/0016-7606(1953)64[381:TFSACI]2.0.CO;2)
- Mix, A.C., Tiedemann, R., Blum, P., et al., 2003. *Proceedings of the Ocean Drilling Program, Initial Reports*, 202: College Station, TX (Ocean Drilling Program). <http://dx.doi.org/10.2973/odp.proc.ir.202.2003>
- Moran, K., 1997. Elastic property corrections applied to Leg 154 sediment, Ceara Rise. In Shackleton, N.J., Curry, W.B., Richter, C., and Bralower, T.J. (Eds.), *Proceedings of the Ocean Drilling Program, Scientific Results*, 154: College Station, TX (Ocean Drilling Program). <http://dx.doi.org/10.2973/odp.proc.sr.154.132.1997>
- Murray, R.W., Miller, D.J., and Kryc, K.A., 2000. *Technical Note 29: Analysis of Major and Trace Elements in Rocks, Sediments, and Interstitial Waters by Inductively Coupled Plasma–Atomic Emission Spectrometry (ICP–AES)*. Ocean Drilling Program. <http://dx.doi.org/10.2973/odp.tn.29.2000>
- Norris, R.D., Wilson, P.A., Blum, P., Fehr, A., Agnini, C., Bornemann, A., Boulila, S., Bown, P.R., Cournede, C., Friedrich, O., Ghosh, A.K., Hollis, C.J., Hull, P.M., Jo, K., Junium, C.K., Kaneko, M., Liebrand, D., Lippert, P.C., Liu, Z., Matsui, H., Moriya, K., Nishi, H., Opdyke, B.N., Penman, D., Romans, B., Scher, H.D., Sexton, P., Takagi, H., Turner, S.K., Whiteside, J.H., Yamaguchi, T., and Yamamoto, Y., 2014. Site U1405. In Norris, R.D., Wilson, P.A., Blum, P., and the Expedition 342 Scientists, *Proceedings of the Integrated Ocean Drilling Program*, 342: College Station, TX (Integrated Ocean Drilling Program). <http://dx.doi.org/10.2204/iodp.proc.342.106.2014>
- Okada, H., and Bukry, D., 1980. Supplementary modification and introduction of code numbers to the low-latitude coccolith biostratigraphic zonation (Bukry, 1973; 1975). *Marine Micropaleontology*, 5:321–325. [http://dx.doi.org/10.1016/0377-8398\(80\)90016-X](http://dx.doi.org/10.1016/0377-8398(80)90016-X)
- Orpin, A.R., Haig, D.W., and Woolfe, K.J., 1999. Sedimentary and foraminiferal facies in Exmouth Gulf, in arid tropical northwestern Australia. *Australian Journal of Earth Sciences*, 46(4):607–621. <http://dx.doi.org/10.1046/j.1440-0952.1999.00728.x>
- Pälike, H., Moore, T., Backman, J., Raffi, I., Lanci, L., Parés, J.M., and Janecek, T., 2005. Integrated stratigraphic correlation and improved composite depth scales for ODP Sites 1218 and 1219. In Wilson, P.A., Lyle, M., and Firth, J.V. (Eds.), *Proceedings of the Ocean Drilling Program, Scientific Results*, 199: College Station, TX (Ocean Drilling Program), 1–41. <http://dx.doi.org/10.2973/odp.proc.sr.199.213.2005>
- Parker, J.H., 2009. Taxonomy of foraminifera from Ningaloo Reef, Western Australia. *Memoirs of the Association of Australasian Palaeontologists*, 36.
- Parker, R.L., and Gee, J.S., 2002. Calibration of the pass-through magnetometer—II. Application. *Geophysical Journal International*, 150:140–152. <http://dx.doi.org/10.1046/j.1365-246X.2002.01692.x>
- Pearson, P.N., Olsson, R.K., Hemleben, C., Huber, B.T., and Berggren, W.A., 2006. Atlas of Eocene planktonic foraminifera. *Special Publication - Cushman Foundation for Foraminiferal Research*, 41.
- Perch-Nielsen, K., 1985. Cenozoic calcareous nannofossils. In Bolli, H.M., Saunders, J.B., and Perch-Nielsen, K. (Eds.), *Plankton Stratigraphy*: Cambridge, United Kingdom (Cambridge University Press), 427–554.
- Pribnow, D., Kinoshita, M., and Stein, C., 2000. *Thermal Data Collection and Heat Flow Recalculations for Ocean Drilling Program Legs 101–180*: Hanover, Germany (Institute for Joint Geoscientific Research, Institut für Geowissenschaftliche Gemeinschaftsaufgaben [GGA]). <http://www-odp.tamu.edu/publications/heatflow/ODPReprt.pdf>
- Quilty, P.G., 1977. Foraminifera of Hardy Inlet, southwestern Australia. *Journal of the Royal Society of Western Australia*, 59(3):79–90.
- Renema, W., 2006. Large benthic foraminifera from the deep photic zone of a mixed siliciclastic-carbonate shelf off East Kalimantan, Indonesia. *Marine Micropaleontology*, 58(2):73–82. <http://dx.doi.org/10.1016/j.micromicro.2005.10.004>

- Rider, M.H., 1996. *The Geological Interpretation of Well Logs* (2nd edition): Caithness, Scotland (Whittles Publishing).
- Rothwell, R.G., 1989. *Minerals and Mineraloids in Marine Sediments: An Optical Identification Guide*: London (Elsevier).
- Ruddiman, W.F., Cameron, D., and Clement, B.M., 1987. Sediment disturbance and correlation of offset holes drilled with the hydraulic piston corer: Leg 94. In Ruddiman, W.F., Kidd, R.B., Thomas, E., et al., *Initial Reports of the Deep Sea Drilling Project*, 94: Washington, DC (U.S. Government Printing Office), 615–634.
<http://dx.doi.org/10.2973/dsdp.proc.94.111.1987>
- Saito, T., Thompson, P.R., and Breger, D., 1981. *Systematic Index of Recent and Pleistocene Planktonic Foraminifera*: Tokyo (University of Tokyo).
- Schlumberger, 1989. *Log Interpretation Principles/Applications*: Houston (Schlumberger Education Services), SMP-7017.
- Sen Gupta, B.K., 1999. Systematics of modern foraminifera. In Sen Gupta, B.K. (Ed.), *Modern Foraminifera*: London (Kluwer Academic), 7–36.
- Serra, O., 1984. *Fundamentals of Well-Log Interpretation* (Volume 1): *The Acquisition of Logging Data*: Amsterdam (Elsevier).
- Serra, O., 1986. *Fundamentals of Well-Log Interpretation* (Volume 2): *The Interpretation of Logging Data*: Amsterdam (Elsevier).
- Serra, O., 1989. *Formation MicroScanner Image Interpretation*: Houston (Schlumberger Education Services), SMP-7028.
- Shepard, F.P., 1954. Nomenclature based on sand-silt-clay ratios. *Journal of Sedimentary Research*, 24(3):151–158.
<http://dx.doi.org/10.1306/D4269774-2B26-11D7-8648000102C1865D>
- Shipboard Scientific Party, 2002. Leg 194 summary. In Isern, A.R., Anselmetti, E.S., Blum, P., et al., *Proceedings of the Ocean Drilling Program, Initial Reports*, 194: College Station, TX (Ocean Drilling Program), 1–88.
<http://dx.doi.org/10.2973/odp.proc.ir.194.101.2002>
- Sissingh, W., 1977. Biostratigraphy of Cretaceous calcareous nannoplankton. *Geologie en Mijnbouw*, 56:37–65.
- Smith, A.J., and Gallagher, S.J., 2003. The Recent foraminifera and facies of the Bass Canyon: a temperate submarine canyon in Gippsland, Australia. *Journal of Micropalaeontology*, 22(1):63–83.
<http://dx.doi.org/10.1144/jm.22.1.63>
- Smith, A.J., Gallagher, S.J., Wallace, M., Holdgate, G., Daniels, J., and Keene, J., 2001. The Recent temperate foraminiferal biofacies of the Gippsland shelf: an analogue for Neogene environmental analyses in southeastern Australia. *Journal of Micropalaeontology*, 20(2):127–142.
<http://dx.doi.org/10.1144/jm.20.2.127>
- Stow, D.A.V., 2005. *Sedimentary Rocks in the Field: A Colour Guide*: London (Manson Publishing)
- Szarek, R., Kuhnt, W., Kawamura, H., and Kitazato, H., 2006. Distribution of recent benthic foraminifera on the Sunda shelf (South China Sea). *Marine Micropaleontology*, 61(4):171–195.
<http://dx.doi.org/10.1016/j.marmicro.2006.06.005>
- Tauxe, L., Tucker, P., Peterson, N.P., and LaBrecque, J.L., 1984. Magnetostratigraphy of Leg 73 sediments. In Hsü, K.J., LaBrecque, J.L., et al., *Initial Reports of the Deep Sea Drilling Project*, 73: Washington, DC (U.S. Government Printing Office), 609–621.
<http://dx.doi.org/10.2973/dsdp.proc.73.123.1984>
- Thompson, P.R., Bé, A.W.H., Duplessy, J.-C., and Shackleton, N.J., 1979. Disappearance of pink-pigmented *Globigerinoides ruber* at 120,000 yr BP in the Indian and Pacific oceans. *Nature*, 280(5723):554–558.
<http://dx.doi.org/10.1038/280554a0>
- Tucker, M.E., and Wright, P.V., 1990. *Carbonate Sedimentology*: Oxford, United Kingdom (Blackwell Science Publishing).
- Vacquier, V., 1985. The measurement of thermal conductivity of solids with a transient linear heat source on the plane surface of a poorly conducting body. *Earth and Planetary Science Letters*, 74(2–3):275–279.
[http://dx.doi.org/10.1016/0012-821X\(85\)90027-5](http://dx.doi.org/10.1016/0012-821X(85)90027-5)
- van der Zwaan, G.J., Jorissen, F.J., and de Stigter, H.C., 1990. The depth dependency of planktonic/benthic foraminiferal ratios: constraints and applications. *Marine Geology*, 95(1):1–16.
[http://dx.doi.org/10.1016/0025-3227\(90\)90016-D](http://dx.doi.org/10.1016/0025-3227(90)90016-D)
- van Hinsbergen, D.J.J., Kouwenhoven, T.J., and van der Zwaan, G.J., 2005. Paleobathymetry in the backstripping procedure: correction for oxygenation effects on depth estimates. *Palaeogeography, Palaeoclimatology, Palaeoecology*, 221(3–4):245–265.
<http://dx.doi.org/10.1016/j.palaeo.2005.02.013>
- van Marle, L.J., 1988. Bathymetric distribution of benthic foraminifera on the Australian-Irian Jaya continental margin, eastern Indonesia. *Marine Micropaleontology*, 13(2):97–152.
[http://dx.doi.org/10.1016/0377-8398\(88\)90001-1](http://dx.doi.org/10.1016/0377-8398(88)90001-1)
- Van Marle, L.J., 1991. Eastern Indonesian late Cenozoic smaller benthic foraminifera. *Verhandelingen - Koninklijke Nederlandse Akademie van Wetenschappen, Afdeling Natuurkunde, Eerste Reeks*, 34.
- Vasiliev, M.A., Blum, P., Chubarian, G., Olsen, R., Bennight, C., Cobine, T., Fackler, D., Hastedt, M., Houpt, D., Mateo, Z., and Vasilieva, Y.B., 2011. A new natural gamma radiation measurement system for marine sediment and rock analysis. *Journal of Applied Geophysics*, 75:455–463.
<http://dx.doi.org/10.1016/j.jappgeo.2011.08.008>
- Von Herzen, R., and Maxwell, A.E., 1959. The measurement of thermal conductivity of deep-sea sediments by a needle-probe method. *Journal of Geophysical Research*, 64(10):1557–1563.
<http://dx.doi.org/10.1029/JZ064i010p01557>
- Wade, B.S., Pearson, P.N., Berggren, W.A., and Pälike, H., 2011. Review and revision of Cenozoic tropical planktonic foraminiferal biostratigraphy and calibration to the geomagnetic polarity and astronomical time scale. *Earth-Science Reviews*, 104(1–3):111–142.
<http://dx.doi.org/10.1016/j.earscirev.2010.09.003>
- Wentworth, C.K., 1922. A scale of grade and class terms for clastic sediments. *Journal of Geology*, 30(5):377–392. <http://dx.doi.org/10.1086/622910>
- Young, J.R., 1998. Neogene. In Bown, P.R. (Ed.), *Calcareous Nannofossil Biostratigraphy*: Dordrecht, The Netherlands (Kluwer Academic Publishing), 225–265.
- Zijderveld, J.D.A., 1967. AC demagnetization of rocks: analysis of results. In Collinson, D.W., Creer, K.M., and Runcorn, S.K. (Eds.), *Methods in Palaeomagnetism*: Amsterdam (Elsevier), 254–286.



Minerva Access is the Institutional Repository of The University of Melbourne

Author/s:

Gallagher, SJ; Fulthorpe, CS; Bogus, K; Auer, G; Baranwal, S; Castañeda, IS; Christensen, BA; De Vleeschouwer, D; Franco, DR; Groeneveld, J; Gurnis, M; Haller, C; He, Y; Henderiks, J; Himmler, T; Ishiwa, T; Iwatani, H; Jatiningrum, RS; Kominz, MA; Korpanty, CA; Lee, EY; Levin, E; Mamo, BL; McGregor, HV; McHugh, CM; Petrick, BF; Potts, DC; Rastegar Lari, A; Renema, W; Reuning, L; Takayanagi, H; Zhang, W

Title:

Expedition 356 methods

Date:

2017

Citation:

Gallagher, S. J., Fulthorpe, C. S., Bogus, K., Auer, G., Baranwal, S., Castañeda, I. S., Christensen, B. A., De Vleeschouwer, D., Franco, D. R., Groeneveld, J., Gurnis, M., Haller, C., He, Y., Henderiks, J., Himmler, T., Ishiwa, T., Iwatani, H., Jatiningrum, R. S., Kominz, M. A. ,... Zhang, W. (2017). Expedition 356 methods. International Ocean Discovery Program.

Persistent Link:

<http://hdl.handle.net/11343/197507>

File Description:

Published version